



---

**Forschungszentrum Karlsruhe**  
in der Helmholtz-Gemeinschaft

---

**Wissenschaftliche Berichte**  
FZKA 7161

# **Simulation of the Optimised Design of the HFTM and the Natural Convection Simulation in the IFMIF Test Cell Cavity**

**B. Dolensky, S. Gordeev, V. Heinzl,  
K. Lang, A. Möslang, V. Slobodchuk,  
E. Stratmanns**

**Institut für Reaktorsicherheit  
Institut für Materialforschung  
Programm Kernfusion**

**Oktober 2005**



**Forschungszentrum Karlsruhe**

in der Helmholtz-Gemeinschaft

Wissenschaftliche Berichte

FZKA 7161

Simulation of the optimised design of the HFTM  
and the natural convection simulation in the IFMIF  
test cell cavity

B. Dolensky, S. Gordeev, V. Heinzl, K. Lang, A. Möslang,  
V. Slobodchuk, E. Stratmanns

Institut für Reaktorsicherheit  
Institut für Materialforschung  
Programm Kernfusion

**Final Report in framework of contract Nr 325/20280021/IRS**

**Impressum der Print-Ausgabe:**

**Als Manuskript gedruckt  
Für diesen Bericht behalten wir uns alle Rechte vor**

**Forschungszentrum Karlsruhe GmbH  
Postfach 3640, 76021 Karlsruhe**

**Mitglied der Hermann von Helmholtz-Gemeinschaft  
Deutscher Forschungszentren (HGF)**

**ISSN 0947-8620**

**urn:nbn:de:0005-071611**

## **Abstract**

The thermohydraulic simulation of the optimised design of the High Flux Test Module (HFTM) for the International Fusion Material Irradiation Facility (IFMIF) is done with the commercial code STAR-CD. The work is mainly focused on the detailed analysis of the temperature and velocity distribution in the module. Particularly, the influence of the cooling channels deformation as well as the heat of the target back wall on the thermohydraulic characteristics of the HFTM is estimated. It has been also shown that the target temperature in the volume with samples can be reached with the acceptable temperature gradient for the temperature level of 4500C and 6500C by use of the electrical heaters. The appropriate power of the electrical heaters are obtained for all the rigs.

Additional task of the investigation is the optimisation of the lateral reflector cooling system. The cooling system consisting of four cooling channels is suggested to decrease the temperature level of the lateral reflector and to decrease the temperature non-uniformity in it. Nevertheless, the preliminary stress analysis showed high stress value in the rig wall. So, further work is required in this direction to achieve the acceptable stress in the structure.

The first results of the natural convection simulation in the IFMIF test cell cavity are also presented in this report. These results are obtained for a simplified simulation of the test cell cavity and the work should be continued to obtain more reliable data.

## **Zusammenfassung**

### **Thermohydraulische Simulationen des optimierten Entwurfs des Hochfluß - Testmoduls HFTM und Simulationen der Naturkonvektion in der IFMIF Testzelle.**

Thermohydraulische Simulationen des optimierten Entwurfs des Hochfluß - Testmoduls (HFTM) für die Internationale Fusionsmaterial-Bestrahlungseinrichtung (IFMIF) wurden mit Hilfe des kommerziellen CFD Computerprogramms Star-CD durchgeführt. Die Arbeit konzentrierte sich im Wesentlichen auf die Analysen der Temperatur- und Geschwindigkeitsverteilung in HFTM / Bestrahlungseinsätzen (Rigs). In erster Linie wurde die Wirkung der Deformation des Kühlkanals und der beheizten Lithium-Target-Rückplatte auf die thermohydraulischen Parameter des HFTM untersucht. Es wurde auch nachgewiesen, dass die vorgesehenen Bestrahlungstemperaturen von 450°C bis 650°C mit akzeptablen Temperaturdifferenzen in den Proben nur mit der elektrischen Beheizung erreicht werden können. Die benötigten Heizleistungen wurden für alle Rigs im HFTM ermittelt.

Die nächste Untersuchungsaufgabe war die Optimierung des Kühlsystems des seitlichen Reflektors. Um die ungleichmäßige Temperaturverteilung im Reflektor zu verringern, wurde ein Kühlsystem aus vier Kühlkanälen vorgeschlagen. Die ersten Spannungsanalysen zeigen, dass die Spannungen in der Rig-Wand immer noch zu hoch sind. Um akzeptable Spannungen in der Struktur zu erreichen, sind weitere Untersuchungen erforderlich.

Im dritten Teil des Berichts werden die ersten Ergebnisse der Simulationen zur Naturkonvektion in der IFMIF Testzelle vorgestellt. Das Ziel der Untersuchung war die Einschätzung des Beitrages der Naturkonvektion zur Wärmeübertragung in der mit Gas gefüllten Testzelle. Da die Rechnungen zunächst mit einigen Vereinfachungen durchgeführt wurden, sind weitere detailliertere Simulationen notwendig.

**Contents**

- 1 Introduction ..... 1**
  
- 2 Simulation of the optimised design of the HFTM..... 1**
  - 2.1 Description of the design ..... 1*
  - 2.2 Modelling of the design..... 3*
  - 2.3 The first results of the simulation..... 4*
  - 2.4 Optimisation of the stiffening wall temperature ..... 5*
    - 2.4.1 Comparison of turbulence models for thermohydraulic simulation ..... 5*
    - 2.4.2 Stiffening plate temperature. .... 6*
  - 2.5 Influence of the electrical heaters ..... 9*
  - 2.6 Choice of an appropriate power of the electrical heaters..... 10*
  - 2.7 Simulation of the IFMIF/HFTM with deformed cooling channels ..... 10*
    - 2.7.1 Simulation of the cooling channels deformation for all channels of the model 11*
    - 2.7.2 Comments on the results. .... 12*
    - 2.7.3 Simulation of individual rig dimension deviations from the reference design.. 13*
  - 2.8 Influence of the heat from the target back wall on the HFTM..... 15*
  - 2.9 Optimization of the IFMIF lateral reflector cooling system. .... 16*
  
- 3 Natural convection simulation in the IFMIF test cell cavity ..... 19**
  - 3.1 Testing turbulence models for natural convection simulation..... 19*
    - 3.1.1 Introductory remarks..... 19*
    - 3.1.2 Model description and simulation..... 20*
    - 3.1.3 Results of the simulation ..... 20*
  - 3.2 Simulation of the natural convection flow in the IFMIF test cell cavity ..... 23*
  
- 4 Acknowledgement..... 24**
  
- 5 References..... 25**



# 1 Introduction

This report is the final report summing up the results obtained in the framework of the contract Nr 325/20280021/IRS. The work carried out in the framework of this contract is concerned with the numerical simulation of the thermohydraulic characteristics of the IFMIF/HFTM and natural convection in the IFMIF test cell cavity. The report consists of several sections including the description of the HFTM simulation, the thermohydraulic analysis of the optimised design of this module, the influence of the deformation and geometrical tolerance of the cooling channels on the thermohydraulic characteristics, the optimisation of the lateral reflector cooling system, the choice of an appropriate power of the electrical heaters for all the rigs, and the first results of the natural convection simulation in the IFMIF test cell cavity. The results obtained are presented and discussed below.

## 2 Simulation of the optimised design of the HFTM

### 2.1 Description of the design

The optimised design of the HFTM test section with chocolate plate rigs is shown in Fig. 2.1, 2.2, [1]. Based on preliminary hydraulic calculations a single rectangular duct with a cross section of 88x52 mm has been chosen for the helium flow to the test section. It is positioned asymmetrically by one side of the irradiation zone. The uniform feeding of helium to the rigs is improved by two baffles inserted in the 180° bend joining the ducts with downward and upward flow. The lateral reflectors are integral parts of the container housing the test rigs. Helium cooling of these reflectors is provided by a bypass to the main flow. The lower axial reflector is a single bloc with appropriate channels to lead the helium flow to the rigs. The upper axial reflector is split into 12 single parts according to the number of rigs. The outer shape is selected such that cooling channels of the necessary dimensions are generated. Holes in the blocs allow the insertion of thermocouples and heater wires.

Fig. 2.2 shows a horizontal cross section of the test section (x,z-plane) in the region of the irradiation zone. It consists of a container with an inner cross section of 203 x52 mm. In the y,z-plane the container is divided into four compartments by stiffening plates serving to stabilise the container walls. Each compartment is filled with 3 rigs. The rigs have an outer cross section of 49x16 mm. Cooling channels are provided at all sides of the rigs with a width of 1.0 mm at the large sides and of 0.5 mm at the small sides. The dimensions of the cooling channels are assured by small vertical ribs at the corners and the side walls of the rigs. The attachment of the rigs inside the container is not yet included in the design.

Details of the rig design are shown in Fig. 2.2, 2.3. They consist of the outer housing (rig wall) and the inner capsule containing the specimens separated by a thermal insulation with a thickness of 1.35 mm at the large side and 1 mm at the small side. The capsule has an inner cross section of 40x9.3 mm. This allows a rather dense arrangement of most of the envisaged test specimens (see Fig. 2.2). Electrical heaters are wrapped around the capsule in horizontal windings. This concept will lead to temperatures of the capsule close to the irradiation temperature of the specimens, whereas the rig wall is at about the level of the helium temperature.

The length of the rig without the upper reflector is 144 mm. The capsules have a length of 125 mm and are closed by two cup-shaped caps giving the testing zone a length of 81.5 mm. This includes 0.5 mm for the accommodation of thermal expansion differences. The capsules are filled with a liquid metal (Na or, if possible NaK) to increase the thermal contact between the specimens and the capsule walls. The upper cap has two holes connecting the test zone with the NaK expansion volume of about 20 mm length located at the top end of the rig. To facilitate filling of the capsule with NaK to a defined level, two tubes are provided at the top side of the expansion tank. One of these tubes dips into the tank to the envisaged filling level, the other one ends at the top plate. The filling level is established by at first filling the tank completely, and then blowing out the surplus NaK via the dip tube by applying a gas pressure to the other one. Finally, both tubes have to be cut and sealed. The volume of the expansion tank and the filling level have been determined taking into account the NaK volume, the filling temperature and the operating temperature.

The main design problem of the rigs is to realise the specified level and constancy of the irradiation temperatures. The maximum thickness of the capsule (in z-direction) is given by the power density and the thermal conductivity of the specimens/NaK mixture in connection with the allowable maximum temperature difference across the specimens. This consideration leads to a maximum thickness of about 10 mm for the first row of rigs. At the rear side of the HFTM the capsule thickness can be larger according to the decrease in power density, but in order to minimise the design and manufacturing effort it was decided to use identical dimensions for all the rigs. Taking into account the dimensions and possible arrangements of the specimens (see Fig. 2.2), 9.3 mm has been chosen as internal capsule widths.

Of course, the specified constancy of the specimen temperature must likewise be achieved in the two other directions, i.e. x and y. The latter is of particular importance because of the large variation in the power density, the coolant temperature rise and heat transfer coefficient variation along the flow channel. Different solutions have been studied, e.g. variable thermal insulation or compensation by electrical heating. The latter way was finally adopted mainly for the following two reasons:

- a) This solution allows one the use of a uniform thermal insulation with the advantage of easier manufacturing.
- b) Electrical heating is necessary in any case to maintain the temperature during beam-off periods.

In detailed analyses [1] it was found that three sections with different but constant heating power are necessary and sufficient to reach the desired temperature constancy. In order to allow the compensation of uncertainties in the temperature prediction, individual power supply and control of each section is required.

Mineral insulated wires of 1 mm diameter are envisaged as heating elements. To assure sufficient thermal contact, they have to be attached to the capsules by brazing them into grooves. The sectioning of the heating necessitates horizontal winding (in the x,z-plane) of the heaters. A high density of the heaters is necessary to reach the required temperature without exceeding the specified power limits of the heaters. On the other hand, the ribs between the heaters must be sufficiently large to facilitate manufacturing. Based on manufacturing trials, a distance of 1.6 mm between the heater windings has been adopted.

The thermal insulation between the rig wall and the capsules must be designed such that the irradiation temperature specified for each rig is reached in a reliable and reproducible way. It was estimated that a helium layer between about 0.1 and 1 mm thickness would fulfil the thermal requirement. For the upper temperature range the following concept is suggested: a plane helium gap between the rig wall and the capsule with a pressure which is higher than in the cooling channel. This can easily be realised by joining the gap and the helium coolant at the rig inlet. At these pressure conditions the rig wall is deflected toward the cooling channel. First estimates have shown that this deflection amounts to about 0.1 mm which is in the range of 10 % of the thickness of the insulation layer. This could affect the specimen temperature. The effect can be significantly reduced by increasing the wall thickness of the outer container, or by providing a vertical rib in the middle of the cooling channel (already included in the design).

As explained before, electrical heating is provided with three heating zones. The heaters are embedded in grooves and joined to the surface of the capsule by brazing. The grooves have a width of 1.1 mm and a distance of 1.6 mm. The six cold ends of the heaters are led to the top end of the rigs along the small sides of the capsules via vertical grooves located below the peripheral grooves. The thermocouples needed for the measurement of the specimen temperatures and the control of the electrical power supply system (two thermocouples for each heating section) are inserted into the centre of the specimen stack at the required location. They leave the capsule through sleeves, and follow then the way of the heaters to the top end of the rig.

## **2.2 Modelling of the design**

The simulation of the module is performed in accordance with the design requirements. The model under consideration consists of the test section and the gas supply system. The irradiated section of the module is simulated as four parallel compartments, each containing three rigs with samples - Fig. 2.4 - 2.6. The vertical and horizontal cross section of the model of the rig is shown in Fig. 2.7, 2.8. Its simulation is adopted taking into account the following circumstances. Naturally, it contains the section with samples to house the desirable number of specimens. An electrical heating system as well as the temperature control system should also be integrated in the rig design. The section with samples, in its turn, consists of the external rig wall and internal capsule with samples, surrounded by electrical heaters. The gas gap (filled with helium) is foreseen between the rig wall and the capsule with samples to provide the required temperature level for each rig. In the present work a simplified simulation of the gas gaps and electrical heaters is adopted: these are considered as layers of defined thickness with corresponding properties – Fig. 2.7, 2.8. The rigs are positioned with equal gaps between them. The gap width in Z-direction is equal to 1 mm. The gas gaps of 0.5 mm in X-direction are also provided between the rigs and the stiffening walls – Fig. 2.5, 2.6. The lower axial reflector is simulated as a single bloc with appropriate channels for the helium flow – Fig. 2.9. The upper axial reflector is split into several single parts according to the number of rigs – Fig. 2.10. This design enables one to redistribute the gas flow between the compartments with rigs. So, the reflector sections are simultaneously used as elements for smoothing the velocity and pressure fields at the entry to the section with irradiated samples. The lateral reflector of 100 mm thick around the test section increases the dpa-rates in the irradiation specimens. Helium cooling of these reflectors is provided via channels by a bypass to the main flow – Fig. 2.11, 2.12. The reflector

is simulated as a solid structure with the properties of the T91-type steel. The capsules have a length of 125 mm and are closed by two cup-shaped caps – Fig. 2.7. The volume with samples is also simulated as a solid structure, whose properties are estimated taking into account that 20% of the volume is filled with a liquid metal (properties assumed to be those of NaK) and 80% is filled with a stainless steel. The properties of the regions composed of different materials, are calculated as a combination of the properties for these materials, e.g., for a property P:

$$P = \sum x_i * P_i ,$$

where  $x_i$  is the volume fraction of the  $i$ 'th material and  $P_i$  is the property P of the  $i$ 'th material. The wall material of the gas supply system and the test section is 316L-type stainless steel. Two baffles inserted in the 180° bend of the gas supply system to improve the uniform feeding of helium are also simulated – Fig. 2.13. The cooling helium thermal conductivity and the stainless steel thermal conductivity are approximated as follows:

$$\lambda_{He} = 0.56 + 0.00031 * T,$$

$$\lambda_{SS} = 10.5 + 0.015 * T,$$

where T is the absolute temperature, K.

The heat source distribution due to nuclear heating in the test section and in the reflector is obtained from the nuclear calculations using the MCNP code [2]. An interface program was elaborated to transfer the heat source distribution, obtained in nuclear calculations, to the calculation domain used in thermohydraulic analysis. The dimensions of the calculation domain used by the MCNP code are 250×150×75 mm for the X, Y, Z co-ordinate axes, respectively. For the remaining part of the test section volume and reflector, the heat source distribution is extrapolated assuming a law of  $1/r^2$ , where r is the distance along the corresponding co-ordinate axis. The model presented is used for thermohydraulic simulation of the HFTM.

### 2.3 The first results of the simulation

The first thermohydraulic analysis is carried out to obtain the velocity, pressure and temperature distribution in the test module. The calculations have been done with the STAR-CD code, version 3.15 [3] using the k-e high Reynolds number turbulence model of Chen. Below the main results of this simulation are presented and discussed.

1. The horizontal cross section of the HFTM is shown in Fig. 2.5. The most heavily loaded rig (from the thermal loads point of view) is denoted by number 2 (or 3 because of symmetry) in this figure. The results discussed below are mainly related to this rig. The results are obtained for the case of the nuclear heating only, nuclear heat source distribution is shown in Fig. 2.14. Fig. 2.15 shows the temperature distribution in the volume with samples and in the rig walls. One can see that the temperature distribution in the samples correlates with the nuclear heat source distribution. The temperature distribution in the rig walls (Fig. 2.15b) shows that the temperature field is more non-symmetrical than in the volume with samples. It can be explain by the fact that the helium flow is heated up from the inlet to the outlet of the test section resulting in the temperature field “deformation”.

2. On the other hand, the temperature distribution in the stiffening plate dividing the test section into compartments differs significantly from the temperature distribution in the samples and rig wall. The temperature rises continuously in the direction of the helium flow. One can see the hot spots along the wall on the places where the wall contacts the stiffening ribs foreseen at the rig walls, Fig. 2.16. These places are intensively heated because of the nuclear heating of the wall and ribs. At the same time, this region has insufficient cooling. The reason of this fact is discussed below.

3. The cooling system of the IFMIF test section consists of a number of parallel channels, Fig. 2.5, 2.6. These channels have common inlet chamber and common outlet chamber and are of two types: “narrow” channels of 0.5 mm wide and “wide” channels of 1 mm wide. The pressure drop between the inlet and outlet chambers is the same for all the cooling channels. The helium flow is distributed between the cooling channels according to the pressure drop. As the cooling channels have the same length, a velocity value in the “narrow” channels should be lower than in the “wide” channels. The calculated results confirm this, Fig. 2.17. One can see the significant difference of the flow velocity in the cooling channels. The turbulent kinetic energy production is also lower in the “narrow” channels, Fig. 2.18. So, the flow pattern is quasi-laminar in the “narrow” channels that results in insufficient cooling of the wall and heating up of the helium flow in these channels. The temperature distribution of the helium flow in the cooling channels as well as at the outlet of the cooling channels is presented in Fig. 2.19, 2.20, respectively. One can see that the flow temperature can reach  $\sim 137^{\circ}\text{C}$  in the “narrow” channel at the averaged outlet temperature of  $\sim 88^{\circ}\text{C}$ . That is why the temperature of the stiffening plate is so high. This temperature difference can result in significant thermal stress of the wall.

4. The possible ways to decrease the flow temperature in the “narrow” channel may be the following:

- increase in the helium flow rate;
- using the rig vessel without ribs;
- using the rig vessel with discontinuous ribs.

All these possibilities are considered below.

## **2.4 Optimisation of the stiffening wall temperature**

Additional numerical simulation was carried out for the HFTM optimised design under another operation conditions and for some modification of the rig wall design aimed at reduce in the temperature of the stiffening plates. The results obtained are discussed in this section.

### ***2.4.1 Comparison of turbulence models for thermohydraulic simulation***

The thermohydraulic calculations of the high flux test module (HFTM) have been performed with a new version of the STAR-CD code – 3.20, which now is available [4]. First of all, the results are compared with those obtained with the previous version of the STAR-CD [3]. The conclusion is the following. The temperature distribution in the model simulated is practically the same as was obtained with a previous version of the STAR-CD code. As for pressure drop and velocity distribution, their values are different. For example, the pressure drop and the maximum velocity in the model, obtained with the new version of the code are lower than for the previous version of

the code by 6.5% and 16.5%, respectively. The calculations have been performed using the Chen k-e high Re number turbulence model under the condition of the nuclear heating only. For comparison additional calculations are done with another turbulence models under the same operation conditions. Some results of the calculation are summarised in Table 1.

Table 1. Main calculated results obtained for the HFTM with different turbulence models

Parameter	Turbulence model				
	Standard k-e high Re number	k-e high Re number non-linear	Chen k-e high Re number	RNG	V2F
$W_{\max}$ , m/s	346.9	349.4	346.2	343.4	566.7
$\Delta P$ , bar	0.702	0.711	0.7	0.653	0.8
$T_s^{\max}$ , °C	386.9	386.3	391	389.8	404.7
$T_h^{\max}$ , °C	371.3	370.7	375.5	374.2	390.2
$T_w^{\max}$ , °C	379.5	378.9	383.6	382.3	398
$T_r^{\max}$ , °C	142.7	141.8	142.2	145.4	131.5
$T_f^{\max}$ , °C	131.4	130.9	131	132.2	131.3

The following nomenclature is used.

$W_{\max}$  is the maximum velocity of the helium flow in the HFTM,

$\Delta P$  is the pressure drop in the model,

$T_s^{\max}$  is the maximum temperature of the volume with samples,

$T_h^{\max}$  is the maximum temperature of the electrical heaters,

$T_w^{\max}$  is the maximum temperature of the container and rig wall,

$T_r^{\max}$  is the maximum temperature of the reflector,

$T_f^{\max}$  is the maximum temperature of the helium flow.

One can see that the results obtained with the V2F model differ significantly from those obtained with the another models. Moreover, the detailed analysis shows that the velocity and pressure distribution in the model is highly non-uniform in the test section, see Fig. 2.21, where the results obtained with the Chen k-e high Re number turbulence model are also presented for the comparison. At the same time, the pressure drop in the HFTM obtained with the V2F turbulence model is significantly higher and this circumstance should result in more uniform pressure and velocity distribution in the model. This discrepancy is difficult to explain, might be it is concerned with a problem of the implementation of this turbulence model in the new version of the STAR-CD code. For this reason for the further calculations the V2F turbulence model is not used. The results obtained with the k-e high Re number models correlate each other well and the Chen k-e model is chosen for further thermohydraulic analysis.

#### 2.4.2 Stiffening plate temperature.

The calculations have been done under the operation condition of the nuclear heating only. Firstly, the increase in the helium mass flow rate by 10% is simulated. The temperature distribution of the stiffening plate for the reference design, i.e. for the rig vessel with the ribs on the short side, is shown in Fig. 2.22a,b, as well as the

temperature of the helium flow at the outlet of the test section, Fig. 2.22c (the results are presented for rig 2, see Fig. 2.5). One can see in Fig. 2.22a and 2.22b that the temperature distribution is very similar for these cases. The influence of the increase in the mass flow rate results in the insignificant decrease in the wall temperature (by  $6^{\circ}\text{C}$ ). The temperature field of the helium flow at the outlet of the test section under the mass flow rate of 0.121 kg/s is similar to one for the mass flow rate of 0.11 kg/s, only the maximum flow temperature is by  $6.5^{\circ}\text{C}$  lower.

The velocity field in the “narrow” and “wide” cooling channels are presented in Fig. 2.23, 2.24 under the aforementioned mass flow rates. The velocity fields are similar with corresponding difference of the velocity values. Accordingly, the pressure loss in the model is 23.4% higher in the case of greater mass flow rate. So, one can expect that additional increase in the mass flow rate can result in a significant increase in the pressure loss (and increase in mechanical loads on the rig structure), while the wall temperature is decreased insignificantly.

The second case is the modified design using the rig vessel without the ribs on the short side. The calculations are carried out for two mass flow rates mentioned above and some results are presented in Fig. 2.25-2.27. The absence of the ribs results in slightly lower pressure loss in the model: 0.693 bar instead of 0.7 bar for the reference design. The wall temperature is noticeably decreased, by  $\sim 16^{\circ}\text{C}$  (or  $\sim 14\%$ ), see Fig. 2.22, 2.25.

The velocity field in the cooling channels at the outlet of the test section shows the following. The velocity distribution in the “narrow” channel is more uniform and the average velocity value is greater than for the reference design. At the same time, the velocity value in the “wide” channel is lower than for the reference design, that corresponds to the smaller pressure drop (see Fig. 2.23, 2.24 and Fig. 2.26, 2.27). The difference of the wall temperature as well as the difference of the pressure loss for two different mass flow rates are practically the same as for the reference design.

The third case is the rig vessel design with discontinuous ribs on the short side as shown in Fig. 2.28. Here the cases are simulated with two variants of discontinuous ribs – one consists of three sections of rib, each 10 mm long (case 3x10), the other consists of one section of rib 20 mm long located at the central section of the rig short side (case 1x20). The helium mass flow rate is equal to 0.11 kg/s. The results are the following.

The maximum temperature of the stiffening plate is higher than in case of the rig vessel without ribs on the short side, but it is lower than for the reference design, Fig. 2.29a. At the same time the case of discontinuous ribs 3x10 gives the results closer to the reference design and the case of discontinuous ribs 1x20 gives the results closer to the design of the rig without ribs on the short side. Similar results are also obtained for the pressure loss in the model. The temperature field of the helium flow at the outlet of the test section for the case 3x10 is shown in Fig. 2.29b. The example of the velocity distribution in the cooling channels at the outlet of the test section is presented in Fig. 2.30 (case 3x10). The results are intermediate between those for the reference design and the design of the rig vessel without ribs on the short side.

The main results are summarised in Table 2.

The calculations are repeated under the conditions of the nuclear and electrical heating for the temperature level in the volume with samples of  $\sim 650^{\circ}\text{C}$ , and the results are summarised in Table 3.

Table 2. Main calculated results for different rig vessel design. Nuclear heating only.

Parameter	Design					
	Reference		Rig vessel without ribs		Discontinuous ribs	
					3x10	1x20
$G_{\text{He}}$ , kg/s	0.11	0.121	0.11	0.121	0.11	0.11
$W_{\text{max}}$ , m/s	346.2	399.8	346	397.5	346.3	345.5
$\Delta P$ , bar	0.7	0.864	0.693	0.85	0.998	0.695
$T_s^{\text{max}}$ , $^{\circ}\text{C}$	391	382.5	387.2	383.1	387	386.9
$T_h^{\text{max}}$ , $^{\circ}\text{C}$	375.5	366.9	371.5	367.5	371.4	371.3
$T_w^{\text{max}}$ , $^{\circ}\text{C}$	383.6	375.1	379.3	375.7	379.5	379.5
$T_r^{\text{max}}$ , $^{\circ}\text{C}$	142.2	135.8	140.1	134	140.8	140.6
$T_f^{\text{max}}$ , $^{\circ}\text{C}$	131	123	123	115.3	127.7	126.5
$T_{\text{st}}^{\text{max}}$ , $^{\circ}\text{C}$	119.4	113.5	100.4	95.5	106.6	101.8

The nomenclature is the same as for Table 1, and  $T_{\text{stmax}}$  is the maximum temperature of the stiffening wall.

Table 3. Main calculated results for different rig vessel design. Nuclear and electrical heating at the temperature level of  $\sim 650^{\circ}\text{C}$  in the volume with samples.

Parameter	Design			
	Reference	Rig vessel without ribs	Discontinuous ribs	
			3x10	1x20
$G_{\text{He}}$ , kg/s	0.11	0.11	0.11	0.11
$W_{\text{max}}$ , m/s	397	396.5	396.8	395.8
$\Delta P$ , bar	0.77	0.76	0.764	0.76
$T_s^{\text{max}}$ , $^{\circ}\text{C}$	655.2	656.6	656.3	655.8
$T_h^{\text{max}}$ , $^{\circ}\text{C}$	648.4	649.4	649.5	649.3
$T_w^{\text{max}}$ , $^{\circ}\text{C}$	650.2	651.3	651.3	651.1
$T_r^{\text{max}}$ , $^{\circ}\text{C}$	175.3	168.3	169.1	169.6
$T_f^{\text{max}}$ , $^{\circ}\text{C}$	217.4	209.3	215.3	213.5
$T_{\text{st}}^{\text{max}}$ , $^{\circ}\text{C}$	224.3	173.7	199.3	177

So, the conclusion of this section is the following.

The increase in the helium mass flow rate results in increase in the pressure loss in the model and increase in the loads on the rig structure, while the maximum temperature is decreased insignificantly.

The absence of the ribs on the rig vessel results in a significant decrease in the stiffening wall temperature and in insignificant decrease in the pressure loss. On the other hand, the absence of the ribs makes rig vessel less stiff and a significant deformation of the vessel can take place. Additional stress analysis is desirable. The

case with discontinuous ribs (for example, case 1x20) can be considered as alternative variant to the rig design without ribs.

The maximum temperature of the stiffening plate occurs approximately at the section opposite to the middle of the short side of the rig vessel even in the case of the vessel without ribs. This can be explained by the fact that this section is more intensive heated due to nuclear heating.

## 2.5 Influence of the electrical heaters

The nuclear heat source distribution in the HFTM test section is non-uniform in all three directions, Fig. 2.14. So, the temperature distribution in different rigs should also be non-uniform under the nuclear heating only. Fig.2.31 shows the temperature distribution in rig 2 and rig 9 (see Fig. 2.5) under this condition. The character of the temperature distribution is similar for both rigs, but temperature level is different. The temperature of rig 9 is 76 – 152 °C lower than the temperature of rig 2. One can also observe the high temperature gradient in the volume with samples and low the maximum temperature, not higher than 400°C even in the most heated rig 2.

To reduce the temperature gradient and to increase the temperature level the electrical heater is foreseen [1]. It consists of three sections (bottom, middle and top) with different heating power. One can reach the desirable temperature of the volume with samples varying the power of the electrical heaters. Fig. 2.32 shows the temperature distribution in the volume with samples under nuclear and electrical heating. Only two electrical heaters are switched on (bottom and top) with the heating power of 74 and 71 W/cm<sup>3</sup>, respectively. The temperature distribution is now more uniform and the temperature level is higher, up to ~450 °C for rig 2. At the same time, the maximum temperature in the volume with samples of rig 9 remains significantly lower than 450°C, and the temperature gradient in this rig is rather high.

To reach the temperature level of ~ 650°C all the electrical heaters must be into operation with a higher heating power. The calculations have been performed under the nuclear and electrical heating with the heater's power of 158, 90 and 149 W/cm<sup>3</sup> for the bottom, middle and top heaters, respectively [1]. The heater power is the same for all the rigs. One can see in Fig. 2.33 that the maximum temperature in the volume with samples reaches 655°C for rig 2. At the same time, the maximum temperature in the volume with samples of rig 9 is by 92°C lower. This means that the electrical heater power should be fitted for different rigs to reach a target temperature in the volume with samples of particular rig.

The temperature distribution in the volume with samples under electrical heating only is presented in Fig. 2.34. The heater's power (206, 199 and 194 W/cm<sup>3</sup> for the bottom, middle and top heaters, respectively [1]) is chosen to reach the temperature level of about 650°C. This power is applied to all the rigs. Nevertheless, the temperature level is slightly varied from rig to rig. This can be explained by the influence of the neighbour rigs. The rigs of the second row have higher temperature (by about 10°C).

## 2.6 Choice of an appropriate power of the electrical heaters.

Additional calculations are carried out to choose the appropriate power of the electrical heaters to reach the target temperature for all the rigs. The simulation model is slightly modified to be closer to the reference design and the calculations have been done. The simulation model modification is concerned with a more accurate simulation of the insulation gap between the rig wall and the capsule with samples. The gap is filled with the helium and now the helium thermal conductivity is considered as function of the temperature. The effective thickness of the gap is adopted to be equal to 0.5 mm. The electrical heaters power is estimated for the temperature level of 450<sup>0</sup>C and 650<sup>0</sup>C in the volume with samples. The results of the calculation are presented in Table 4 and in Fig. 2.35, 2.36. One can see very similar temperature distribution in the volume with samples practically in all the rigs. On the other hand, one should note that the middle section of the electrical heater can not be into operation only for the rigs 2 and 3 at the temperature level of 450<sup>0</sup>C. As for another rigs, all three sections of the electrical heaters are into operation even at the temperature of 450<sup>0</sup>C.

Note. The thermohydraulic simulation is done with the k-e high-Re-number turbulence model of Chen. For more accurate choice of the electrical heaters power the simulation with the k-e low-Re-number is desirable.

Table 4. Electrical heater power for the rigs of the HFTM.

Rig	$q_b \cdot 10^{-7}, \text{W/m}^3$		$q_m \cdot 10^{-7}, \text{W/m}^3$		$q_t \cdot 10^{-7}, \text{W/m}^3$	
	T = 450 <sup>0</sup> C	T = 650 <sup>0</sup> C	T = 450 <sup>0</sup> C	T = 650 <sup>0</sup> C	T = 450 <sup>0</sup> C	T = 650 <sup>0</sup> C
Rig 1,4	8.1	16.7	1.6	10.5	7.6	15.6
Rig 2,3	7.4	15.8	0	9.2	7.1	14.9
Rig 5,8	8.2	16.8	3.9	12.8	7.6	15.4
Rig 6,7	7.4	15.9	2.5	11.3	6.9	14.6
Rig 9,12	8.9	17.4	6.1	15.1	8.3	16.3
Rig 10,11	8.1	16.7	4.8	13.8	7.8	15.7

$q_b$ ,  $q_m$ ,  $q_t$  – is the power of bottom, middle and top sections of the electrical heater, respectively.

Rig numbering corresponds to Fig.2.5.

## 2.7 Simulation of the IFMIF/HFTM with deformed cooling channels

The operation conditions of the IFMIF/HFTM are very severe. Significant mechanical and thermal loads can result in the deformation of the rig walls and, hence, result in the deformation of the cooling channels. The cooling channels of the IFMIF/HFTM have a rectangular cross section, being 0.5 mm wide on the short side of the rig and 1 mm wide on the long side of the rig (reference design). So, even a small deformation of the cooling channels results in a significant change in the channel cross section area, which, in its turn, can change the thermohydraulic characteristics of the HFTM. This work is done to estimate the influence of the cooling channels deformation on the thermohydraulic characteristics of the HFTM.

### ***2.7.1 Simulation of the cooling channels deformation for all channels of the model***

The simulation of this part is carried out with the commercial CFD code STAR-CD, version 3.15 [3]. The following assumptions are made:

- the dimensions of the cooling channels at the inlet to the test section are not changed and are adopted as for the reference design, Fig.2.37a;
- the remaining part of the section of the cooling channels is changed, but because the shape of the deformed channels is not exactly known, the width of the channel is simply reduced, except for the rib section, Fig. 2.37b,c;
- two variants are simulated: the channel width is reduced by 10% and by 20% of the reference value;
- nuclear heating only is considered as the thermal loads;
- the mass flow rate is constant.

Below the results are presented for several cases.

Case 1. Reference design of the cooling channels.

Case 2. The width of the cooling channel on the long side of the rig is reduced by 10%, i.e. 0.9 mm instead of 1 mm. The width of the cooling channel on the short side of the rig is unchanged.

Case 3. The width of the cooling channel on the long and short sides of the rig is reduced by 10% (1mm  $\rightarrow$  0.9mm, 0.5mm  $\rightarrow$  0.45mm) compared with the reference design.

Case 4 . The same as in case 3, but without ribs on the short side of the rig.

Case 5. The width of the cooling channel on the long side of the rig is reduced by 20%, i.e. 0.8 mm instead of 1 mm. The width of the cooling channel on the short side of the rig is unchanged.

Case 6. The width of the cooling channel on the long and short sides of the rig is reduced by 20% (1mm  $\rightarrow$  0.8mm, 0.5mm  $\rightarrow$  0.4mm) compared with the reference design of the rig.

Case 7. The same as in case 6, but without ribs on the short side of the rig.

The main results of the calculation are summarised in Table 5.

Table 5. Results of the calculation (nuclear heating only).

Parameter	Case						
	Case 1	Case 2	Case 3	Case 4	Case 5	Case 6	Case 7
$W_{\max}$ , m/s	402.5	404.6	409.8	405.6	441.1	483.8	478
$W_{\max}^{\text{ref}}$ , m/s	332.8	385.3	392	390.6	458.1	510.9	505
$\Delta P$ , bar	0.745	0.9	0.928	0.918	1.08	1.25	1.24
$T_s^{\max}$ , °C	386.2	376.9	375.5	375.2	380.3	382.3	383.6
$T_w^{\max}$ , °C	380.4	369.3	367.9	367.6	372.8	374.6	376
$T_h^{\max}$ , °C	372.4	360.9	359.6	359.3	364.5	366.2	367.5
$T_r^{\max}$ , °C	155	149.9	150.6	148.1	148.0	157.3	154.1
$T_f^{\max}$ , °C	152.5	147.5	147.4	137.1	149.3	162.9	159.2

The following nomenclature is used.

$W_{\max}$  is the maximum velocity of the helium flow in the HFTM,

$W_{\max}^{\text{ref}}$  is the maximum velocity of the helium flow in the reflector cooling channels,

$\Delta P$  is the pressure drop in the model,

$T_s^{\max}$  is the maximum temperature of the volume with samples,

$T_h^{\max}$  is the maximum temperature of the electrical heaters,

$T_w^{\max}$  is the maximum temperature of the capsule wall,

$T_r^{\max}$  is the maximum temperature of the reflector,

$T_f^{\max}$  is the maximum temperature of the helium flow.

### 2.7.2 Comments on the results.

The results presented in Table 5 and in Fig. 2.38 - 2.40 show the following. The cooling channels deformation results in the flow redistribution between the channels depending on the case considered. The flow is also redistributed between the main flow and the flow in the lateral reflector. First of all, let us compare the reference design and the cases with cooling channels reduced by 10%. The maximum velocity of the fluid flow in the test section differs insignificantly for these cases, but the flow averaged velocity in the test section and the velocity of the flow in the lateral reflector have a noticeable difference. The effect of this difference is increased pressure loss in the model. This difference reaches  $\approx 25\%$  between the reference design and case 3 (Table 5). As for the temperature of the solid structure, it is even lower for the cases with deformed cooling channel in comparison with the reference design. This fact can be explained by more intensive cooling of the structure because of increased flow velocity. The maximum flow temperature in case 4 is  $10^{\circ}\text{C}$  lower than that in cases 2 and 3, where the temperature distribution is very similar. The flow temperature reaches its maximum value in the cooling channels on the short sides of the rigs located near the lateral reflector, Fig. 2.38. The rig has no rib on the short side in case 4 and the fluid flow is less laminarized in the cooling channels, that results in reduced flow temperature.

In the cases with the cooling channels reduced by 20% the flow is further redistributed. The pressure loss exceeds 1 bar, and the maximum velocity is now in the channels of the lateral reflector. The main flow velocity is also increased, but a significant part of the flow passes through the lateral reflector. The temperature of the solid structure is increased and is close to the temperature of the reference design.

The temperature distribution of the rig walls is presented in Fig. 2.39, 2.40 for all the cases considered. One can see that the wall temperature reaches its maximum on the short side of the rig near the ribs. The absence of the ribs results in a decrease in the wall temperature by  $7^{\circ}\text{C}$  -  $10^{\circ}\text{C}$ , Fig. 2.39 case 3, 4 and Fig. 2.40 case 6, 7.

So, the decrease in the cooling channel cross section by 20% may be dangerous because of increased hydrodynamical and mechanical loads to the structure.

### ***2.7.3 Simulation of individual rig dimension deviations from the reference design.***

The next step of the work is simulation of individual rig dimension deviations from the reference design. This deviation can be caused by the operation conditions as well as can result from the fabrication tolerance. To estimate the influence of the local deviation of the rig from the reference design on the temperature field, the rig 2 (see Fig. 2.5) is chosen for the analysis.

The following cases are simulated:

Case 8. The cooling channels of rig 2 on long sides are decreased by 10% (1 mm  $\rightarrow$  0.9 mm) and insulation gas gap between the rig vessel and the capsule with samples is increased by 0.1 mm accordingly. The nuclear heating only is the operation condition.

Case 9. The cooling channel width is equal to the reference design value, but the insulation gas gap between the rig vessel and the capsule with samples is increased by 10% under nuclear heating only.

Case 10. The same as the case 9, only the insulation gas gap between the rig vessel and the capsule with samples is decreased by 10%.

Cases 11 – 13 are the same as the cases 8-10, but electric heating is added to the nuclear one to reach the temperature level in the volume with samples  $\sim 650^{\circ}\text{C}$ .

The following results are obtained.

In Fig. 2.41, 2.42 the temperature distribution is shown for the volume with samples and the capsule walls for case 8. One can see a non symmetrical character of the temperature field in the first row of rig. The volume with samples and wall of the capsules of the rig 2 have higher temperature than another rigs. The temperature distribution in the second (and third) rows of the rig is already symmetrical. The difference of the maximum temperature between rig 2 and rig 3 is  $\sim 11^{\circ}\text{C}$  for the volume with samples, and  $\sim 14^{\circ}\text{C}$  for the capsule walls.

The results of the calculation for case 9 and 10 show more significant difference of the temperature field in the model (relatively to the reference design) in comparison with case 8, see Fig. 2.43 and Table 6. At the same time, the character of the temperature distribution in case 8 is similar to case 9. The temperature of the rig 2 in case 10 is lower accordingly, but relative difference is higher, than in case 9, see Table 6. The temperature of the flow and reflector is practically not affected by these rig dimension deviations.

Compare the results of the calculation for cases 8-10 one can see more significant influence of the insulation gas gap on the temperature distribution. In case 8 the

cooling channels are decreased by 10% on both large sides of the rig and gas gap is changed accordingly. But the increase of the gas gap is about 7.4% whereas in case 9 it is 10%. The influence of the cooling channels deformation is less significant.

The calculations are repeated under the operation conditions with nuclear and electrical heating. The power of electrical heaters is taken from [1]. Electrical heater consists of three parts –top, middle and bottom- with the power density of 149/ 90/ 158 W/cm<sup>3</sup>, respectively. All three sections of electrical heater are into operation. The results show a similar influence of the insulation gas gap and cooling channels on the temperature field. Some results of the calculations are shown in Fig. 2.44, 2.45 and are summarised in Table 7.

Table 6. The main results of the calculation for deviation of the dimension of rig 2 from the reference design (nuclear heating only).

Parameter	Case						
	Ref. design	Case 8		Case 9		Case 10	
		value	Rel. to ref. design, %	value	Rel. to ref. design, %	value	Rel. to ref. design, %
$W_{max}$ , m/s	344.6	348.2	1.04	344.7	0.03	344.5	-0.03
$\Delta P$ , bar	0.696	0.707	1.58	0.696	0	0.696	0
$T_s^{max}$ , °C	385.5	389.9	1.14	400	3.76	360.5	-6.48
$T_w^{max}$ , °C	377	382.5	1.46	393	4.24	352.8	-6.42
$T_h^{max}$ , °C	368.1	374.4	1.71	384.9	4.56	344.4	-6.44
$T_r^{max}$ , °C	142.1	141.8	-0.21	142.4	0.21	142.4	0.21
$T_f^{max}$ , °C	130.8	130.2	-0.46	130.9	0.08	130.9	0.08

Table 7. The main results of the calculation for deviation of the dimension of rig 2 from the reference design (nuclear and electrical heating).

Parameter	Case						
	Ref. design	Case 11		Case 12		Case 13	
		value	Rel. to ref. design, %	value	Rel. to ref. design, %	value	Rel. to ref. design, %
$W_{max}$ , m/s	397	400.3	0.83	396.5	-0.12	396.1	-0.23
$\Delta P$ , bar	0.77	0.78	1.29	0.77	0	0.77	0
$T_s^{max}$ , °C	655.2	679.5	3.71	699.8	6.81	618.7	-5.57
$T_w^{max}$ , °C	650.2	674.9	3.8	693.6	6.67	614.8	-5.44
$T_h^{max}$ , °C	648.4	673.4	3.86	691.9	6.7	612.8	-5.49
$T_r^{max}$ , °C	175	174.9	-0.06	175.4	0.23	175.3	0.17
$T_f^{max}$ , °C	217.4	219.3	0.87	218.4	0.46	217.3	-0.046

The nomenclature is the same as for Table 1, only  $T_s^{max}$ ,  $T_w^{max}$ ,  $T_h^{max}$  are taken for rig 2 (see Fig. 2.5).

The temperature distribution of the fluid flow for cases under nuclear and electrical heating differs from that for cases under nuclear heating only. The maximum value of the flow temperature is reached in the cooling channels on the short side of the rig 2 and 3 for all the cases under nuclear and electrical heating (Fig. 2.46), whereas the maximum flow temperature under nuclear heating only is observed in the cooling channels of the short sides of the rigs located near the lateral reflectors, Fig. 2.38.

*Conclusion to the section.*

- The decrease in the cooling channels cross section by 20% may be dangerous because of increased hydrodynamical and mechanical loads to the structure.
- The decrease in the cooling channel cross section by 10% may be considered as acceptable. The deviation of the gas gap thickness inside the rig from the reference value affects the temperature distribution in the model more significant than cooling channel deformation.

## **2.8 Influence of the heat from the target back wall on the HFTM.**

The HFTM is located as close as possible (within about 2mm) to the target back wall to receive maximum neutron fluence [5]. The temperature of the target back wall is close to the one of the lithium flow. The Li flow temperature is equal to 250<sup>0</sup>C at the inlet and is about 300<sup>0</sup>C at the outlet of the target. On the other hand, the helium flow temperature at the inlet to the HFTM is chosen to be equal to 50<sup>0</sup>C. In this connection it is important to estimate the influence of the target back wall on the thermal-hydraulic characteristics of the HFTM, because all previous calculations are done without taking into account the heat transfer from the back wall to the HFTM.

The main dimensions of the back wall section simulated for the calculation are presented in Fig. 2.47, 2.48. The remaining part of the back wall has significantly larger gas gap between its back side and the HFTM, so it is not simulated. The properties of the back wall material are taken those of stainless steel. The gap between the back wall and the HFTM is also simulated as a flat gas gap of 1 mm thick. The properties of the gas are taken those of the helium at the near atmospheric pressure. The isometric view of the model simulated is shown in Fig.2.49. The boundary conditions of the target back wall section simulated are shown in Fig. 2.50.

The results of the calculation are presented in Fig. 2.51- 2.53 and in Table 8.

It should be noted that the heat of the target back wall affects only the front wall temperature of the HFTM, the temperature of the helium flow in the cooling channels nearest to the HFTM front wall and temperature of the reflector. Fig. 2.51 and 2.52 show that the maximum temperature of the HFTM front wall is increased by 19.2<sup>0</sup>C and the maximum flow temperature in the first line of the cooling channels is increased by 17.1<sup>0</sup>C. The maximum temperature of the reflector is increased by 18.3<sup>0</sup>C. The comparison is presented for the case under nuclear heating only. The temperature distribution in other elements of the HFTM is practically the same as without the heat of the target back wall, Table 8. This means that the gas gap between the back wall and the HFTM is rather good insulation. The temperature distribution in the gas gap is shown in Fig. 2.53. If the gap thickness is increased to 2 mm, the effect of heat of the target back wall will be less significant.

Table 8. Comparison of the main thermal-hydraulic characteristics of the HFTM without and with the heat of the target back wall.

Parameter	Without a heat of the back wall	With a heat of the back wall
$W_{\max}$ , m/s	344.6	349.8
$\Delta P$ , bar	0.696	0.706
$T_s^{\max}$ , $^{\circ}\text{C}$	385.5	384.1
$T_w^{\max}$ , $^{\circ}\text{C}$	368.1	366.9
$T_h^{\max}$ , $^{\circ}\text{C}$	377	376
$T_f^{\max}$ , $^{\circ}\text{C}$	142.1	160.4
$T_{\text{fw}}^{\max}$ , $^{\circ}\text{C}$	118.3	137.5
$T_{\text{fl-1}}^{\max}$ , $^{\circ}\text{C}$	90.82	107.9

$T_{\text{fw}}^{\max}$  is the maximum temperature of the HFTM front wall,

$T_{\text{fl-1}}^{\max}$  is the maximum temperature of the flow in the first line of the cooling channels.

The remaining nomenclature is the same as in Table 1.

**Note.**

1. The effective thickness of the gas gap inside the rigs is equal to 0.5 mm in the process of the calculation carried out.
2. The calculations are done with the high Reynolds number k-e turbulence model (Chen modification of the standard k-e turbulence model is used). It is desirable to repeat these calculations for individual rig with a low Reynolds number turbulence model and with more fine and more detailed simulation of the rig design.

*Conclusion to the section.*

The simulation carried out shows the following.

The heat of the target back wall results in a rise of the maximum temperature of the HFTM front wall by  $19.2^{\circ}\text{C}$  and the maximum flow temperature in the first line of the cooling channels by  $17.1^{\circ}\text{C}$ . The temperature distribution in other elements of the HFTM is practically the same as without the heat of the target back wall. There is some reserve to reduce the effect of the heat of the target back wall on the HFTM – gas gap thickness between the back wall and the HFTM can be increased to 2 mm.

**2.9 Optimization of the IFMIF lateral reflector cooling system.**

The IFMIF test section is surrounded by the reflector to enlarge the neutron fluence in the volume with samples. The reflector consists of three sections: the top, the bottom and the lateral section. The reflector is heated by the nuclear heating and should be cooled. The top and bottom sections are cooled with the main helium flow, whereas the lateral one is cooled by a bypass flow. The bypass flow is supplied and removed via horizontal flat gaps. The cooling system of the lateral reflector consists of several cooling channels, each of them is a vertical gap 1 mm wide. The optimisation of the lateral reflector cooling system is important because the non-uniform temperature distribution in it can result in significant thermal stress and deformation of the test cell itself.

The results of numerical study of the cooling system of the lateral reflector for optimization of the temperature distribution in it is presented in this section. The axial (vertical) temperature distribution in the lateral reflector depends on the flow temperature increment in the model. So, the main attention is concentrated on the optimization of the temperature distribution in the horizontal direction.

One of the variants of the lateral reflector cooling system is shown in Fig. 2.12. Preliminary calculation showed that the cooling system of the lateral reflector should consist of at least three cooling channels. These channels were placed at 20, 50 and 80 mm from the section with samples. This case is named as reference design. The temperature distribution is presented in Fig. 2.54 for this case. One can see that the temperature distribution is non-uniform and the temperature of the lateral reflector reaches its maximum value ( $\sim 155^{\circ}\text{C}$ ) directly near the IFMIF test section. This is not favorable from the thermal stress point of view. For this reason a number of variants were tested with another location of the cooling channels. Some of them are discussed below.

The variants with 3 and 4 cooling channels were investigated. The cases differ from each other by the locations of the cooling channels with respect to the test section as shown in Fig. 2.55. The main cases considered are summarized in Table 9.

Table 9. Main cases considered for optimization of the cooling system of the lateral reflector.

<b>Case</b>	<b>a</b>	<b>b</b>	<b>c</b>	<b>d</b>	<b>e</b>
Case 0	-	20	50	80	-
Case 1	7	-	50	80	-
Case 2	7	30	-	80	-
Case 3	7	20	50	-	-
Case 4	7	30	65	-	-
Case 5	10	35	-	75	-
Case 6	7	20	50	80	-
Case 7	7	20	40	80	-
Case 8	7	20	45	80	-
Case 8m	7	20	45	80	19

Note. Dimensions of **a**, **b**, **c**, **d** and **e** are in mm.

The calculated temperature distribution is shown in Fig. 2.56, 2.57. One can see that the most appropriate case with 3 cooling channels is case 5 with the cooling channel location at 10, 35 and 75 mm from the test section. Under these conditions the maximum temperature of the lateral reflector is equal to  $134.9^{\circ}\text{C}$ , that is  $20^{\circ}\text{C}$  lower than for the case 0. On the other hand, this temperature can be decreased to  $\sim 120^{\circ}\text{C}$  with the use of 4 cooling channels located at 7, 20, 45 and 80 mm from the test section, case 8, and the temperature can be decreased to  $\sim 112^{\circ}\text{C} - 114^{\circ}\text{C}$  with modified cooling system – case 8m, case 8mn. It should be noted that for case 8m the maximum temperature of the reflector takes place in the volume of the top axial reflector (see Fig. 2.57b) because the temperature of the helium main flow is increased and the bypass helium flow rate is increased decreasing the temperature of the lateral reflector.

As was mentioned, the bypass flow is supplied and removed via the flat gaps. Initially, the height of these gaps ( $h$  in Fig. 2.58) was adopted to be 4 mm. The case with  $h = 2$  mm is also calculated to understand the influence of this parameter on the temperature distribution. The result is the following: the temperature distribution in the lateral reflector is practically unchanged. The difference of the maximum temperature of the lateral reflector in the case of  $h = 2$  mm and  $h = 4$  mm is equal to 2.60C. At the same time, the hydraulic resistance of the cooling system of the lateral reflector is increased under  $h = 2$  mm, that results in the redistribution of the helium flow between the main and bypass flows. The maximum velocity of the main flow is 2.7% higher in the case of  $h = 2$  mm. The temperature of other elements of the model is very close. The cross section area of the modified cooling system (case 8m) is increased and its hydraulic resistance is decreased. The helium flow is redistributed between the main flow of the test section and the bypass flow of the lateral reflector, Table 10. This fact can result in increase in the temperature non-uniformity in the volume with samples, because the lower temperature remains the same and the higher temperature can increase (main stream mass flow rate is decreased, Table 10). Nevertheless, the temperature distribution in the volume with samples is changed insignificantly, see Table 11. Moreover, if the helium total mass flow rate is increased by 15%, the temperature distribution and non-uniformity is practically the same as in the reference case.

The main calculated results are summarized in Table 11.

Table 10. Helium bypass flow in % to the total mass flow rate

Case	Ref. design	Case 8	Case 8m	Case 8mn
$G_{\text{bypass}}/G_{\text{total}}, \%$	22.3	28.4	33.4	33.4

Note. Case 8mn is the same as Case 8m, only the total helium mass flow rate is increased by 15% to the reference value.

Table 11. The main calculated results for different cases of the lateral reflector cooling system.

Parameter	$W_{\text{max}}, \text{m/s}$	$T_{\text{fl}}^{\text{max}}, ^\circ\text{C}$	$T_{\text{s}}^{\text{max}}, ^\circ\text{C}$	$T_{\text{w}}^{\text{max}}, ^\circ\text{C}$	$T_{\text{h}}^{\text{max}}, ^\circ\text{C}$	$T_{\text{ref}}^{\text{max}}, ^\circ\text{C}$
Case 0	402.5	152.5	388.2	380.6	372.4	155
Case 1	400	136.7	388.2	380.7	372.5	168
Case 2	404.6	136.7	388.2	380.6	372.4	155.7
Case 3	395.7	137.2	388.3	380.8	372.5	217.2
Case 4	400.7	136.8	388.3	380.8	372.6	161
Case 5	401.2	136.8	388.3	380.8	372.5	134.9
Case 6	367	138.1	389.9	382.4	374.2	128
Case 7	363.2	138.2	390.1	382.5	374.3	129.3
Case 8	363.1	138.2	390.2	382.5	374.3	120.2
Case 8a	372.8	137.9	389.6	382.1	373.8	122.8
Case 8m	319.2	140.1	392.5	385	376.8	114.2
Case 8mn	389.9	137.2	388.8	381.3	373.1	112.4

Note. Case 8a corresponds to the cooling system with 4 cooling channels located at 7, 20, 45 and 80 mm from the test section and  $h = 2$  mm. Case 8mn see note to Table 10.

$W_{\max}$  is the maximum velocity of the helium flow in the test section,  
 $T_{\text{fl}}^{\max}$  is the maximum temperature of the main fluid flow,  
 $T_s^{\max}$  is the maximum temperature of the volume with samples,  
 $T_w^{\max}$  is the maximum temperature of the capsule wall,  
 $T_h^{\max}$  is the maximum temperature of the electrical heater,  
 $T_{\text{ref}}^{\max}$  is the maximum temperature of the lateral reflector.

Finally, the calculation is done for the model under nuclear and electrical heating (with three sections of the electrical heater under operation) for Case 8a. The temperature distribution in the lateral reflector is shown in Fig. 2.59a. One can see that the maximum temperature of the lateral reflector is increased up to 149.3°C and the zone with the maximum temperature is located near the test section. This zone is heated by the helium flowing in the “narrow” cooling channels of the test section located near the lateral reflector. Nevertheless, the value of the maximum temperature of this zone and the dimension of the zone itself is less than for the initial case, Fig. 2.54. For comparison Fig. 2.59b presents the temperature distribution in the lateral reflector under nuclear and electrical heating and with  $h = 1$  mm. One can see that the maximum temperatures are very close for these two cases. Moreover, the maximum temperature for the case with  $h = 1$  mm is 1.2°C lower than for the case with  $h = 2$  mm. This can be explained by the flow redistribution between the main stream and bypass flow, because the hydraulic resistance of the lateral reflector cooling system is increased for the case with  $h = 1$  mm and the mass flow rate of the main flow is increased, the velocity of the helium flow in the test section is also increased and the flow temperature is decreased. Additionally, one can also see that the temperature distribution in the lateral reflector is more uniform for the case with  $h = 2$  mm, Fig.2.59.

#### *Conclusion to the section.*

The modified cooling system consisting of 4 cooling channels located at 7, 20, 45 and 80 mm from the test section, case 8 or case 8m can be recommended for cooling the lateral reflector. The gap height of the bypass flow supply and removal system can be recommended in the range of 2 - 4 mm.

## **3 Natural convection simulation in the IFMIF test cell cavity**

### **3.1 Testing turbulence models for natural convection simulation**

#### *3.1.1 Introductory remarks*

Natural convection in cavities is encountered in many engineering applications. These include energy transfer in rooms and buildings, nuclear reactor cooling, solar collectors, electronic equipment cooling, etc. All these enclosure flows are dominated by buoyancy and near wall effects. A classical configuration in heat transfer is the rectangular cavity that is differently heated over two opposing vertical walls. Being simple in geometry and boundary conditions, these flows represent a simplified version of practical applications. In spite of the developments in the measurement technology, as well as in numerical methods, fully describing the fluid flow and heat transfer in such a geometry still remains a challenge. As a result, this generic type of physical phenomena is serving as numerical and experimental benchmark tests for the

development and validation of turbulence modelling strategies which can then be applied to buoyancy driven flows in industrial applications.

Natural convection can in some cases demonstrate the flow instabilities especially for cavities with high and low aspect ratio (= height/width ratio), [6, 7]. In these cases the flow has unstable character and one can say only about averaged characteristics of fluid flow and heat transfer. In another cases the flow induced by the natural convection can be practically steady and stable. But even under these steady state conditions of the natural convection flows, a variety of regimes may coexist in a single flow domain in spite of relatively high bulk-Rayleigh numbers, ranging from fully stagnant fluid to laminar circulation, transitional regime, and fully turbulent regions [8]. The natural convection flows are characterised by steep gradients of all properties in usually very thin boundary layer along the non-adiabatic walls, while the core region remains largely stratified and laminar. For numerical simulation this fact requires a fine enough mesh of the near wall region.

A serious problem is that of resolving the large-scale three-dimensional structures, found in well-controlled two-dimensional geometries, as well as local oscillations noticed frequently in basically steady situations [8]. A cavity can have additional solid obstacles inside, around which the natural convection flows can take place. Appropriately capturing the averaged effects of all these structures requires the application of a three-dimensional unsteady computational procedure. A number of turbulence models were developed to simulate more correctly the particular features of the natural convection (see for example, [8-10]). The attempt is undertaken in this work to analyse the ability of the commercial CFD code STAR-CD [4] to simulate the natural convection flow in industrial applications. The STAR-CD code offers a number of turbulence models for the fluid flow simulation. Most of these models are tested and results of the calculation are compared with experimental data.

### ***3.1.2 Model description and simulation***

The experimental benchmark data [11] are chosen for testing the turbulence models offered by STAR-CD. The experimental rig is a cavity 0.75m high x 0.75m wide x 1.5 m deep filled with air and equipped by monitoring and control system. Detailed description of the installation and experimental procedure can be found in [11]. The vertical hot and cold walls of the cavity are isothermal at 50<sup>0</sup>C and 10<sup>0</sup>C respectively giving Rayleigh number of 1.58\*10<sup>9</sup>. Top and bottom walls are made of steel and are insulated. Such horizontal aspect ratio (deep/height = 2) results in 2D flow in the mid-plane of the cavity. So, to simulate these experimental data a 2D model is built with the square cross section of 750 x 750 mm. Top and bottom steel walls of 1.5 mm thick are simulated with adiabatic boundary conditions on the external surfaces. The general view of the model is shown in Fig. 3.1. The mesh of the calculation domain is not uniform: it is more fine near the walls and is more coarse in the central zone, Fig.3.2. The calculations are done with the CFD code STAR-CD [4].

### ***3.1.3 Results of the simulation***

The calculations are carried out using, first of all, the low Reynolds number turbulence models. These are: linear low Re number model (low-Re), quadratic low Re number model (low-ReQ), k-omega low Re number model (k-w low-Re), SST low Re number model (SST low-Re) and the  $\nu_2f$  model is tested too (V2F). Then the high

Re number models are used to simulate the experimental data: linear high Re number model (high-Re), high Re number quadratic and high Re number quadratic with non-equilibrium treatment near the wall region (high-ReQ, high-ReQ neq), k-epsilon Chen model (Chen), SST high Re number model (SST high-Re), k-omega high Re number and k-omega high Re number model with non-equilibrium near the wall treatment (k-w high-Re, k-w high-Re neq).

Typical velocity field and temperature distribution obtained with high Re number and low Re number models are shown in Fig. 3.3, 3.4. One can see that qualitatively the velocity field and the temperature distribution are quite similar, but detailed analysis demonstrates a noticeable difference. For example, the vortexes in the corners obtained with the high Re number turbulence model are smaller than those obtained with the low Re number turbulence models. Accordingly, the temperature distribution in these regions is also different. In this connection it is interesting to compare the calculated results with the experimental data [11], where the mean temperature and velocity distribution are presented in the cavity at its mid-height. The data are also available for the temperature distribution along top and bottom walls as well as the temperature distribution in a vertical plane at the cavity mid-width.

The results of simulation are first of all compared with directly measured data, i.e. with the velocity and temperature distribution. The velocity and temperature distributions near the hot and cold walls are practically anti-symmetrical, so the comparison is done for the distribution of the thermal-hydraulic characteristics near the hot wall.

The velocity distribution in the boundary layer calculated with different turbulence models are compared with the experimental data and shown in Fig. 3.5 - 3.7. Low-Re, low-ReQ and V2F turbulence models give practically identical results, so in Fig. 3.5a-3.7a this is a single line. In general, practically all the turbulence models over-predicted the velocity value in vicinity of the wall (0 – 9 mm) and under-predicted it farther from the wall, except for some high Re number turbulence models (particularly k-w high-Re). The velocity profile predicted by the low Re number turbulence models is close to the laminar one. One can see that some of the high Re number turbulence models give better agreement with the experimental data, but this fact can not be considered as an argument that these models simulate the natural convection better. The matter is the following. It is known that the high Re number turbulence models work correctly for the mesh where the  $y^+$  of the first cell from the wall is equal to  $\sim 30$ , at least  $y^+$  should be more than 12. The velocity in the model simulated varies from 0 in stagnation zones to about 1.3 m/s near the vertical walls. So, the  $y^+$  value varies significantly also. Additionally, to catch the behaviour of the velocity and temperature in the boundary layer correctly, the region of this layer is meshed more fine. Under these circumstances, the  $y^+$  in the model reaches the value of 2 and even less in some places.

The temperature distribution presented in Fig. 3.8, 3.9 shows that practically all the models describe the temperature profile at the cavity mid-height satisfactorily. At the same time, the temperature distribution in the vertical plane at the cavity mid-width is under-predicted by all the turbulence models, Fig. 3.10. Temperature distribution along the top wall shown in Fig. 3.11 demonstrates that calculated results are over-predicted to the experimental data by both high Re number and low Re number turbulence models. It should be also noted, that all the low Re number turbulence

models predict very low value of the turbulent kinetic energy, three order of magnitude lower than the experimental values, i.e. they give practically laminar flow in the cavity. The high Re number turbulence models predict turbulent character of the flow in the cavity and give the same order of magnitude of its value, Fig. 3.12a. On the other hand, the high Re number turbulence models give typical distribution of the turbulent kinetic energy in near the wall region, which differs from the experimental data, Fig. 3.12b.

As a conclusion, one can say that the low Re number turbulence models give velocity profile in near the wall region close to the laminar one, i.e. over-predict the experimental data. The use of the high Re number turbulence models with a strong restriction on  $y^+$  ( $y^+ \geq 30$ ) can result in the fact that it is difficult to describe correctly the narrow boundary layer zone (at a low velocity of the fluid flow, which is typical for the natural convection). In this connection it should be mentioned that k-omega high Re number turbulence models are more “flexible”, because they are applied up to  $y^+ = 5$ . Moreover, at industrial applications for cases, where the natural convection plays a significant role and a cavity has several differently heated elements, the flow can be considered as combined natural-and-forced convection flow. The low Re number turbulence models require very fine mesh of the near wall region and also require much computing time and resources. In this case the use of the high Re number turbulence models (particularly, k-omega) for the flow simulation can be reasonable.

#### *Conclusion to the section.*

An experimental benchmark is chosen for testing the turbulence models offered by the STAR-CD code. The experimental rig is a cavity 0.75 m high x 0.75 m wide x 1.5 m deep filled with air and equipped by monitoring and control system. The vertical hot and cold walls of the cavity are isothermal at 50<sup>0</sup>C and 10<sup>0</sup>C respectively giving Rayleigh number of  $1.58 \cdot 10^9$ . Top and bottom walls are made of steel and are insulated. Such horizontal aspect ratio (deep/height = 2) results in 2D flow in the mid-plane of the cavity. So, to simulate these experimental data a 2D model is built with the square cross section of 750 x 750 mm. Top and bottom steel walls of 1.5 mm thick simulated with adiabatic boundary conditions on the external surfaces.

The main turbulence models offered by the STAR-CD code are tested on these experimental data. As a conclusion one can say that the low Re number turbulence models give velocity profile in near the wall region close to the laminar one, i.e. over-predict the experimental data. The use of the high Re number turbulence models with a strong restriction on  $y^+$  ( $y^+ \geq 30$ ) can result in the fact that it is difficult to describe correctly the narrow boundary layer zone (at a low velocity of the fluid, which is typical for the natural convection). In this connection it should be mentioned that k-omega high Re number turbulence models are more “flexible”, because they are applied up to  $y^+ = 5$ . Moreover, at industrial applications for cases where natural convection plays a significant role and a cavity has several differently heated elements, the flow can be considered as combined natural-and-forced convection flow. The low Re number turbulence models require very fine mesh of the near the wall region and also require much computing time and resources. In this case the use of the high Re number turbulence models (particularly, k-omega) for the flow simulation can be reasonable.

### 3.2 Simulation of the natural convection flow in the IFMIF test cell cavity

The IFMIF test cell cavity includes a number of elements. These are a lithium target, lithium loop components, IFMIF test modules, and auxiliary systems. The operation conditions of the test cell equipment result in a significant heating of some elements. For example, the target and lithium loop components are heated up to 250<sup>0</sup>C – 300<sup>0</sup>C, the test modules can have the temperature of 100<sup>0</sup>C or higher. At the same time, the surrounding building structures should be kept at the temperatures acceptable for a concrete. The test cell cavity can be evacuated and under these conditions the main mechanism of the heat transfer is radiation. An alternative is filling the cavity with a gas. In this case the heat transfer mechanism is the natural convection and radiation.

The aim of this simulation is estimation of the natural convection heat transfer in the cavity if it is filled with gas. The simplified representation of the IFMIF test cell is adopted at the first stage of the simulation. Only lithium loop components (as the most heated elements of the cavity internals) are simulated and the target is simulated as a tube section with the temperature of 300<sup>0</sup>C. The general isometric view of the model is shown in Fig. 3.13. The geometrical dimensions of the model simulated are based on the information taken from [12,13] and are presented in Fig. 3.14, 3.16-3.19. The IFMIF test modules are not simulated.

The thermohydraulic simulation is done with the STAR-CD code [4]. Preliminary testing of the turbulence models offered by the code showed that the k-omega high Reynolds number turbulence model can be applied for the natural convection simulation in the IFMIF test cell cavity. The mesh of the calculation domain is non-uniform. It is more fine in the near the wall region of all the elements simulated and is more coarse in the remaining part of the model (an example of the mesh is shown in Fig. 3.15). Helium and argon at the atmospheric pressure are considered as the gas filling the test cell cavity. The gas density is a function of the temperature. The helium thermal conductivity is approximated with the following relationship

$$\lambda_{\text{He}} = 0.056 + 0.00031 * T, \text{ W/(m*K)}.$$

The argon thermal conductivity is constant.

The boundary conditions are rather complicated for this task. The temperature of the external surfaces of the volume of the test modules is not known exactly. Moreover, this volume can have a shield which can be heated by the nuclear heating and can be considered as a volumetric heat source. At the moment the nuclear calculations of this element are in progress and the heat source distribution is not taken into account. For this reason, the boundary conditions are adopted in a simplified form: the external surfaces of the model have the temperature of 50<sup>0</sup>C, the lithium loop elements have the temperature of 250<sup>0</sup>C and 300<sup>0</sup>C, as shown in Fig. 3.16. Under these conditions the Rayleigh number based on the lithium tank height (H~2.7 m) and the temperature difference of 250 grad is  $Ra \cong 1.29*10^9 - 2*10^{10}$ . It is known that under this value of Rayleigh number the natural convection flow is unstable by nature. In this case a converged steady-state solution cannot be obtained. For this reason, the transient approach is used for the task under consideration. The time step for the calculation is estimated as  $\Delta\tau \cong 0.25$  s [4]. The first results are presented in Fig. 3.20- 3.38. These results are presented for the time of  $\tau = 287.5$  s for helium in the cavity, and for the

time of  $\tau = 650$  s for argon in the cavity. The analysis of the results shows that the temperature and velocity distribution slightly oscillates with time about some more-or-less stable quantities. So, these results can be considered as the first iteration for the estimation of the heat transfer with the natural convection in the IFMIF test cell cavity. The general view of the temperature and velocity distribution in the model is shown in Fig. 3.20, 3.21. The temperature and velocity distributions are also shown for several cross sections of the model simulated. These are the cross sections located near the front and back walls (the front wall of the model is indicated in Fig. 3.14, while the one opposite to it is the back wall), Fig. 3.22, 3.23, 3.32, 3.33; the cross section located at 700 mm from the front wall of the model (this section is located near the lithium tank wall), Fig. 3.24, 3.25, as well as the cross sections passing through the lithium loop elements simulated, Fig. 3.26-3.31, 3.34, 3.35.

One can see that the flow patterns and temperature distribution are very complicated and extremely non-uniform, see for example Fig. 3.38. What is more important for our case is that the temperature distribution has a hot spot at the top wall of the model. This hot spot was to be expected because the lithium loop pipe passes near this wall and the gas has the maximum temperature here. This temperature is about  $90^{\circ}\text{C}$  for the helium inside the cavity and about  $144^{\circ}\text{C}$  for the argon, Fig. 3.36, 3.37, but it can be higher when the boundary conditions are known more exactly at the top wall (at the moment the boundary condition is  $T = 50^{\circ}\text{C}$  at all the walls).

One can also see that the flow velocity is higher and the temperature near the wall is lower for the helium. This result can be explained by the fact that helium has higher thermal conductivity than other gases. So, the heat removed by helium from the heated surfaces is larger than the heat removed by argon. On the other hand, helium is rather expensive, has a very high penetration ability and the leakage of helium out of the test cell can be significant. In this connection argon is an appropriate substance to fill the test cell cavity.

## **4 Acknowledgement**

This work has been performed in the framework of the nuclear programme of the Forschungszentrum Karlsruhe and is supported by the European Union within the European Fusion Technology Programme. Special thanks are due to colleagues from IRS for the help and fruitful discussion of the IFMIF/HFTM design.

## 5 References

1. S. Gordeev, V. Heinzl, K.H. Lang, A. Moeslang, K. Schleisiek, V. Slobodtchouk, E. Schratmanns. Optimised Design and Thermal-hydraulic Analysis of the IFMIF/HFTM Test Section. Forschungszentrum Karlsruhe, Wissenschaftliche Berichte FZKA 6895, October 2003.
2. Simakov S.P., Fischer U., Heinzl V., Moelendorf U. Von. International Fusion Material Irradiation Facility (IFMIF): Neutron Source Term Simulation and Neutronics Analyses of the High Flux Test Module. Forschungszentrum karlsruhe, Wissenschaftliche Berichte, FZKA-6743, Juli 2002.
3. STAR-CD Version 3.15. User Guide, Computational Dynamics Limited (2001).
4. STAR-CD Version 3.20. User Guide, Computational Dynamics Limited (2004).
5. IFMIF Comprehensive Design Report. IFMIF International Team. January, 2004. [http://insdell.tokai.jaeri.go.jp/IFMIFHOME/if\\_download\\_site.html](http://insdell.tokai.jaeri.go.jp/IFMIFHOME/if_download_site.html)
6. R.J.A. Janssen, R. A. W. M. Henkes, Instabilities in three-dimensional differentially-heated cavities with adiabatic horizontal walls, *Phys. Fluids* (1996), 62-74.
7. B. Lartigue, S. Lorente, B. Bourret, Multicellular natural convection in a high aspect ratio cavity: experimental and numerical results, *Int. J. Heat Mass Transfer*, 43 (2000), 3157-3170.
8. H.S. Dol, K. Hanjalic, and S. Kenjeris, A comparative assessment of the second-moment differential and algebraic models in turbulent natural convection, *Int. J. Heat and Fluid Flow*, 18 (1997), 4-14.
9. R. A. W. M. Henkes and C.J. Hoogendoorn, Comparison of turbulence models for the natural convection boundary layer along a heated vertical plate, *Int. J. Heat Mass Transfer*, 32 (1989), 157-169.
10. F. Liu, J.X. Wen, Development and validation of an advanced turbulence model for buoyancy driven flows in enclosures, *Int. J. Heat Mass Transfer*, 42 (1999), 3967-3981.
11. F. Ampofo, T.G. Karayannis, Experimental benchmark data for turbulent natural convection in an air filled square cavity, *Int. J. Heat Mass Transfer*, 46 (2003), 3551-3572.
12. M. Martone, IFMIF International Fusion Materials Irradiation Facility – Final Report- IFMIF CDA Team; RT/ERG/FUS/96/11, Dec. 1996.
13. K.-H. Lang, E. Stratmanns, Personal information.

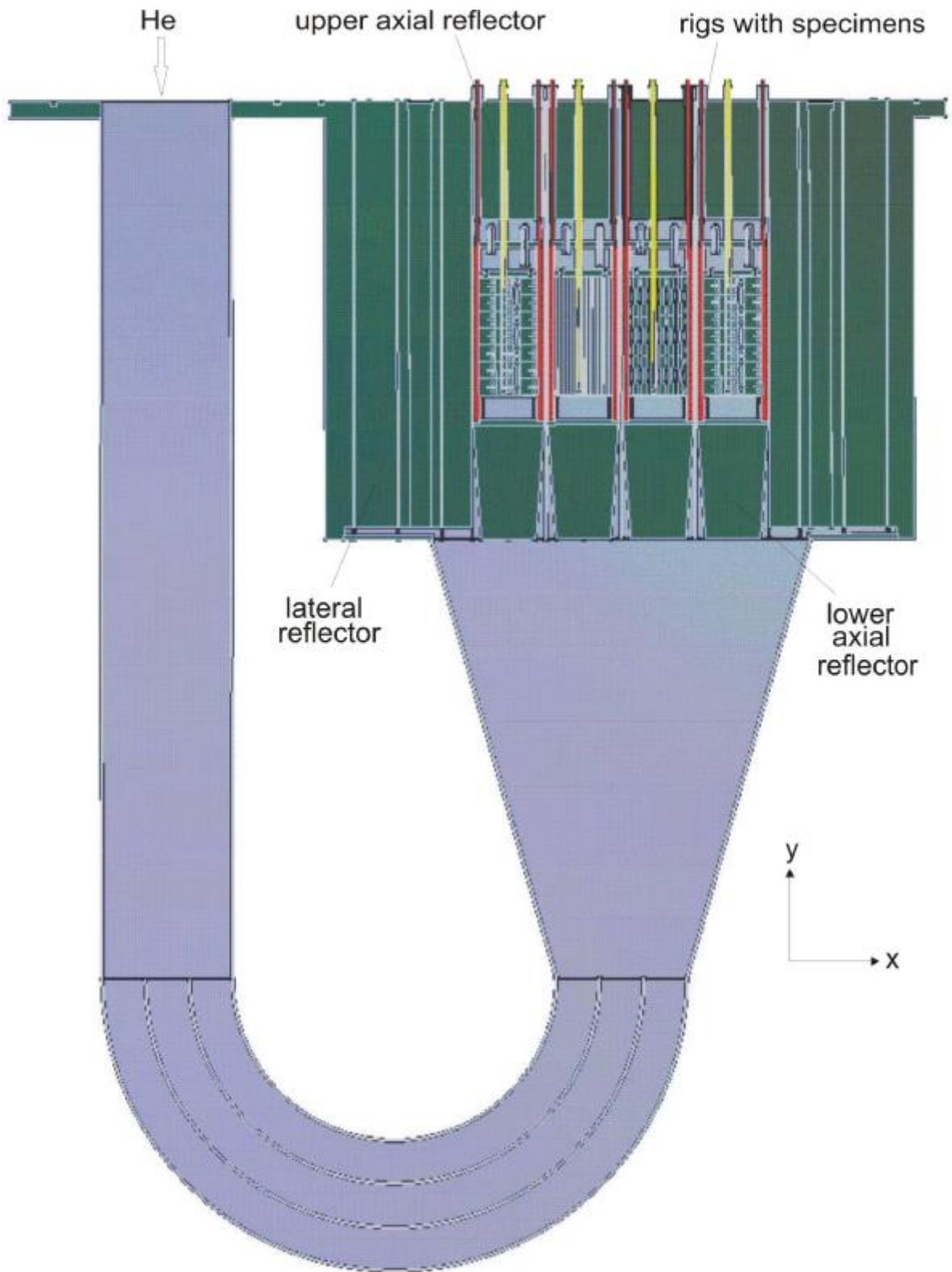


Fig. 2.1 IFMIF Helium cooled High Flux Test Module (HFTM)

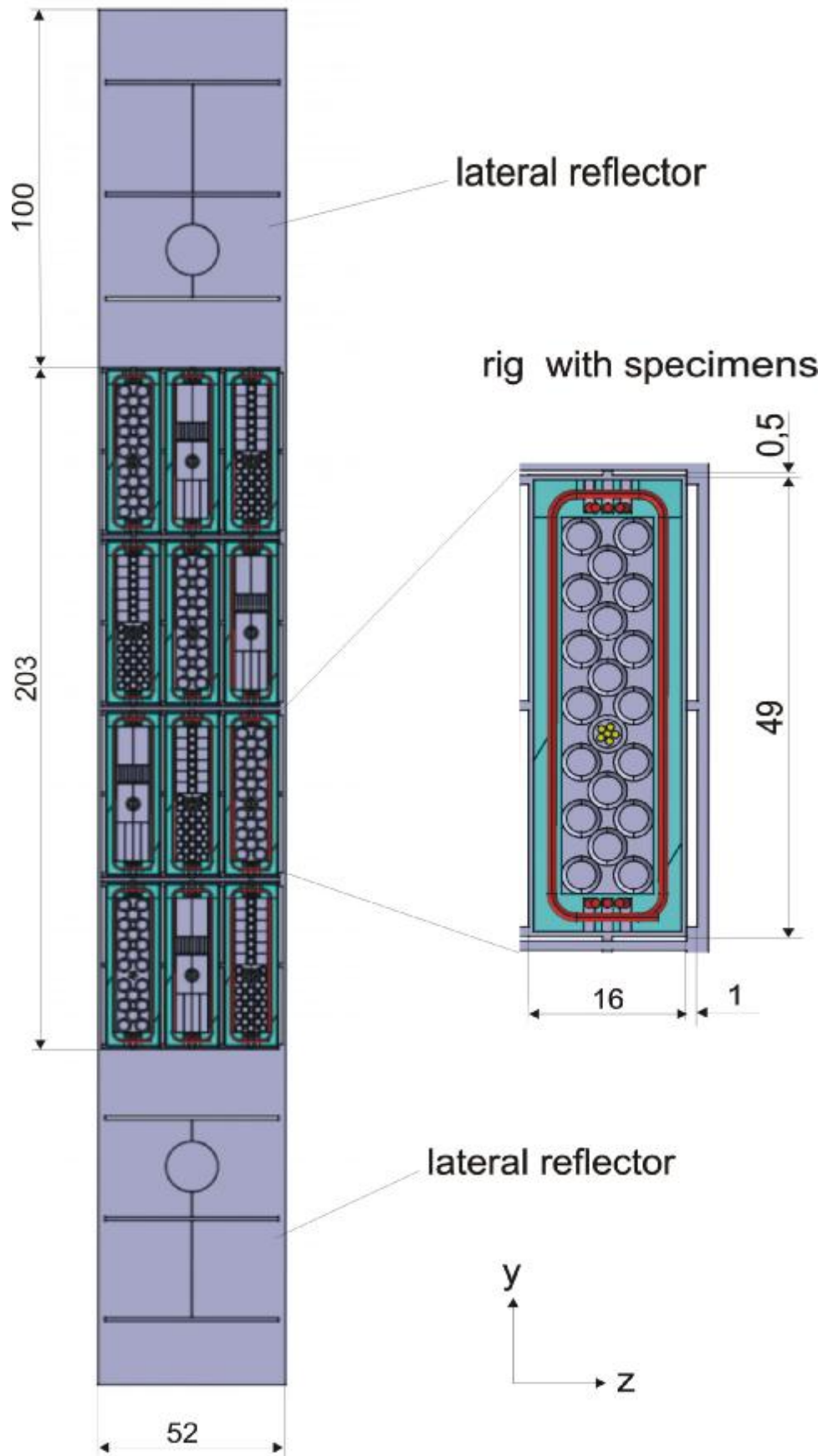


Fig. 2.2 High Flux Test Module cross section

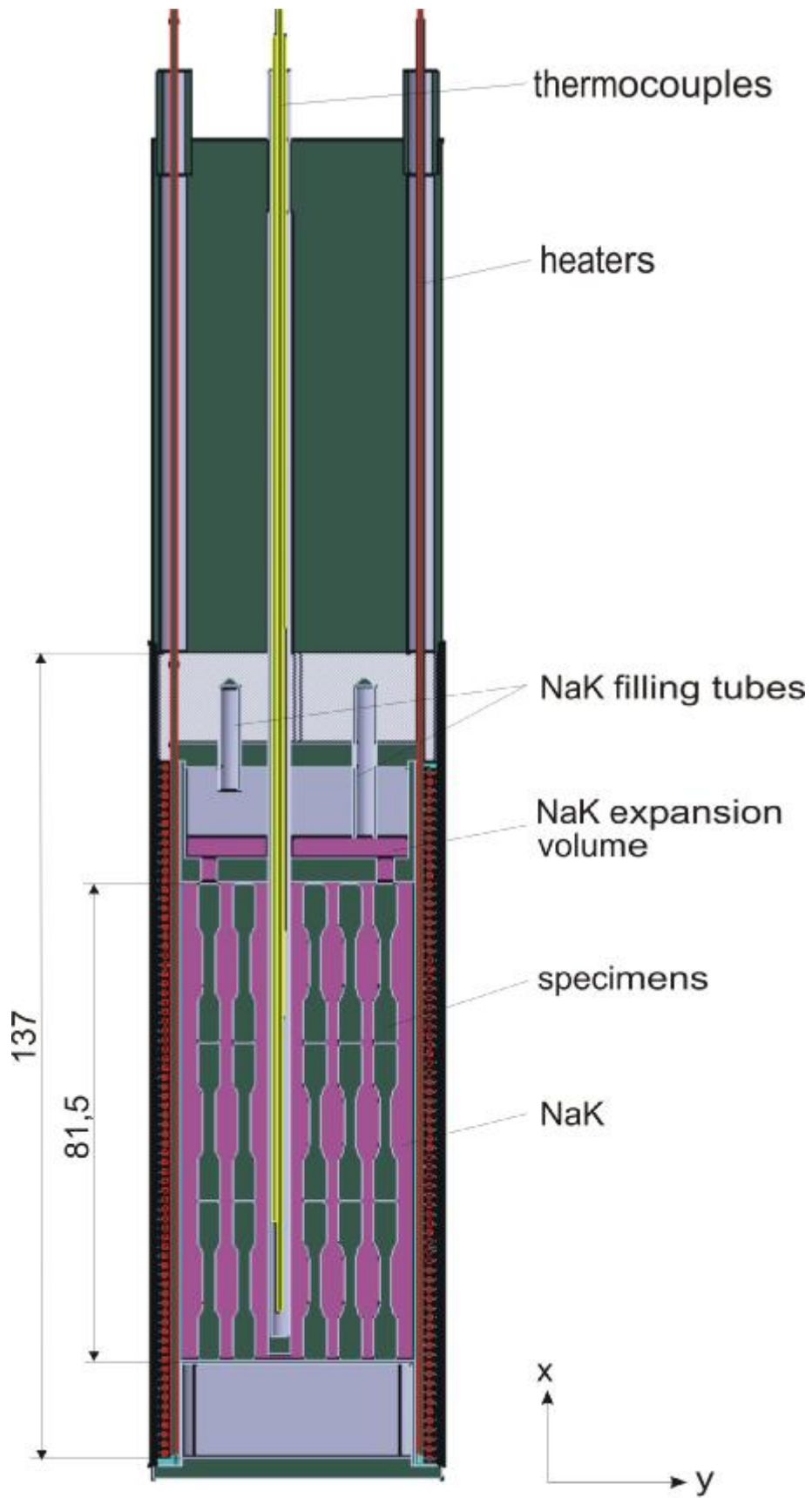


Fig. 2.3 Test rig with specimens

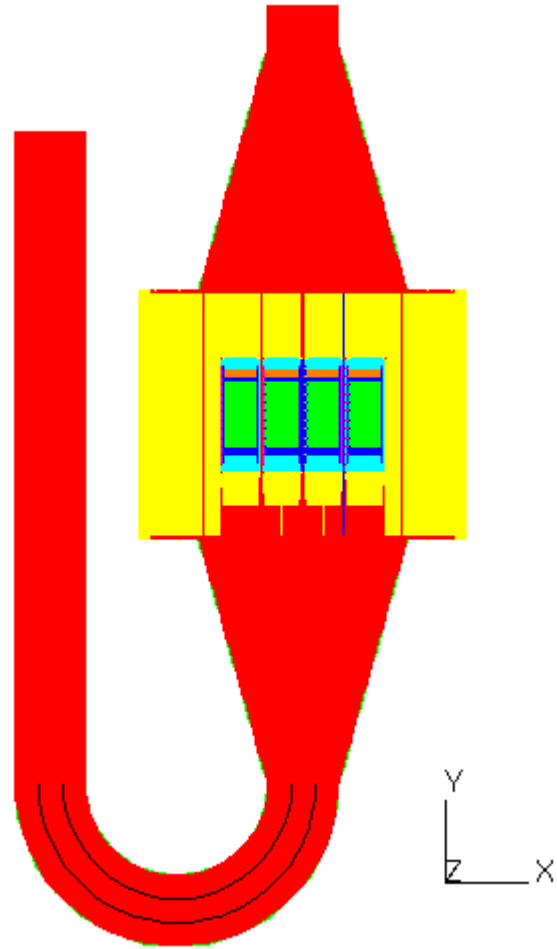


Fig. 2.4 General view of the model simulated

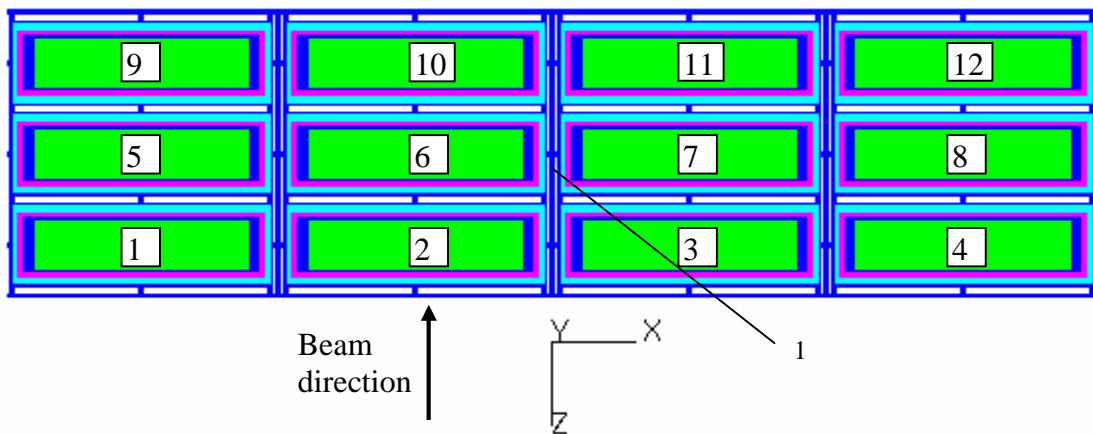


Fig. 2.5 Horizontal cross section of the HFTM test section, 1 – stiffening plate

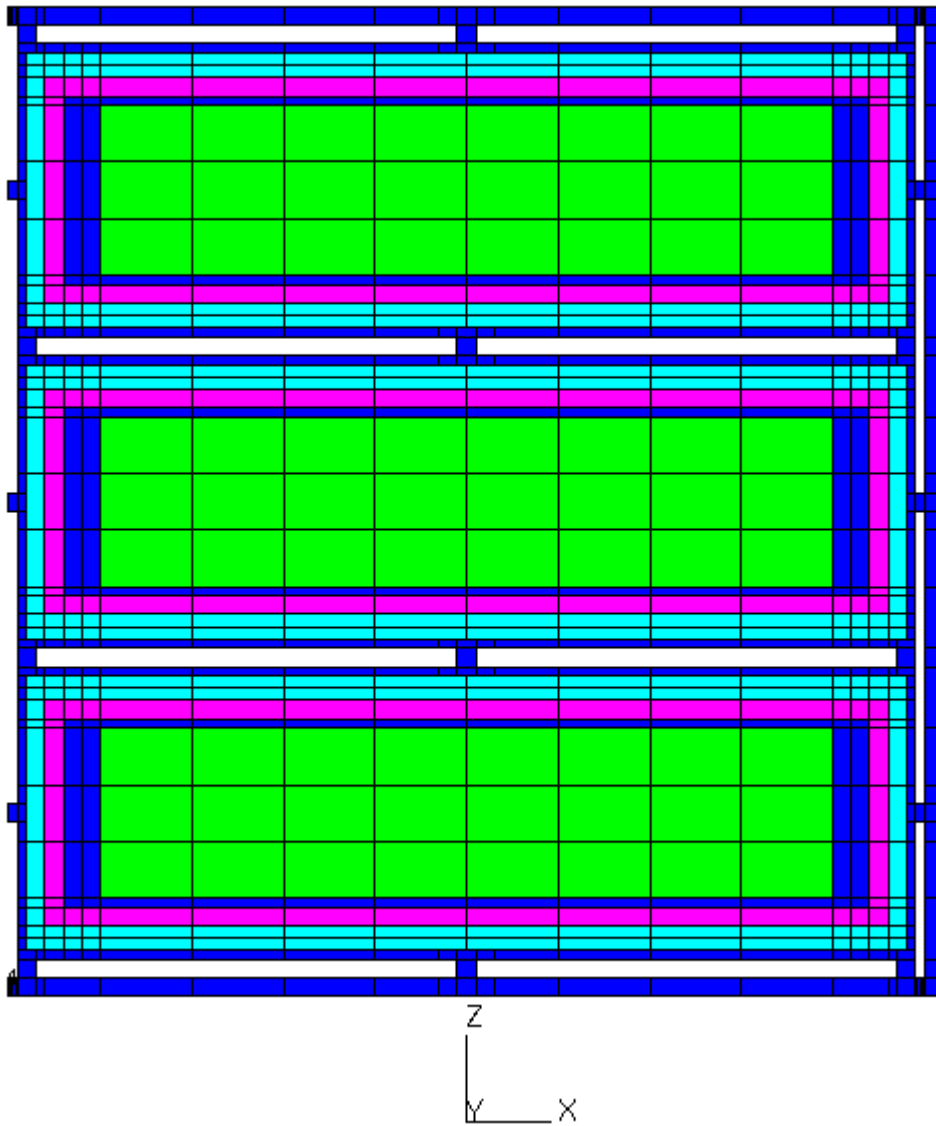


Fig. 2.6 Horizontal cross section of one compartment with three rigs.

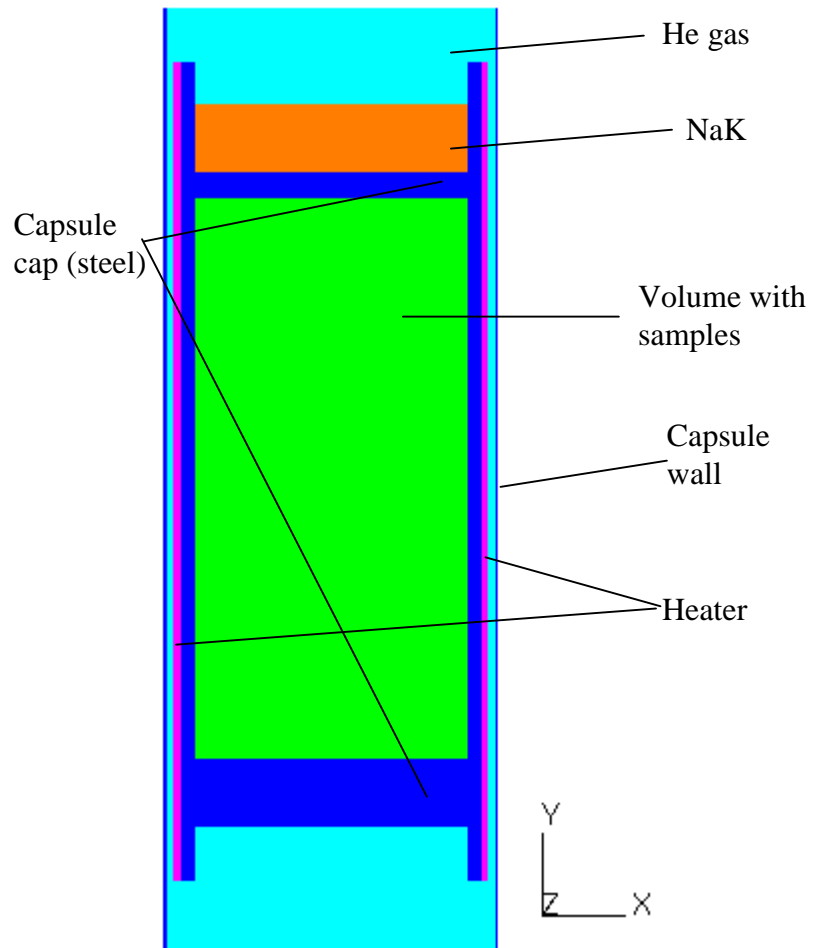


Fig. 2.7 Rig vertical cross section

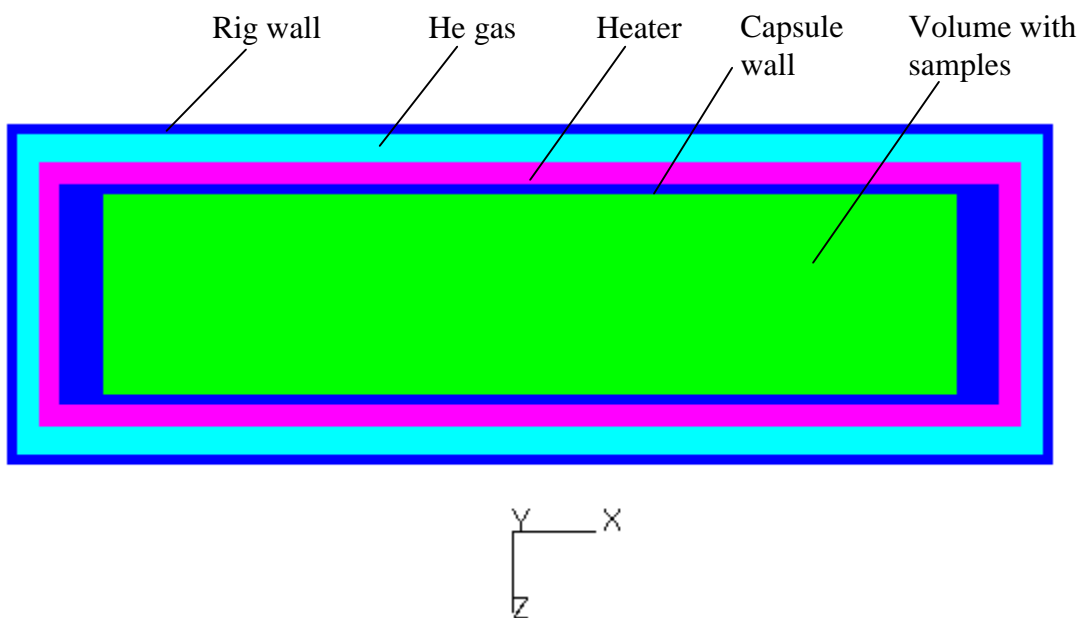


Fig. 2.8 Rig horizontal cross section

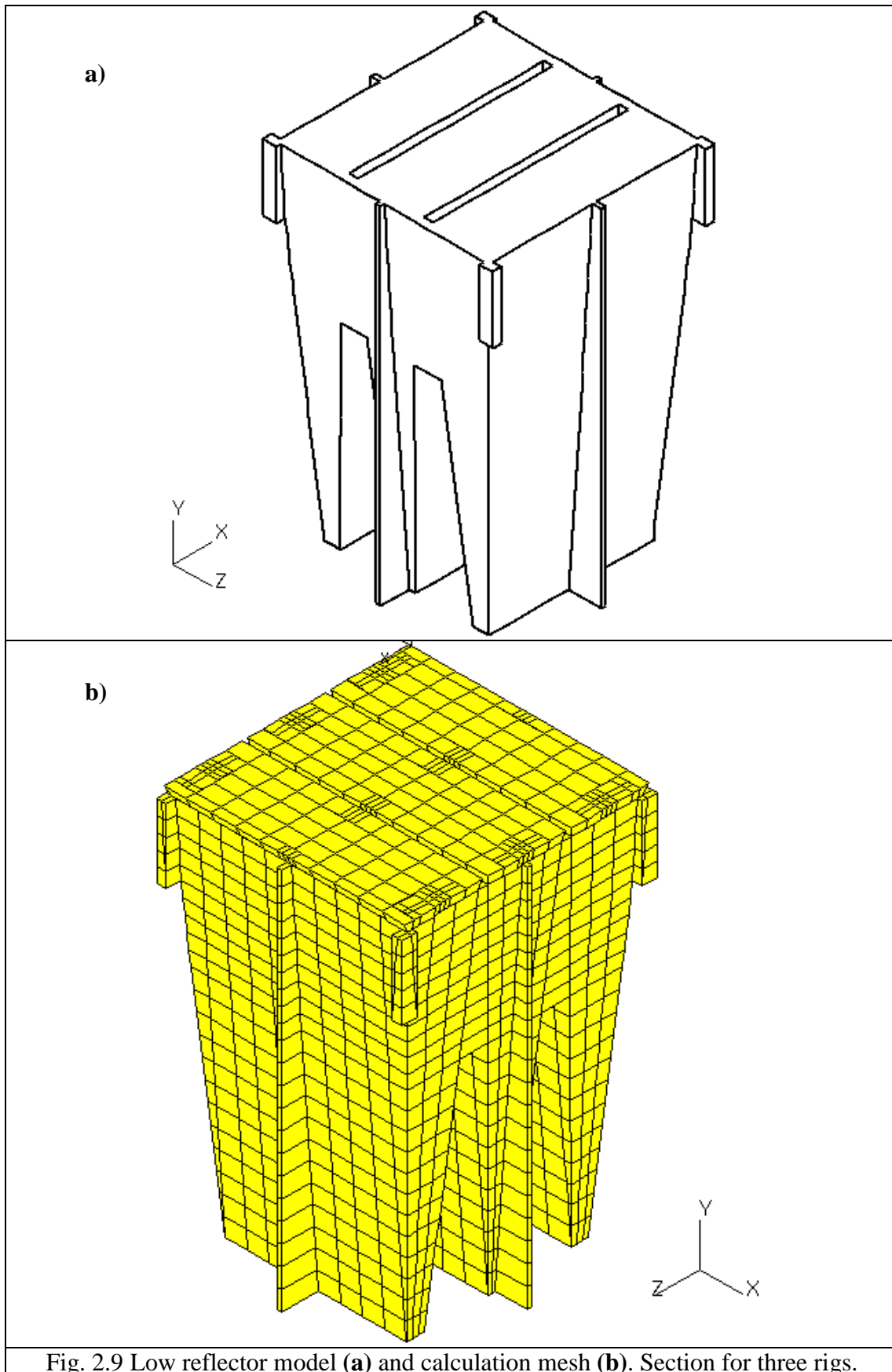


Fig. 2.9 Low reflector model (a) and calculation mesh (b). Section for three rigs.

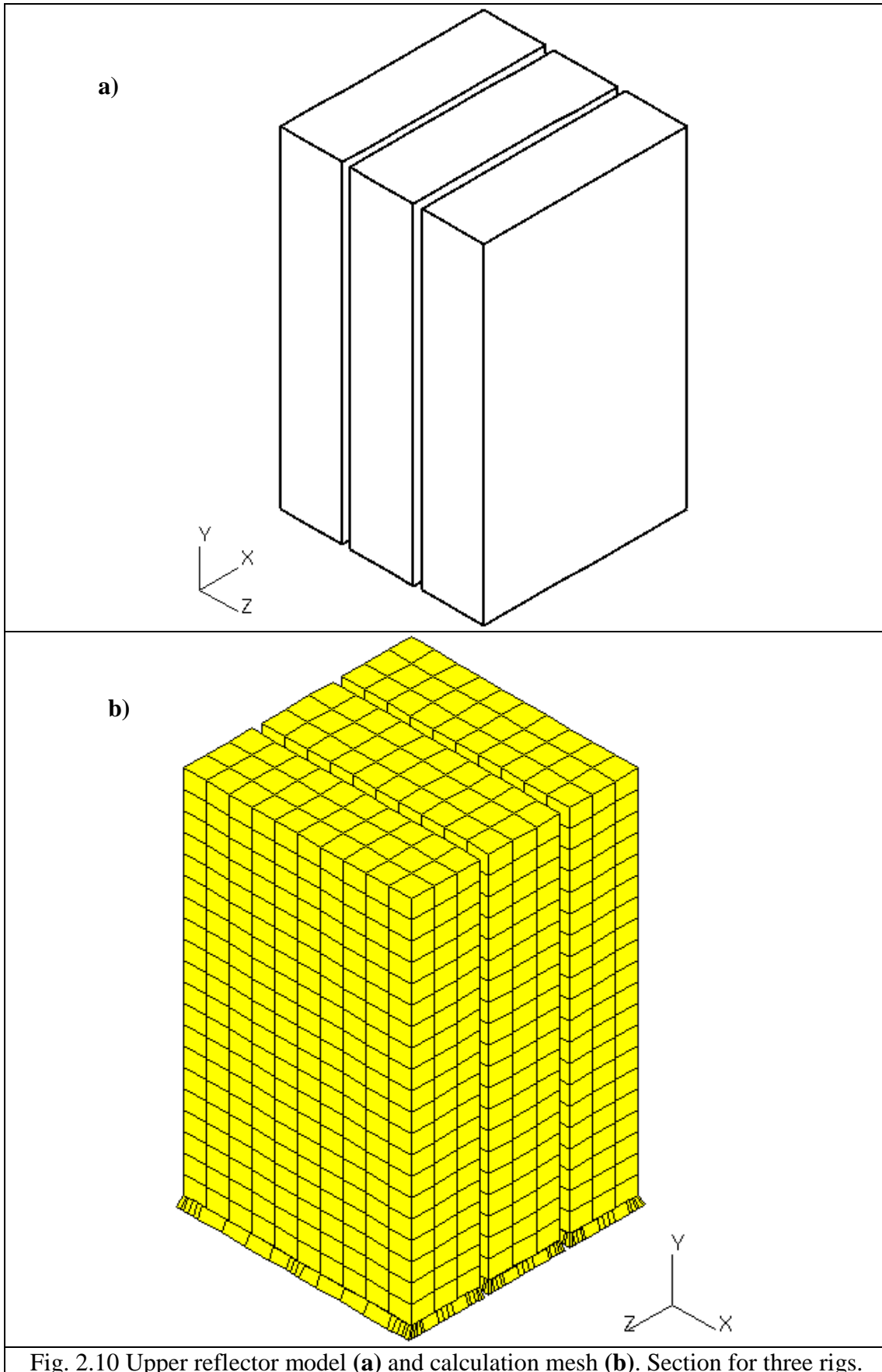


Fig. 2.10 Upper reflector model (a) and calculation mesh (b). Section for three rigs.

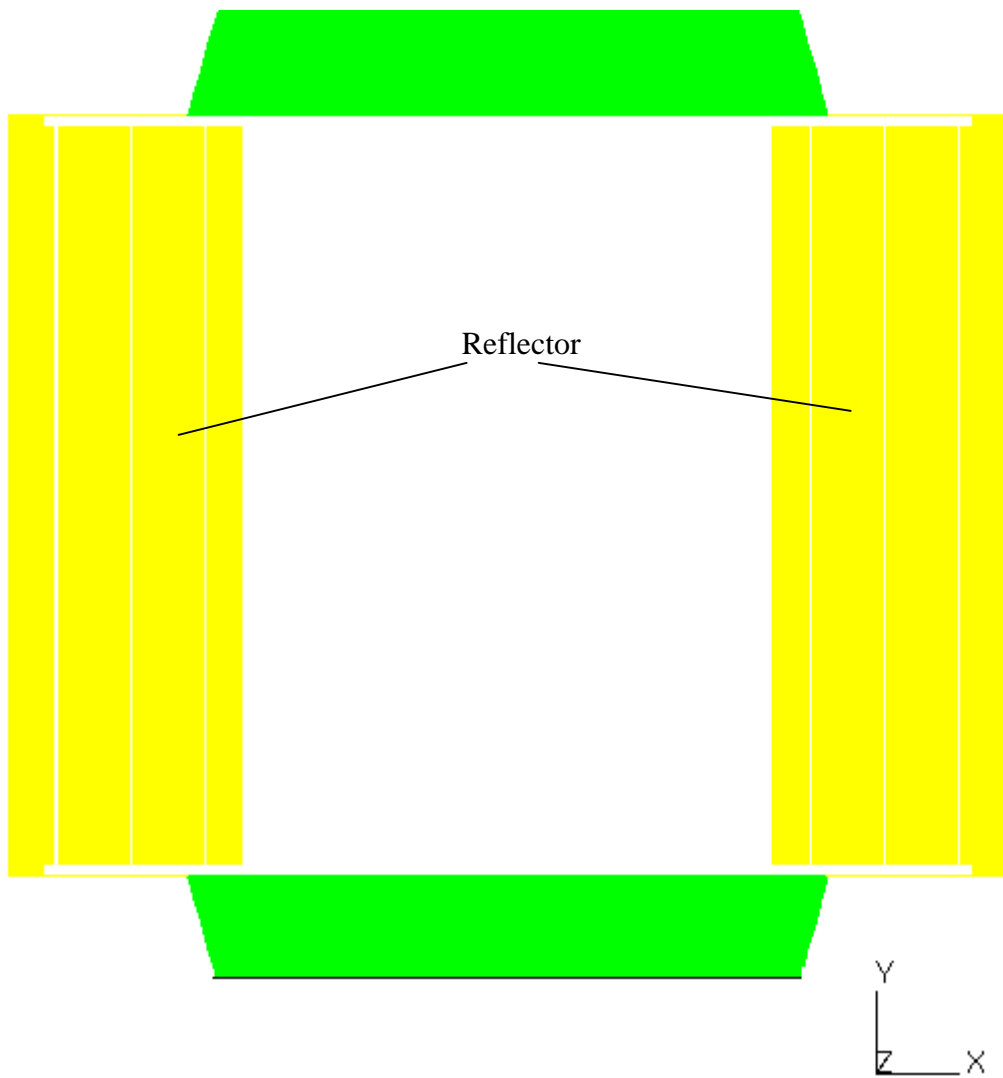


Fig. 2.11 Lateral reflector: general view

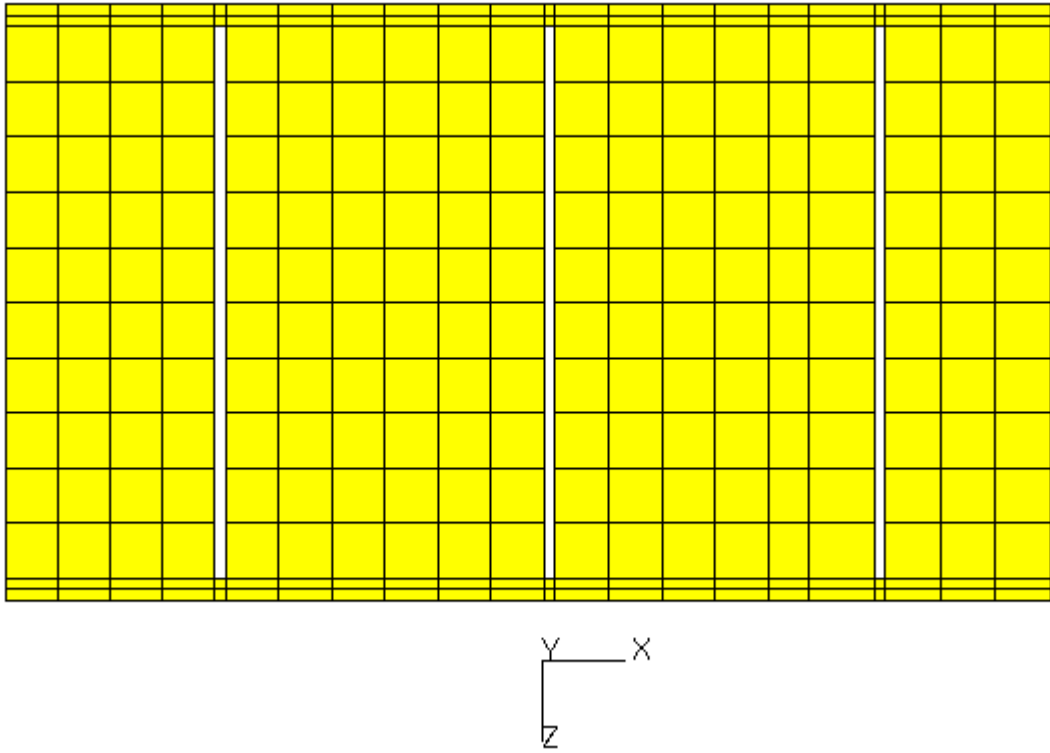


Fig. 2.12 Lateral reflector: mesh and one of the variants of the cooling channels

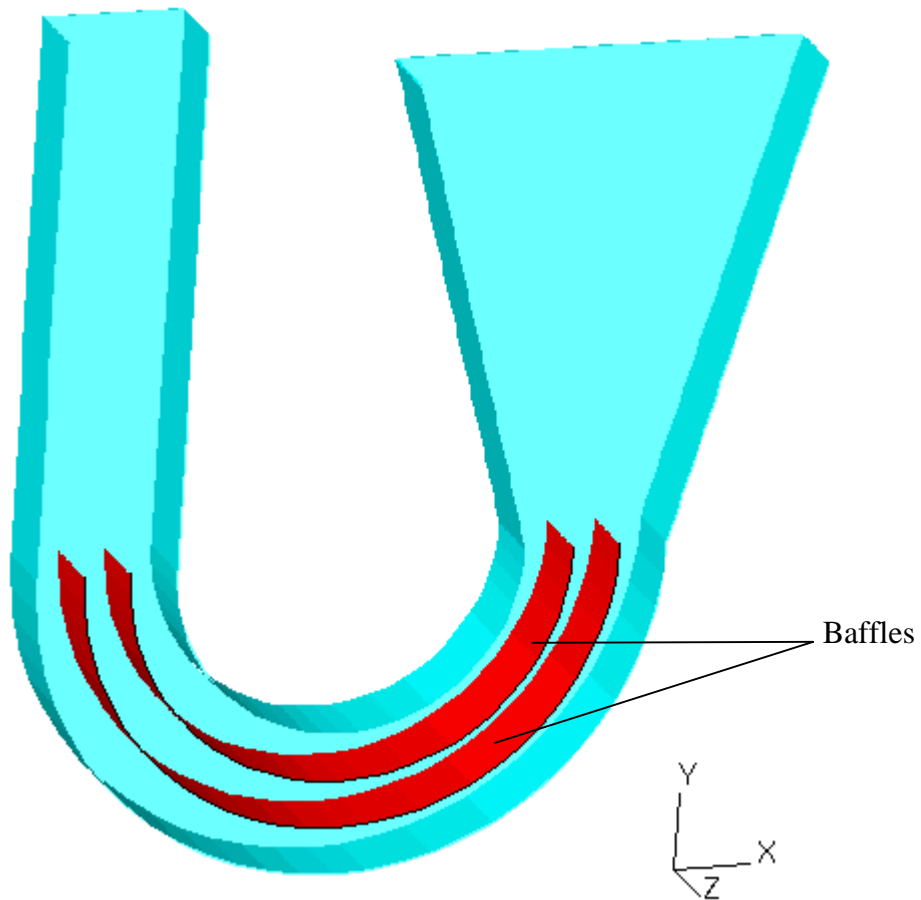
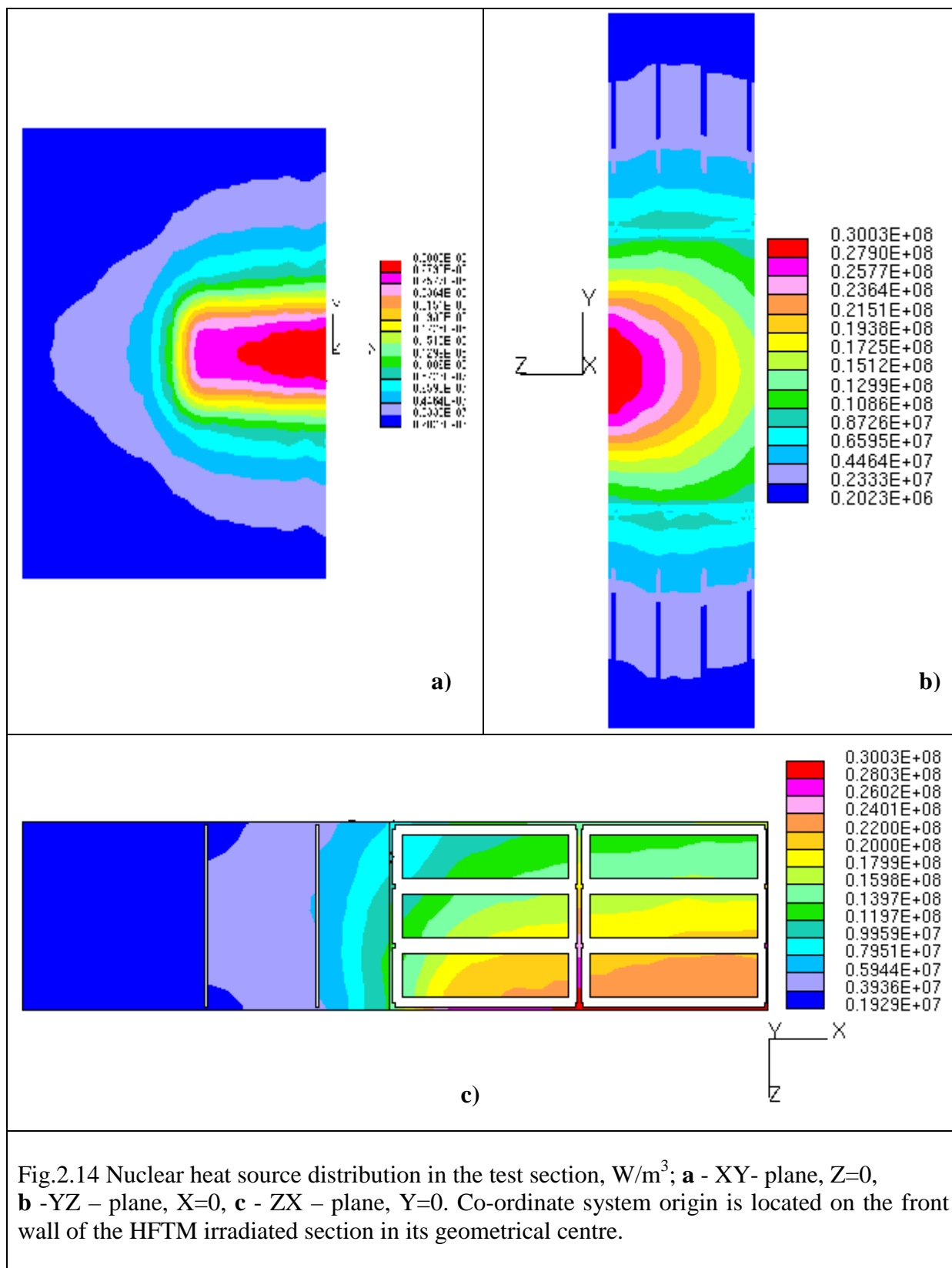
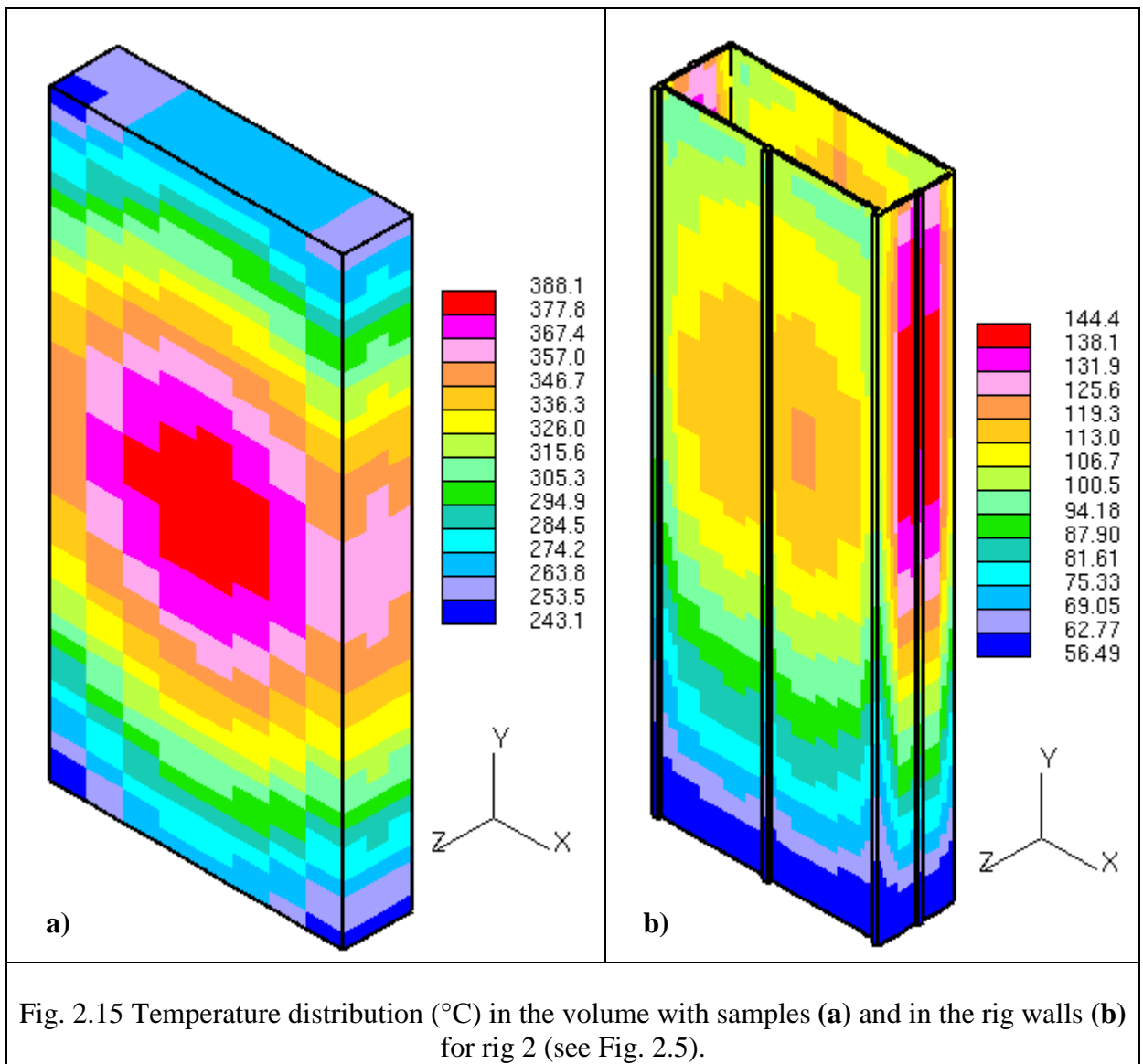


Fig. 2.13 Baffles in the gas supply section of the model.





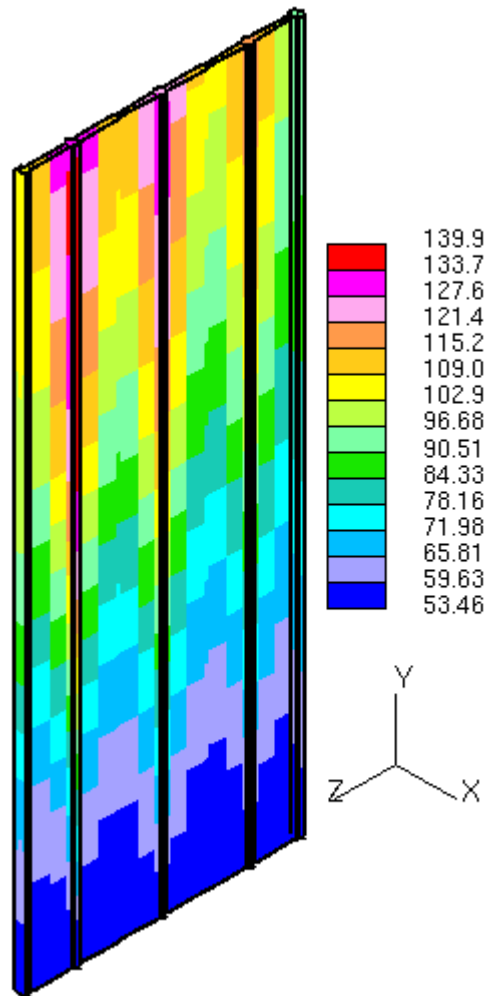
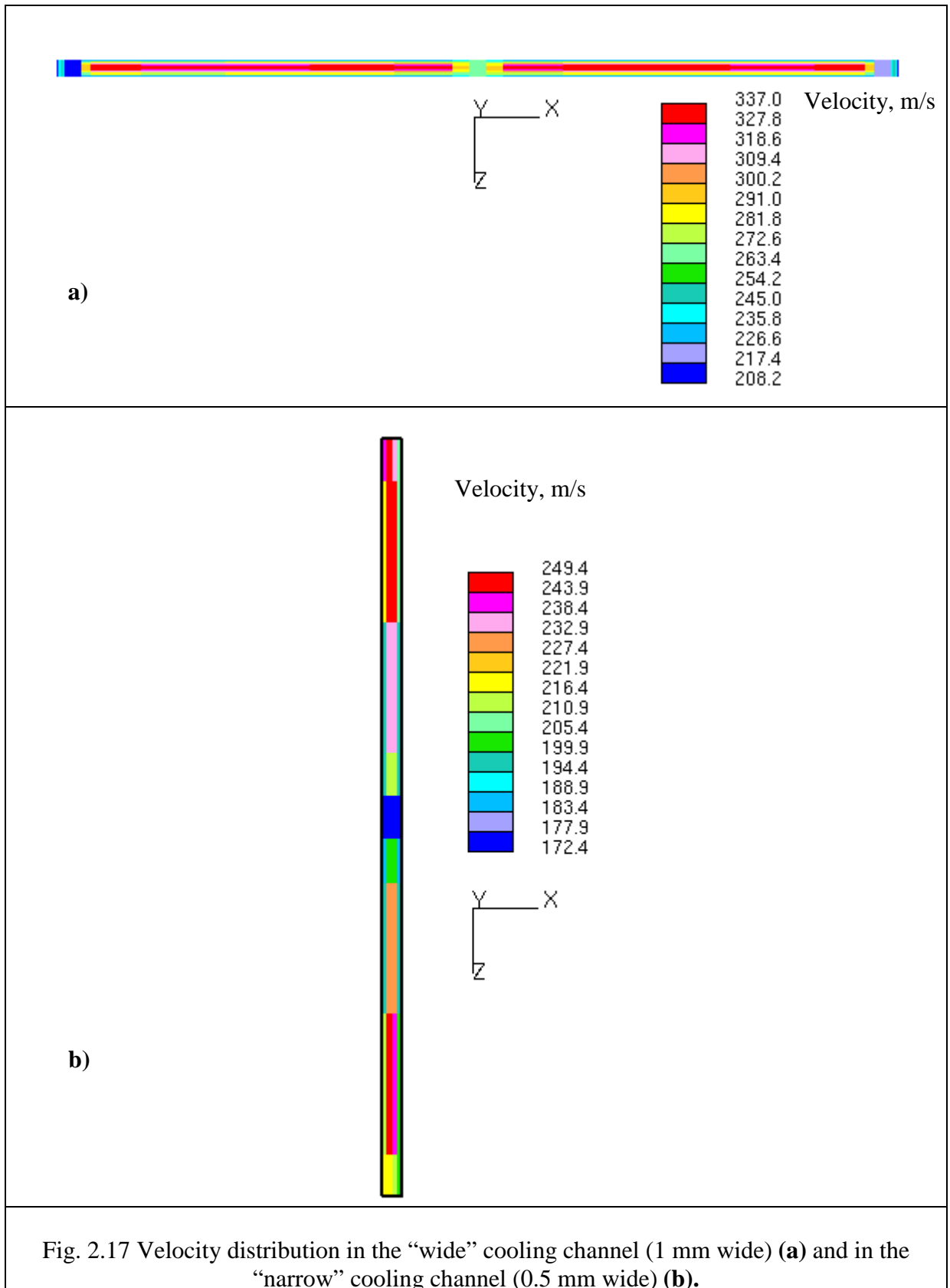


Fig. 2.16 Temperature distribution ( $^{\circ}\text{C}$ ) in the stiffening wall dividing the test section into compartments



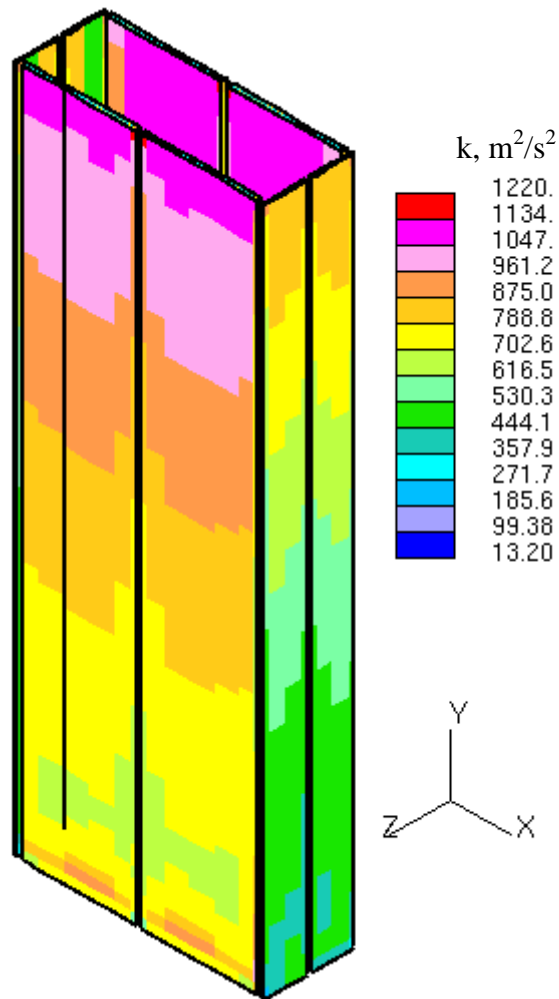


Fig. 2.18 Turbulent kinetic energy distribution in the cooling channels.

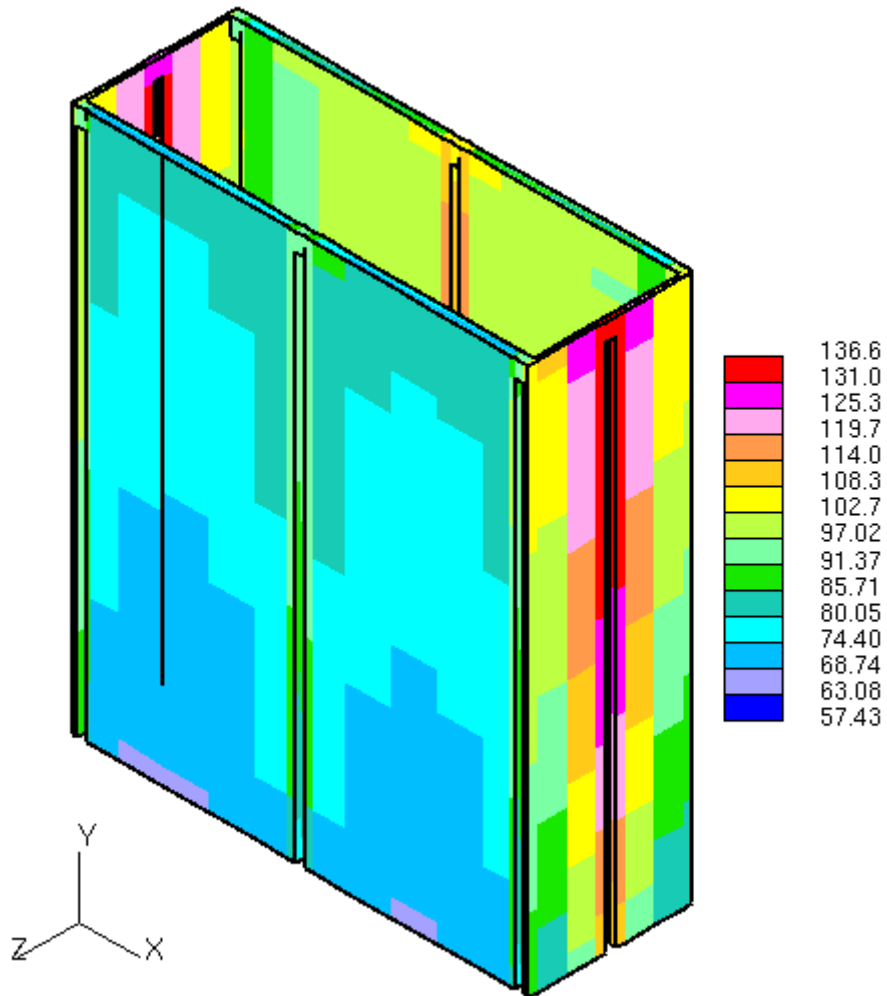


Fig. 2.19 Helium temperature distribution in the cooling channels around the rig 2 (see Fig.2.5)

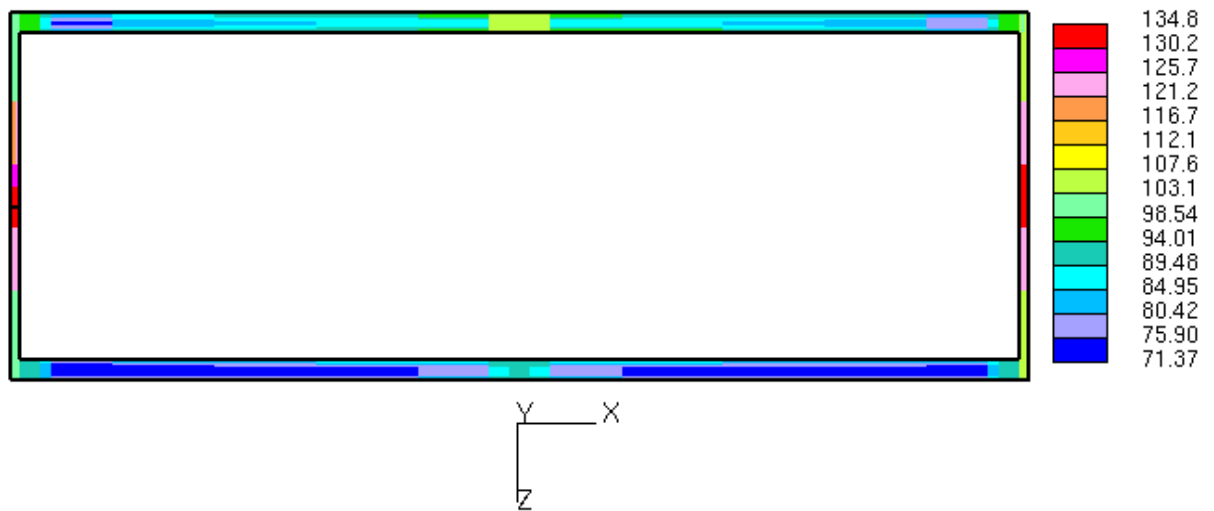


Fig.2.20 Temperature distribution (°C) in the helium flow at the outlet of the cooling channels of the rig 2 (see Fig.2.5)

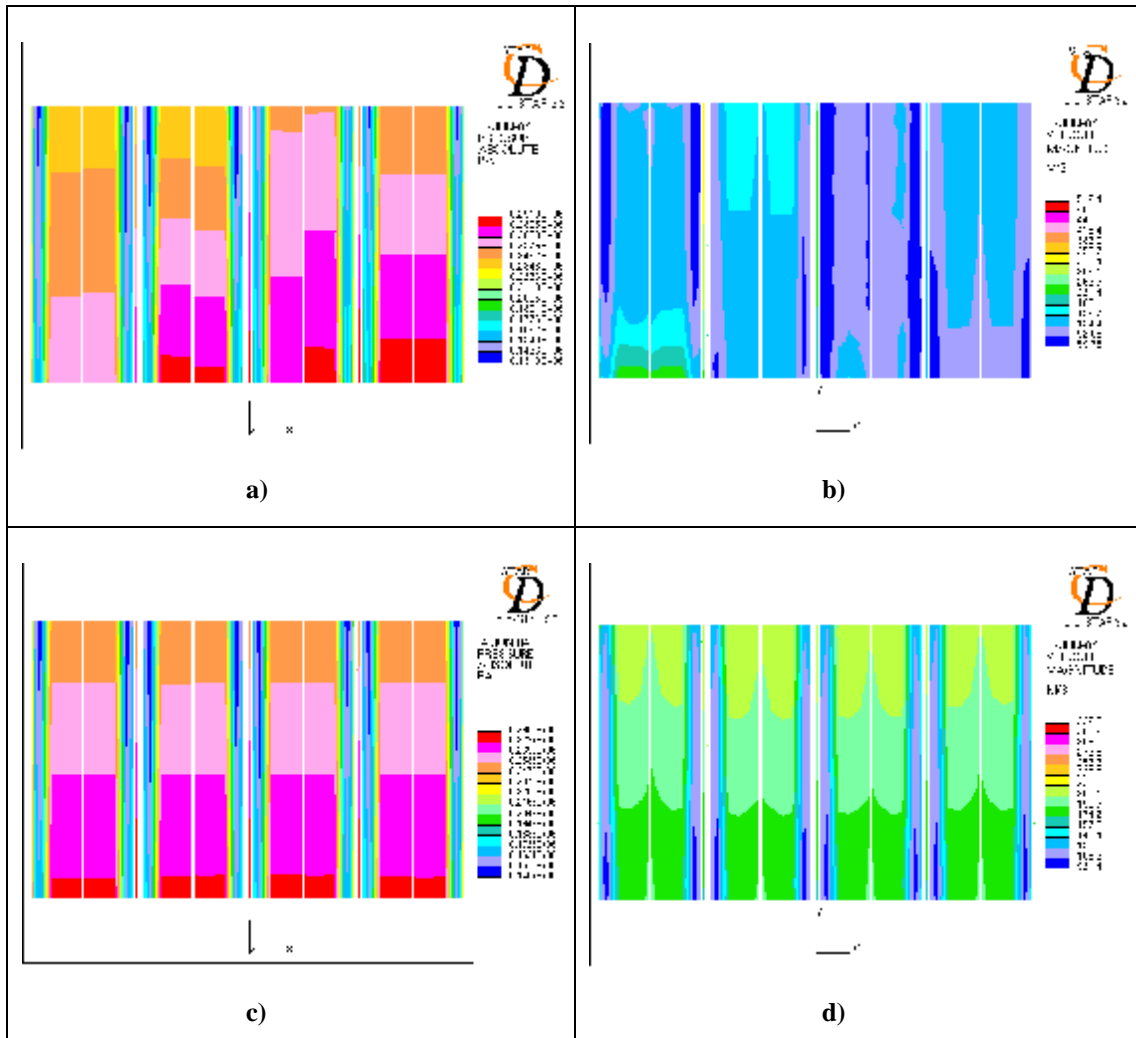


Fig. 2.21 Pressure and velocity distribution in the test section: **a, b** – V2F turbulence model, **c, d** – Chen k-e turbulence model.

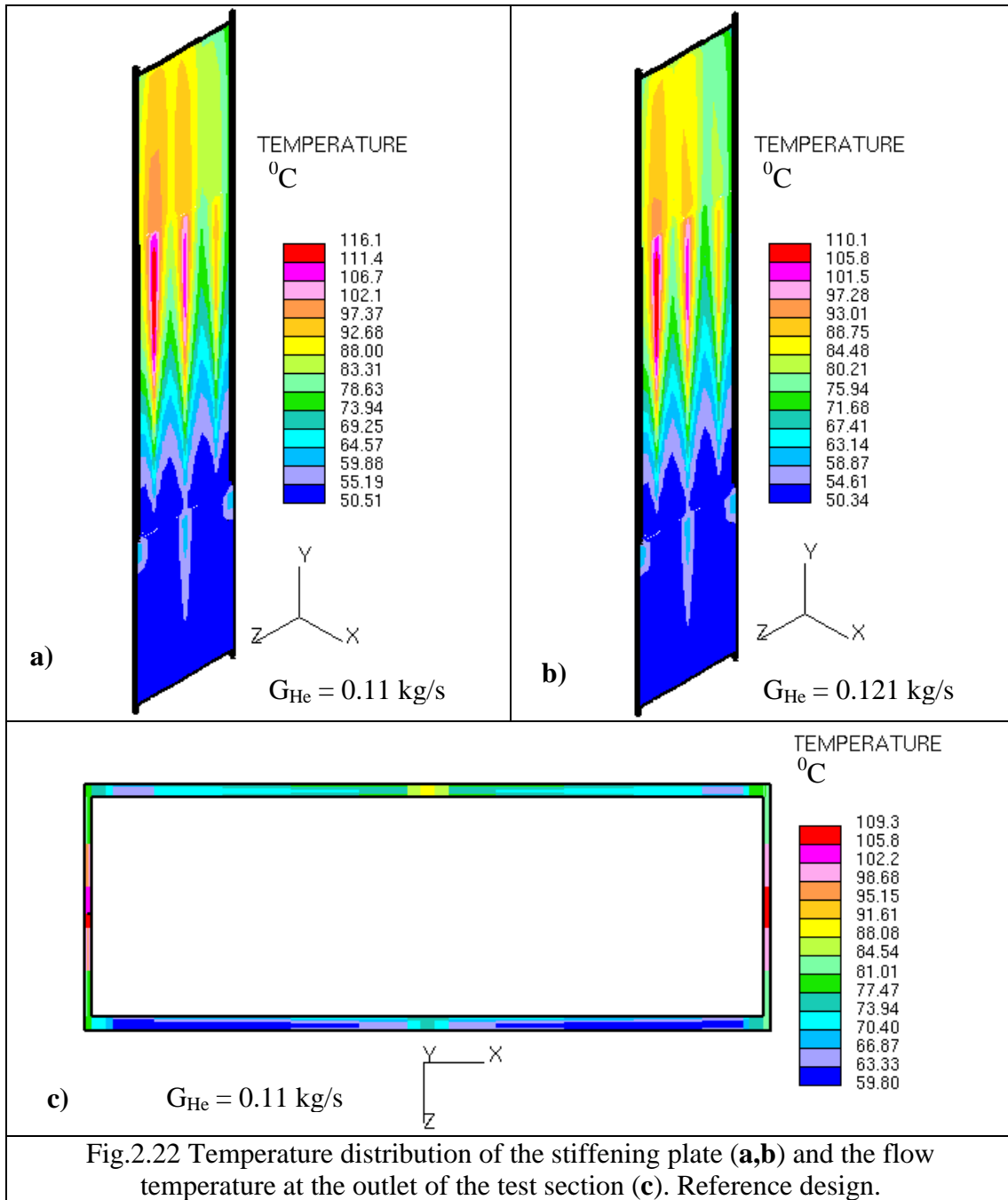
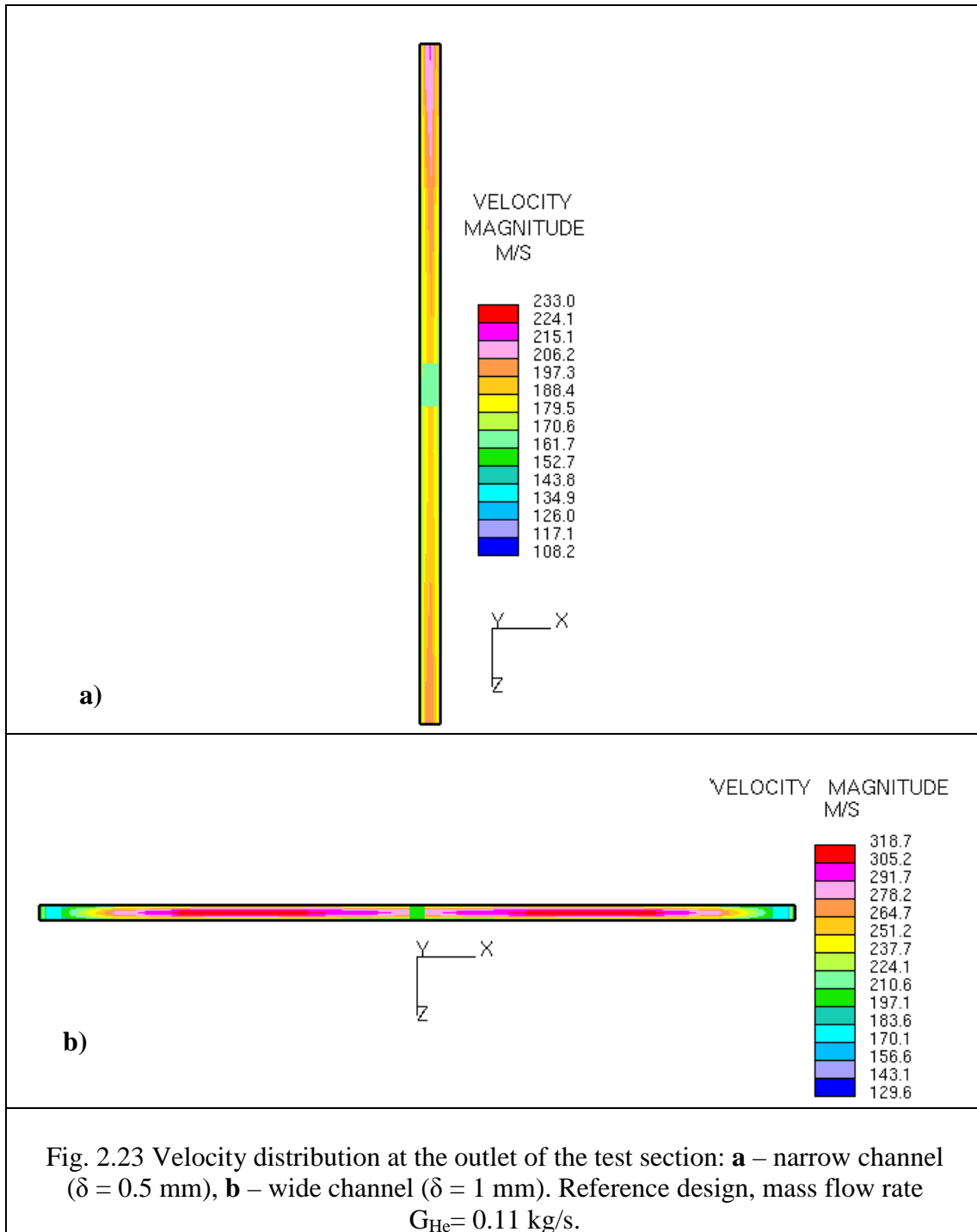
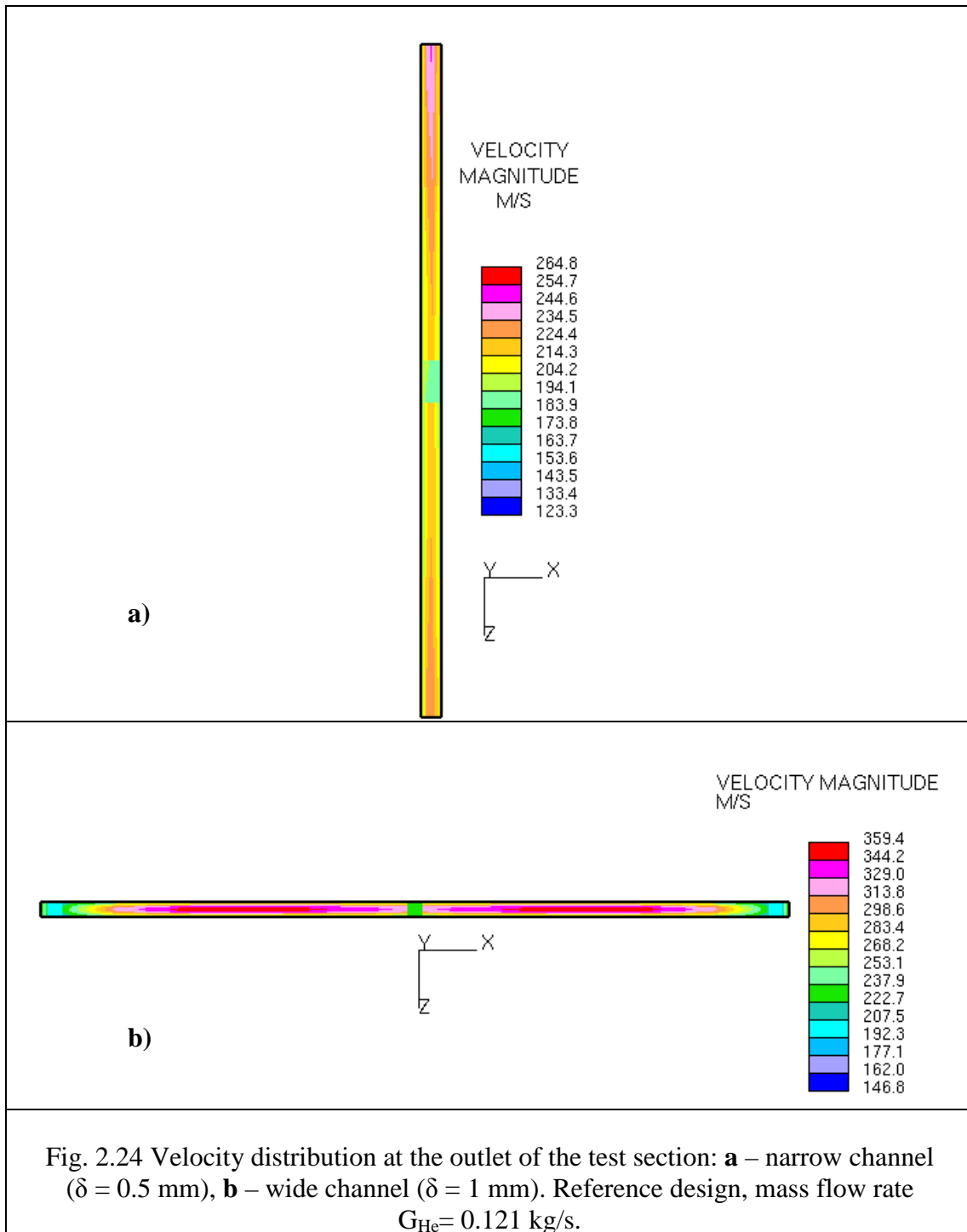
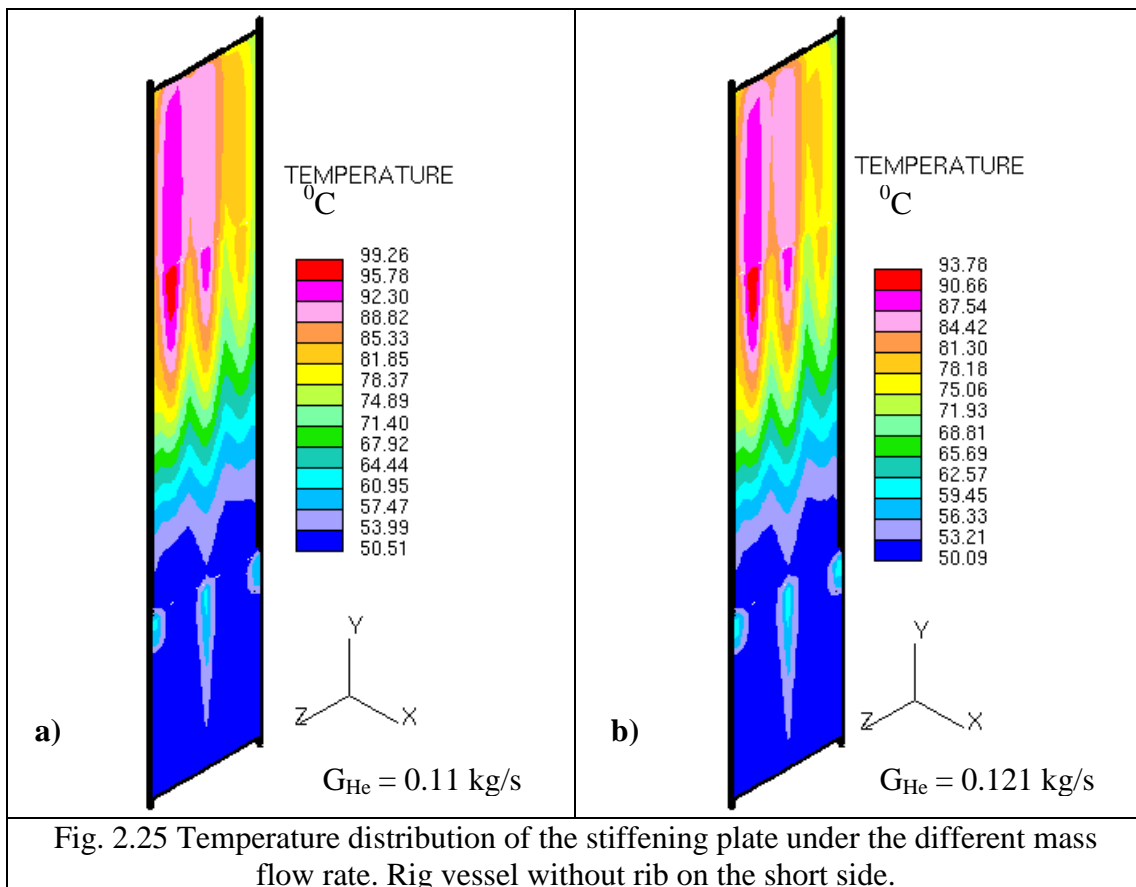
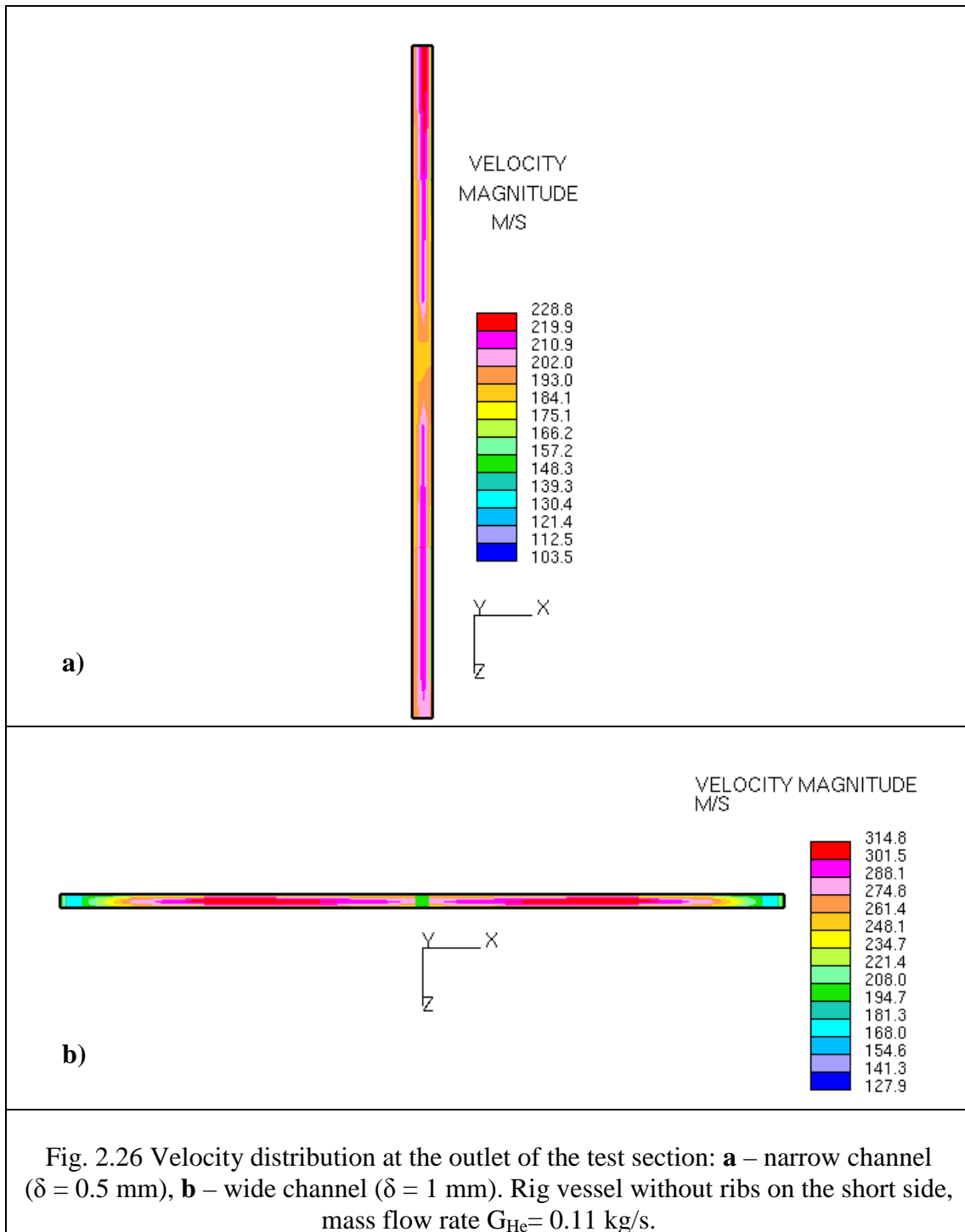


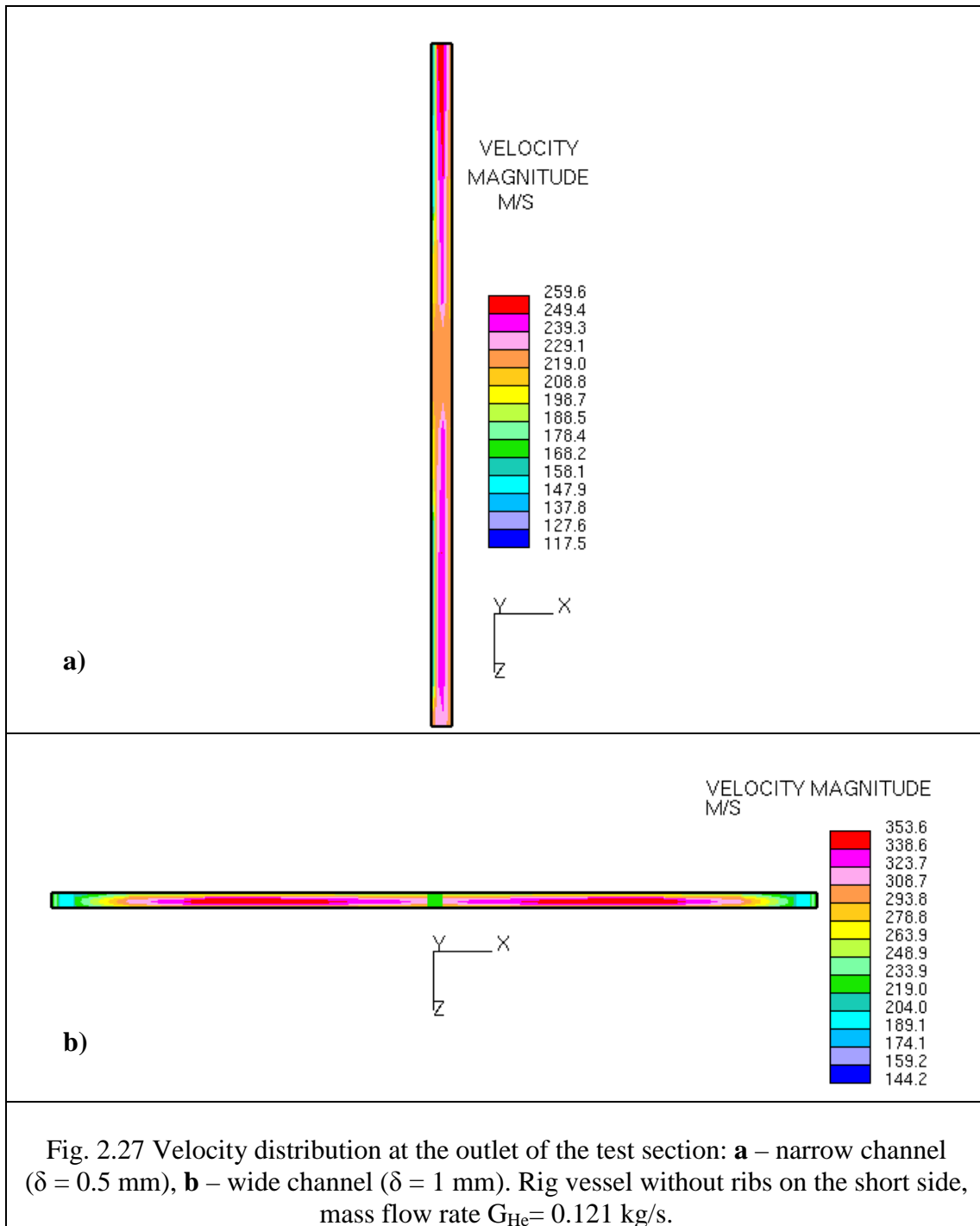
Fig.2.22 Temperature distribution of the stiffening plate (a,b) and the flow temperature at the outlet of the test section (c). Reference design.











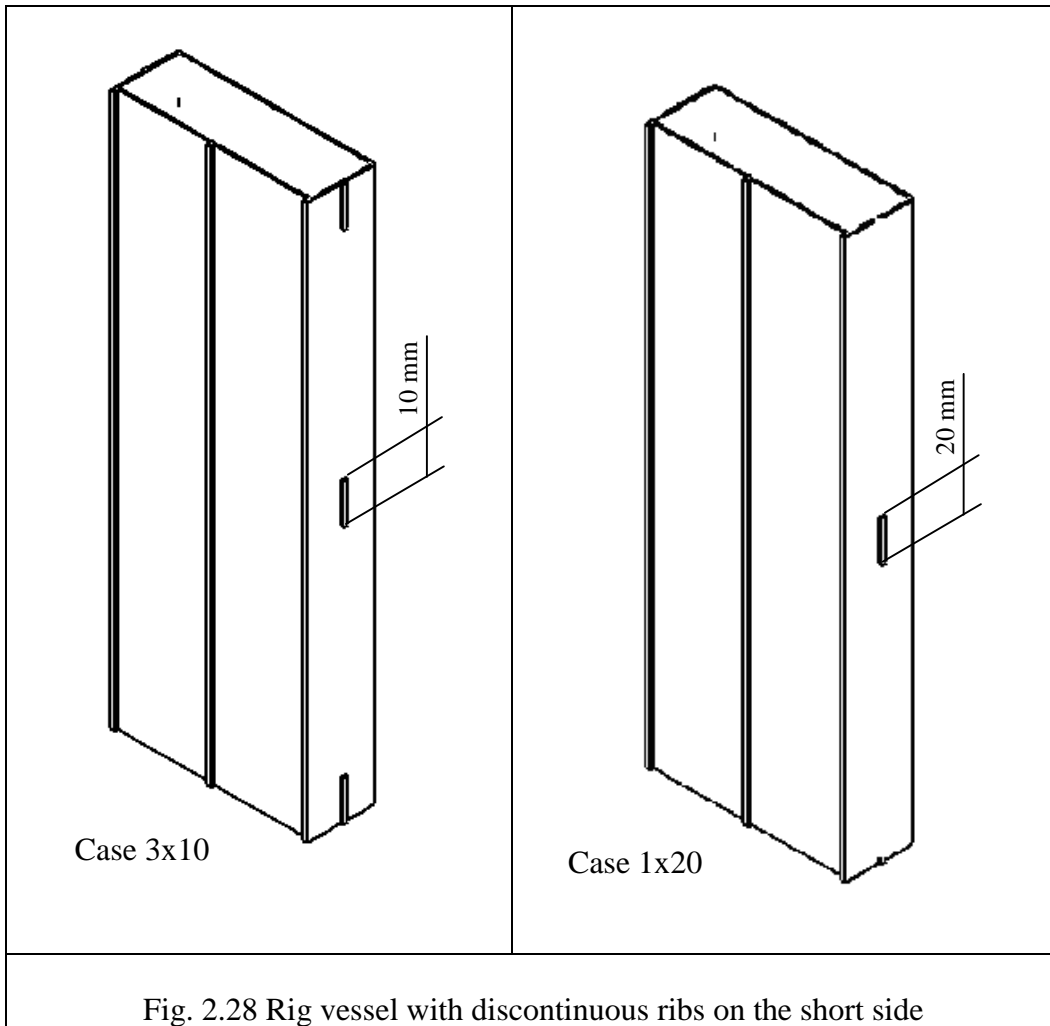


Fig. 2.28 Rig vessel with discontinuous ribs on the short side

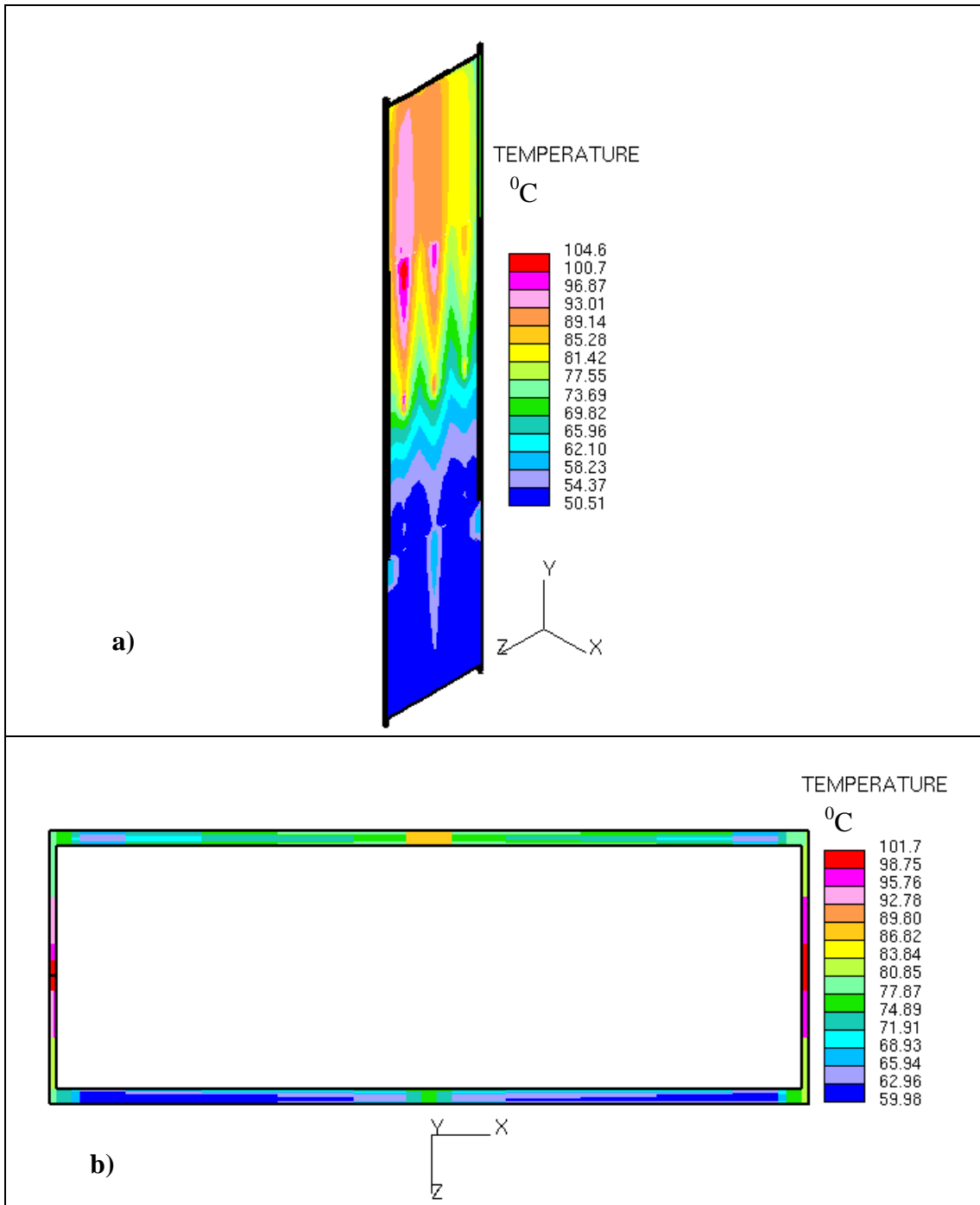
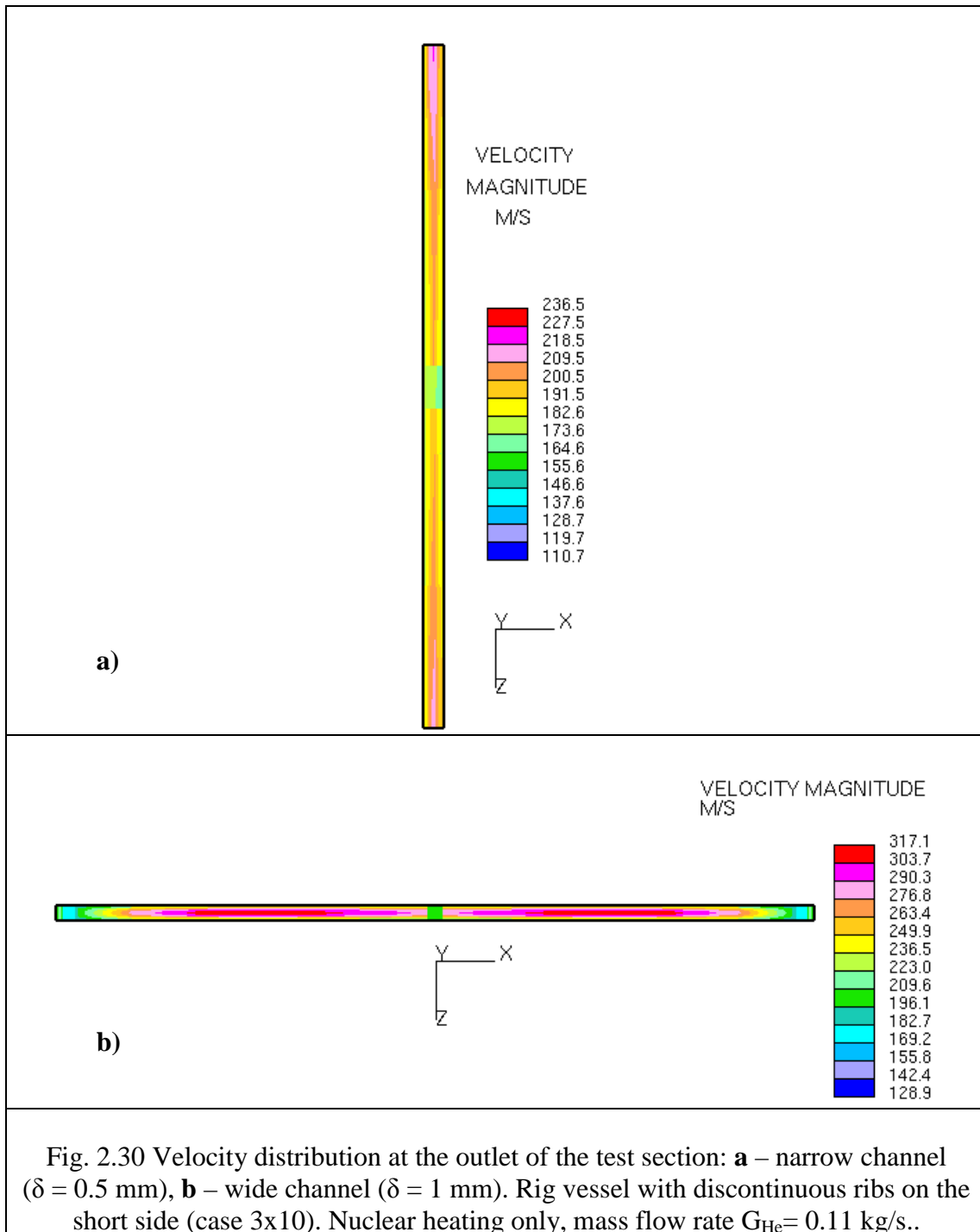
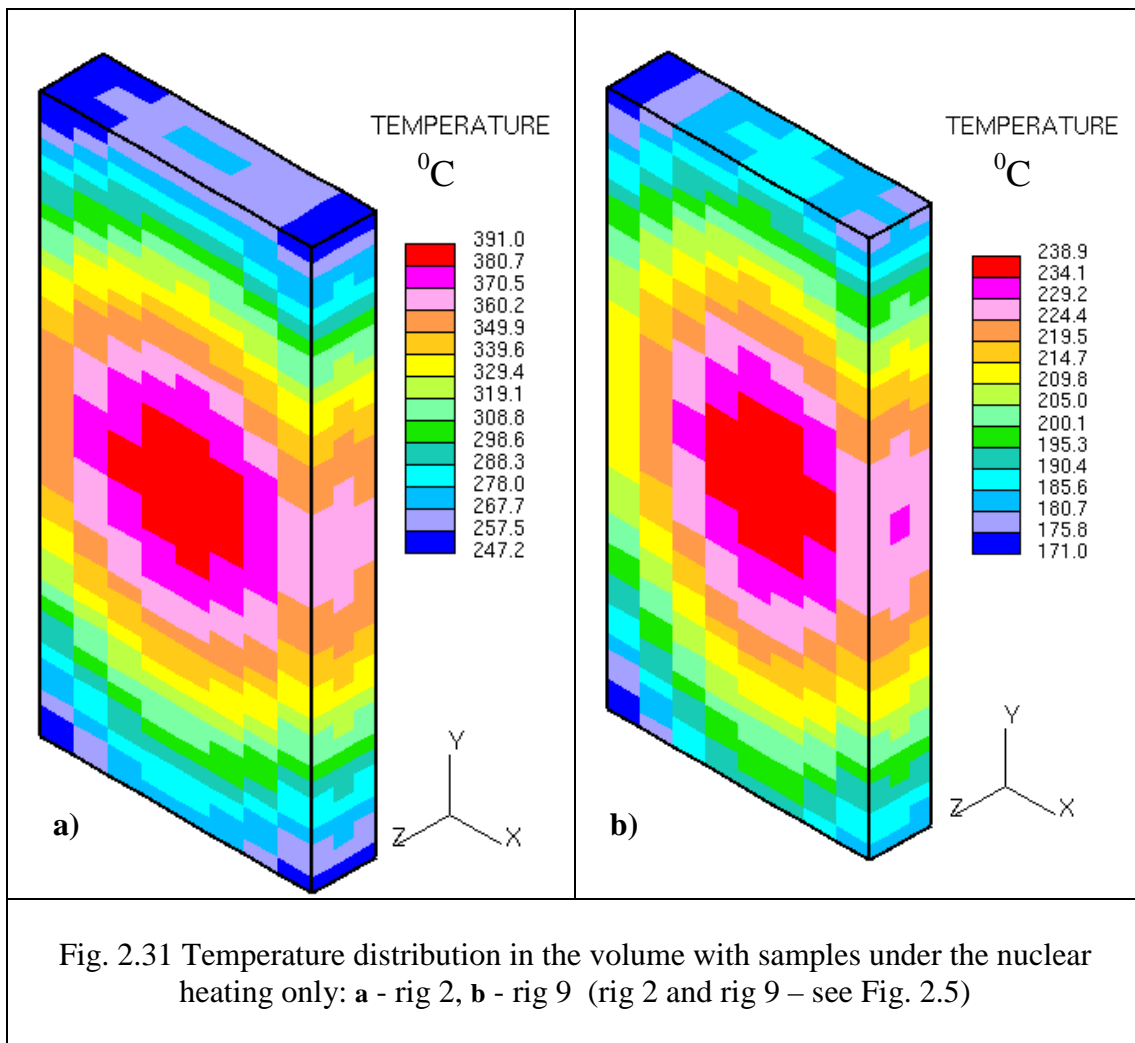


Fig. 2.29 Temperature distribution of the stiffening plate **(a)** and the flow temperature at the outlet of the test section **(b)**. Rig vessel with discontinuous ribs on the short side (case 3x10). Nuclear heating only, mass flow rate  $G_{\text{He}} = 0.11 \text{ kg/s}$ .





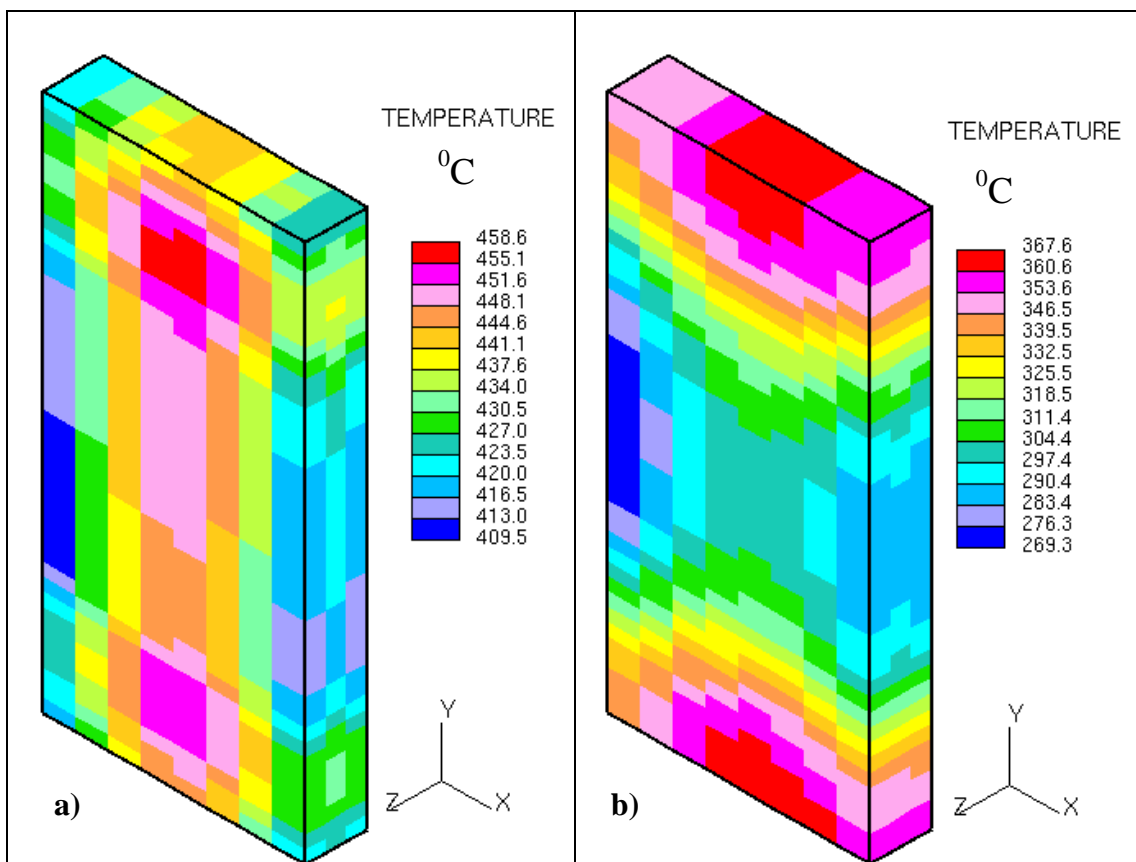
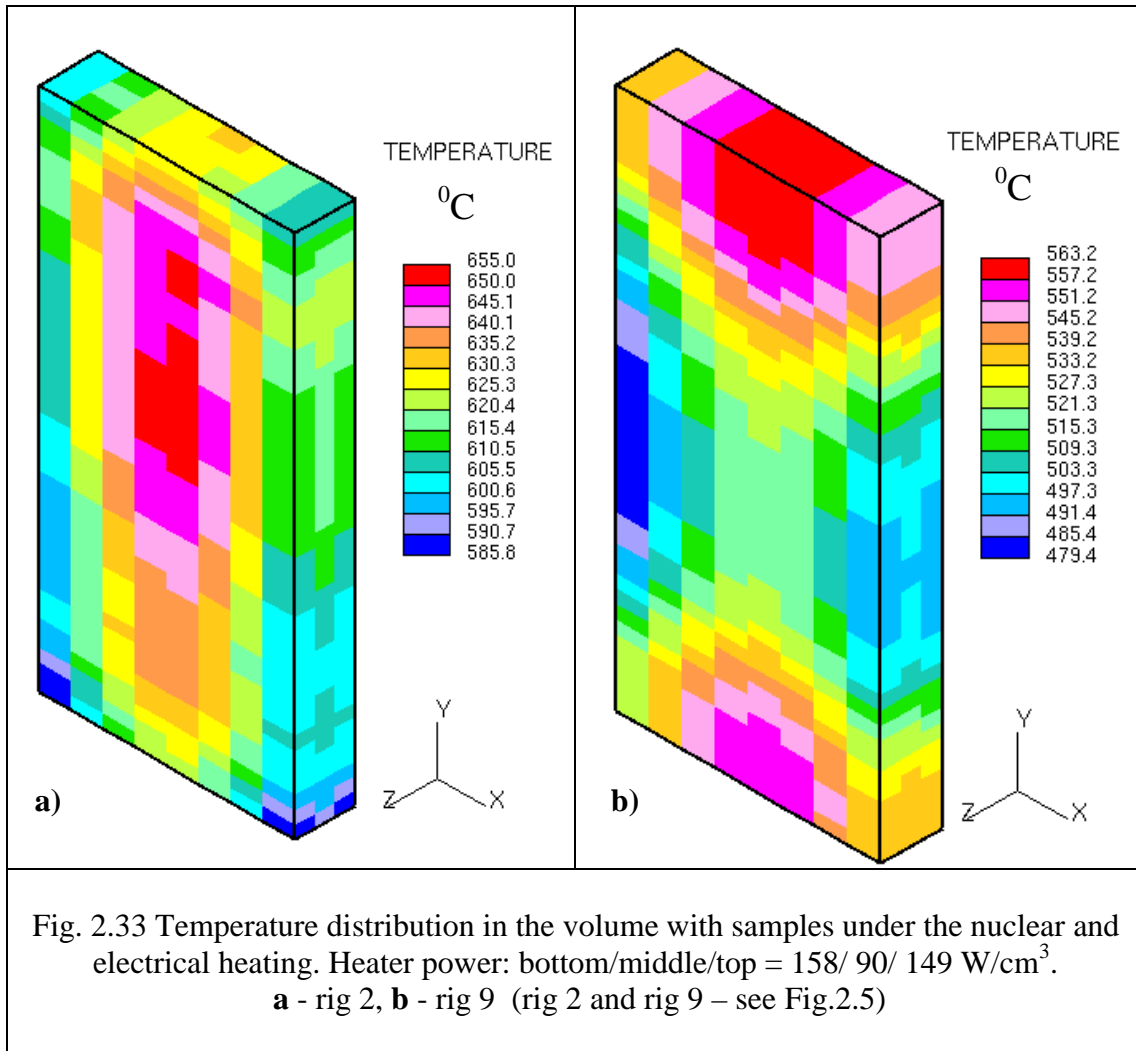
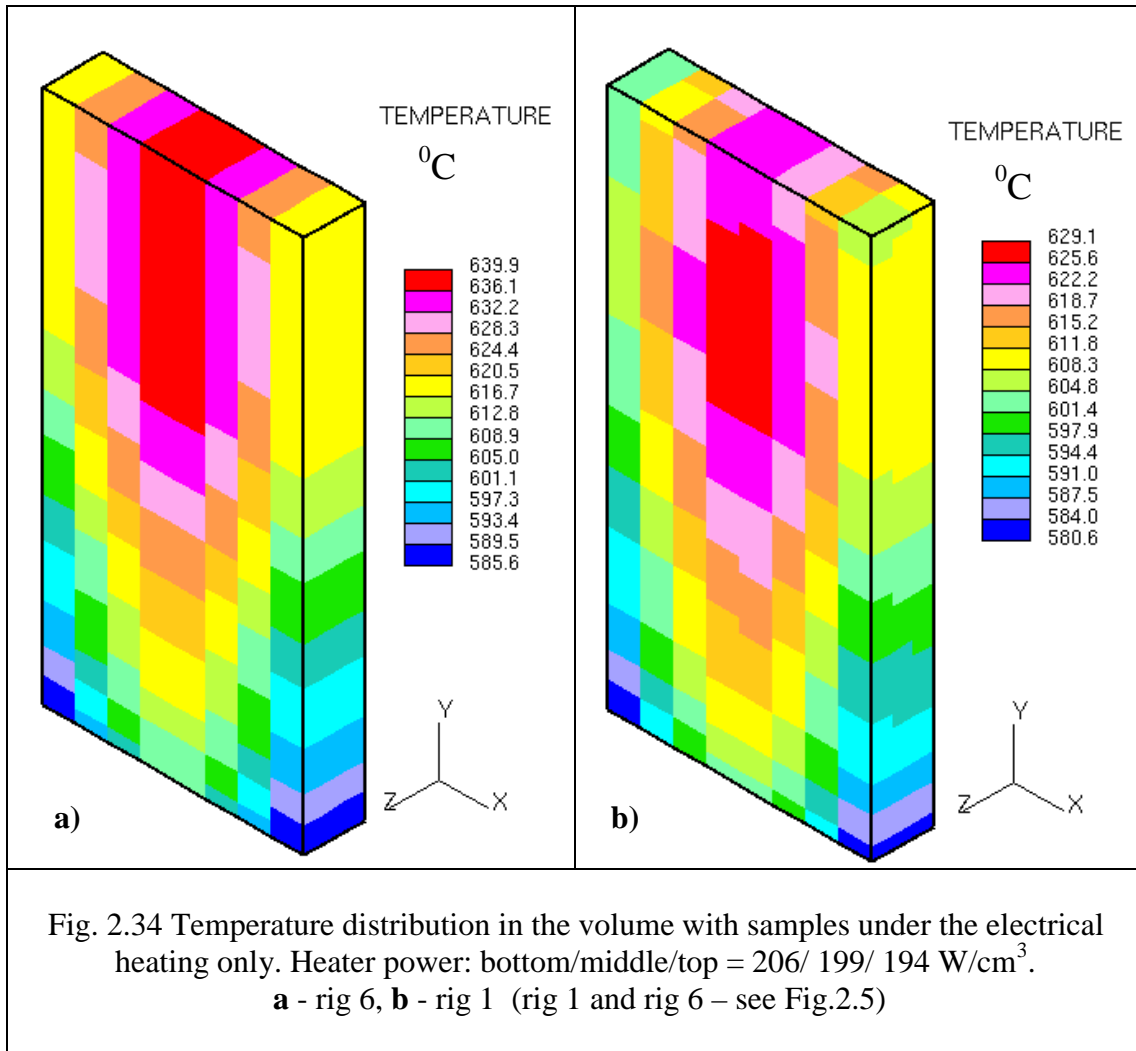


Fig. 2.32 Temperature distribution in the volume with samples under the nuclear and electrical heating. Heater power: bottom/middle/top = 74/ 0/ 71 W/cm<sup>3</sup>.

**a** - rig 2, **b** - rig 9 (rig 2 and rig 9 – see Fig. 2.5)





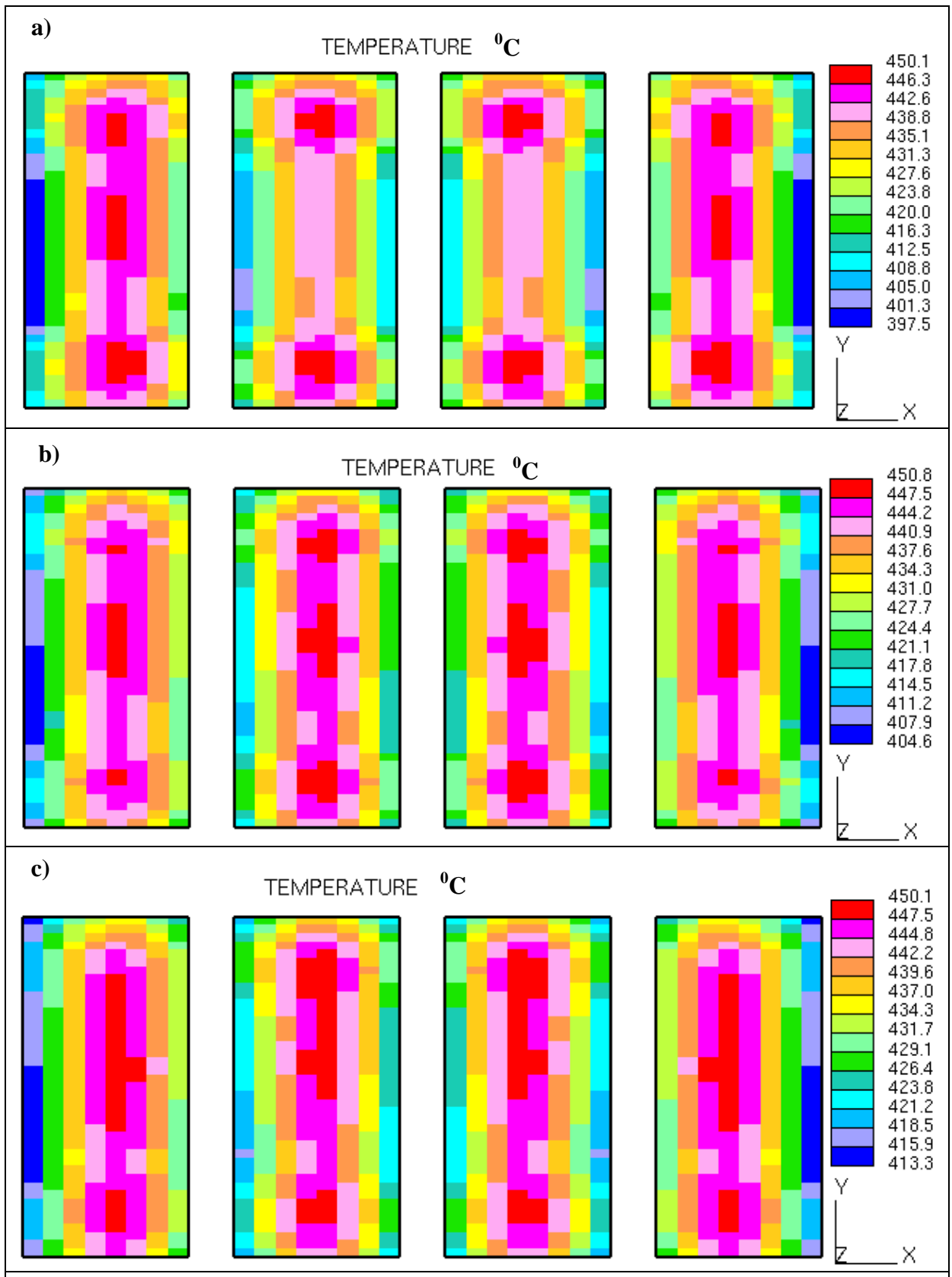


Fig. 2.35. Temperature field in the volume with samples for the temperature level of  $\sim 450^{\circ}\text{C}$ . **a** – first row of rigs (rig 1-4), **b** – second row of rigs (rig 5-8), **c** – third row of rigs (rig 9-12). Rig numbering see Fig.2.5

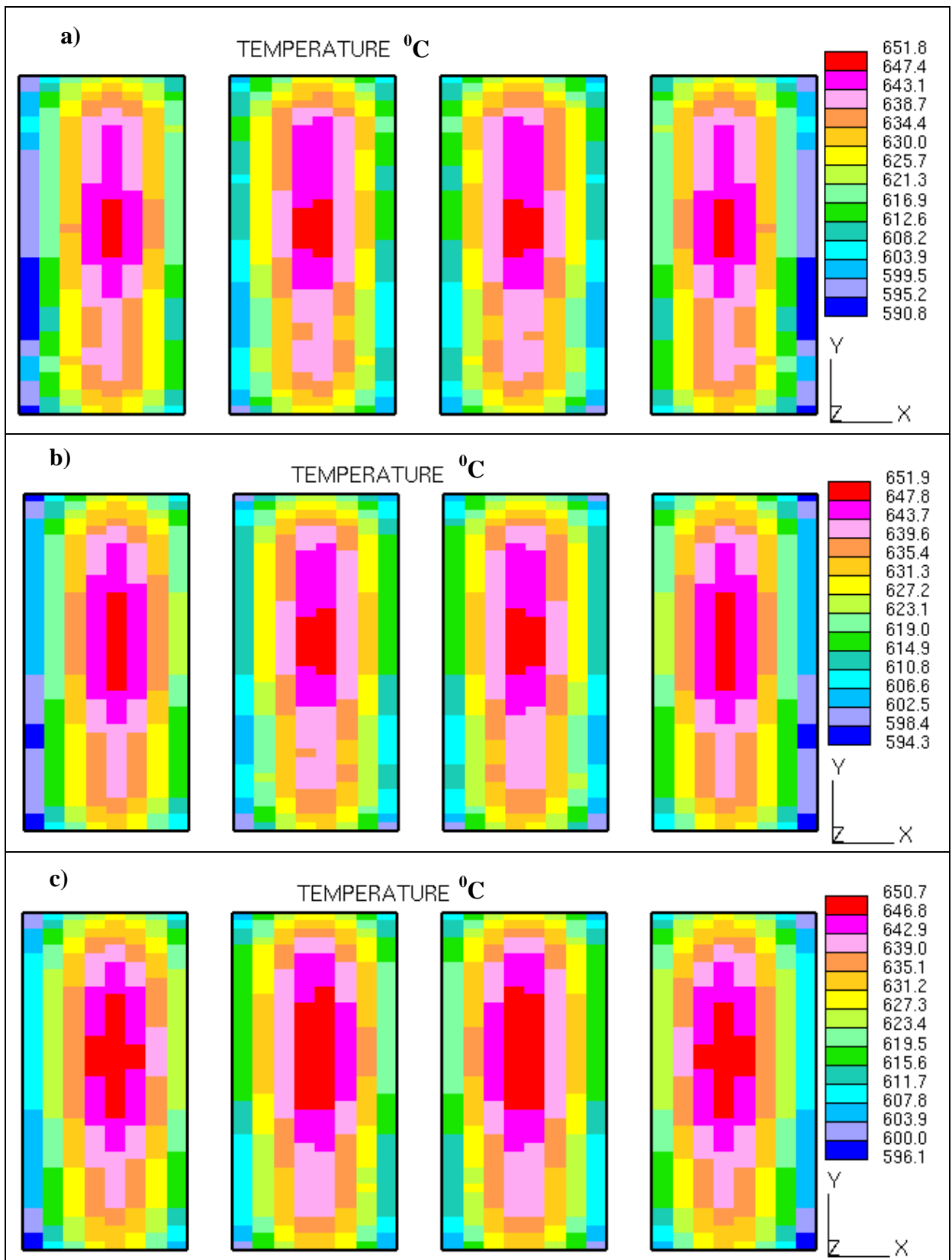


Fig. 2.36. Temperature field in the volume with samples for the temperature level of  $\sim 650^{\circ}\text{C}$ . **a** – first row of rigs (rig 1-4), **b** – second row of rigs (rig 5-8), **c** – third row of rigs (rig 9-12). Rig numbering see Fig.2.5

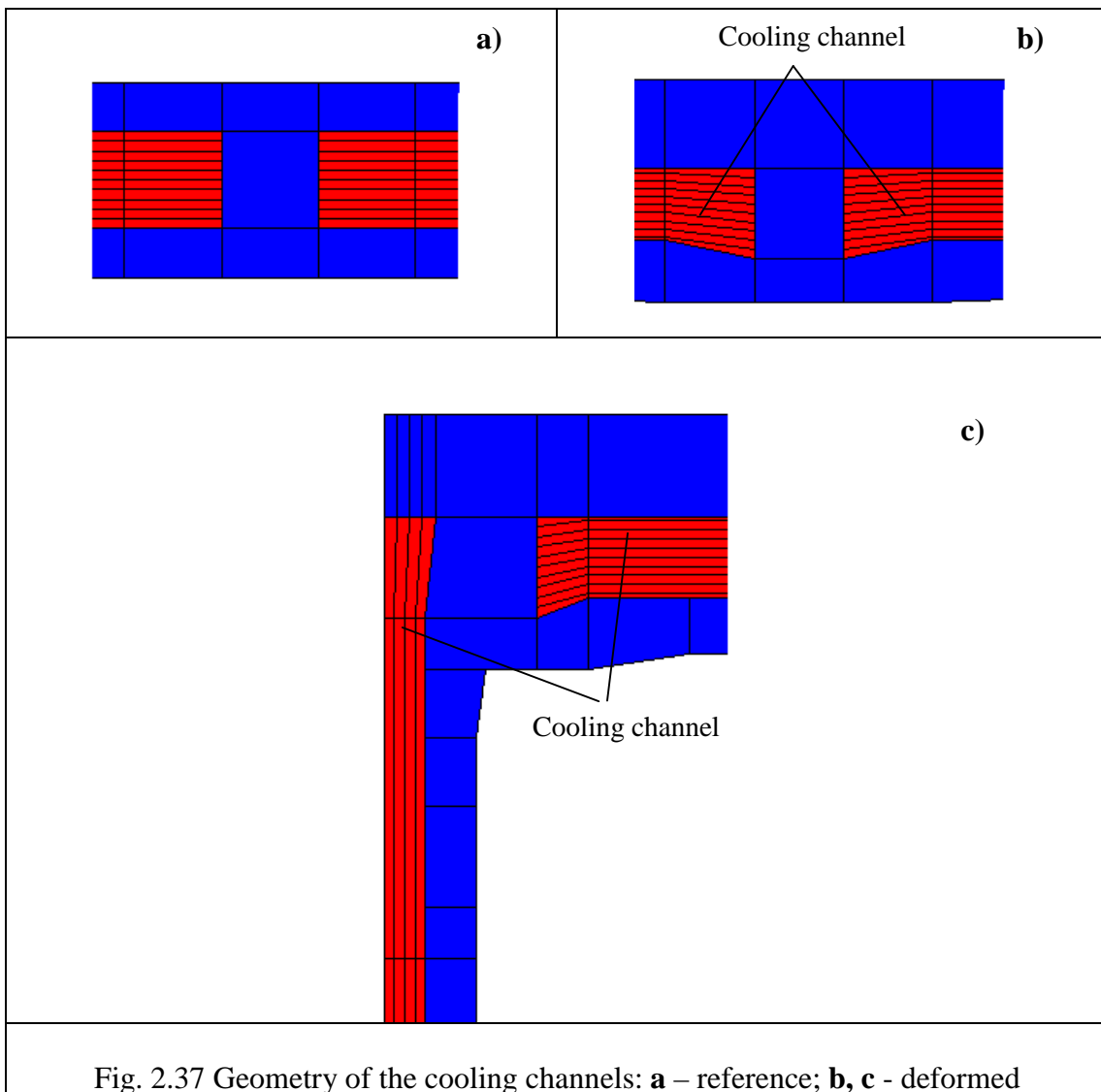


Fig. 2.37 Geometry of the cooling channels: **a** – reference; **b, c** - deformed

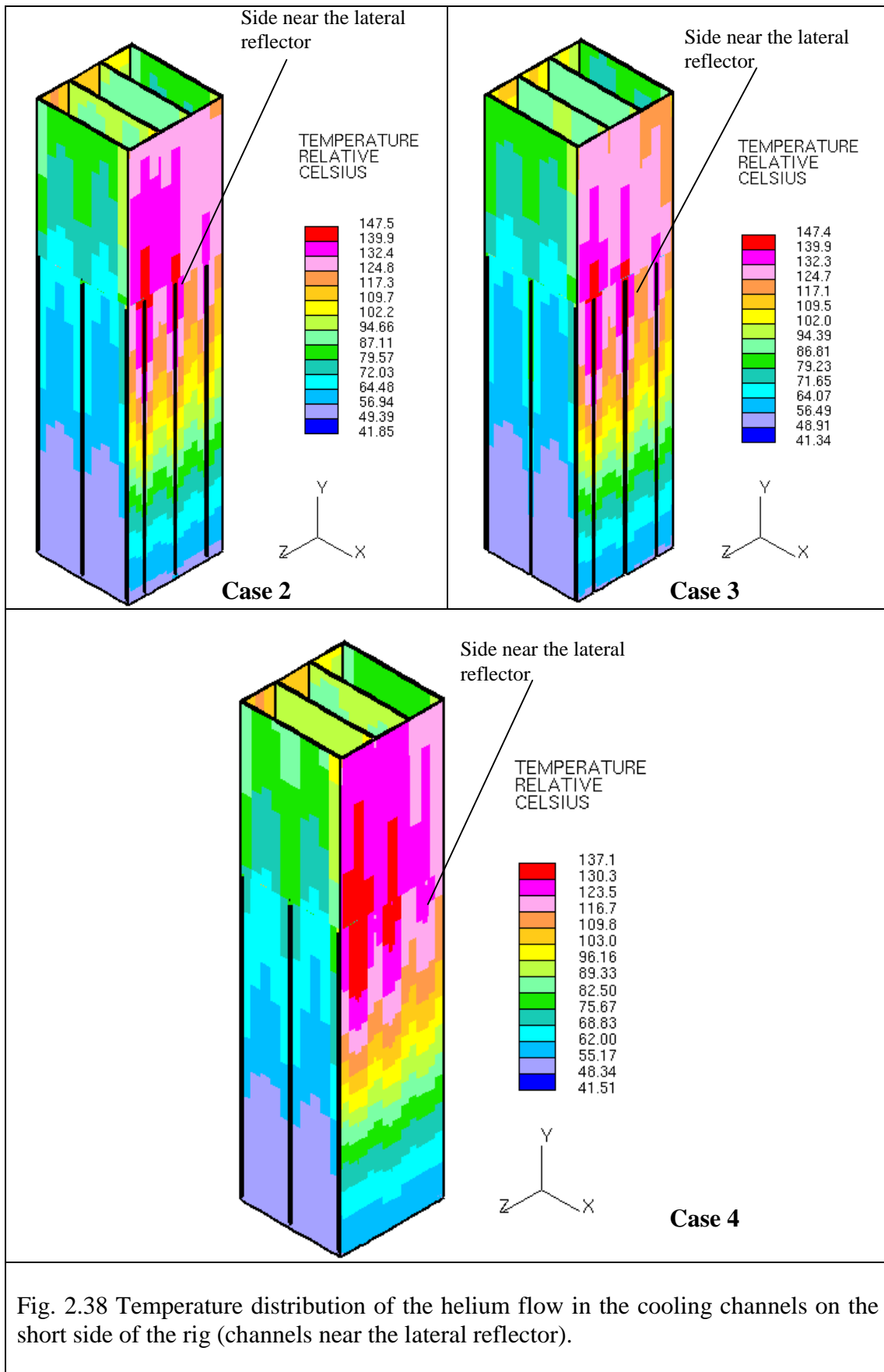


Fig. 2.38 Temperature distribution of the helium flow in the cooling channels on the short side of the rig (channels near the lateral reflector).

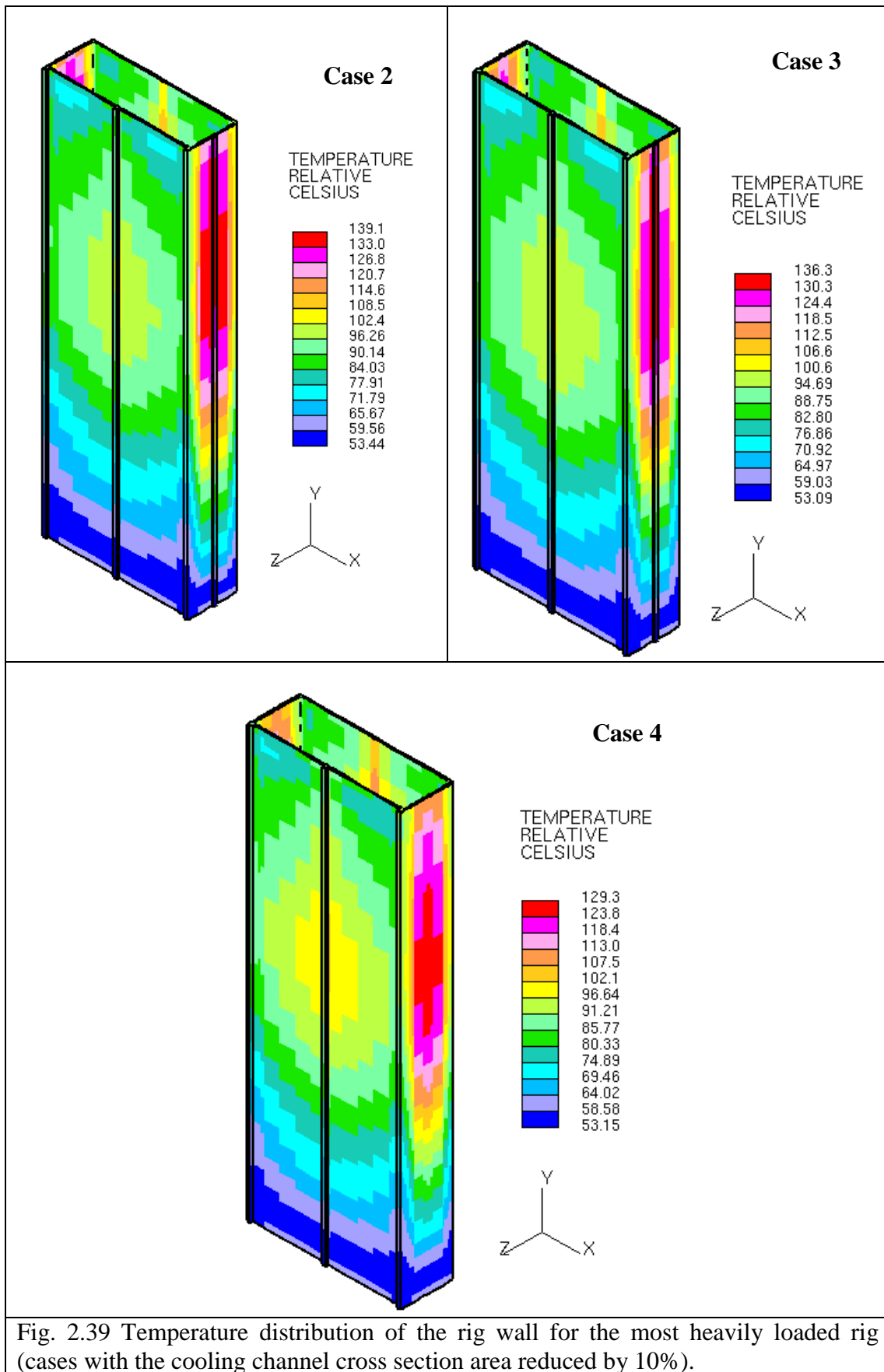


Fig. 2.39 Temperature distribution of the rig wall for the most heavily loaded rig (cases with the cooling channel cross section area reduced by 10%).

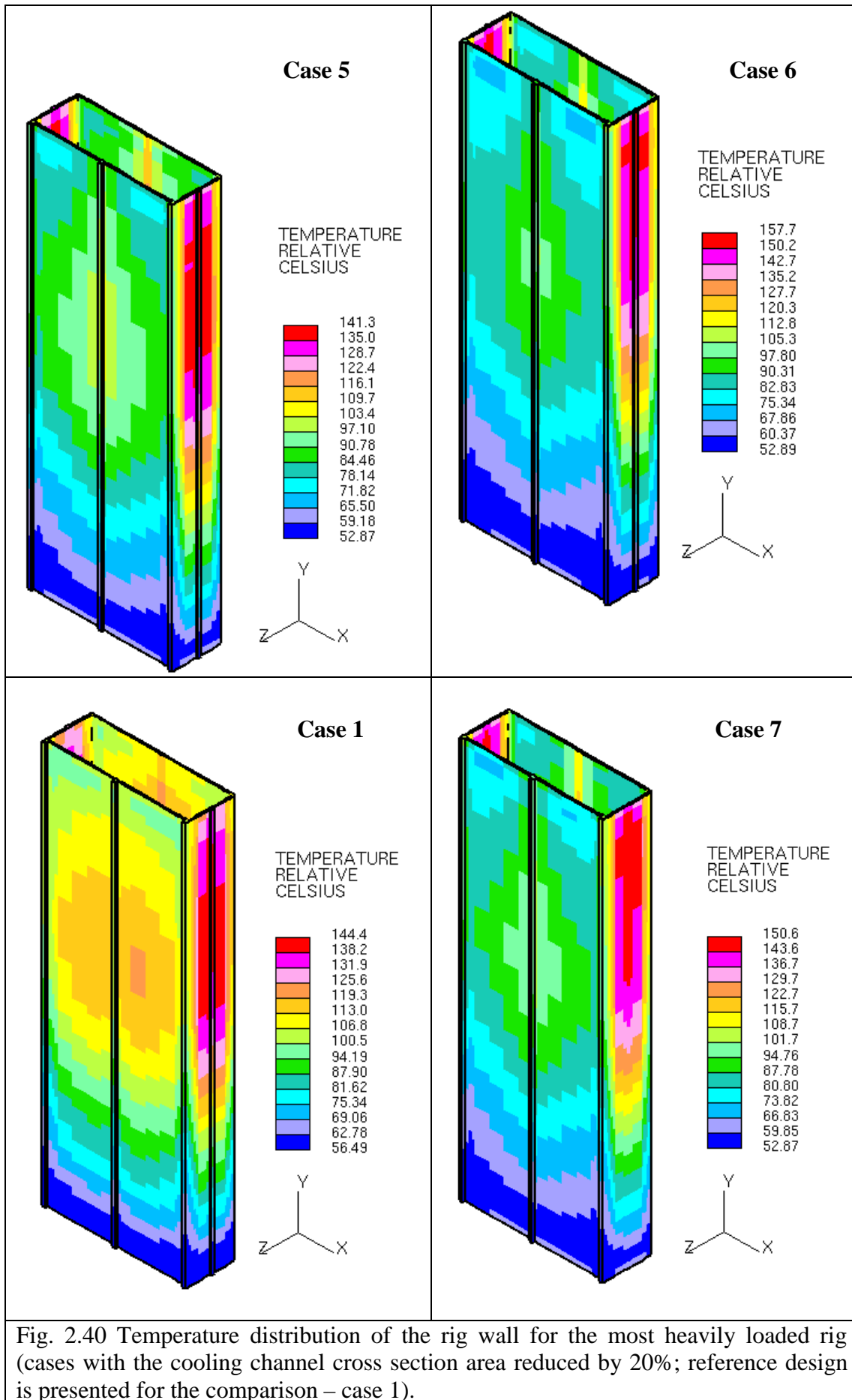


Fig. 2.40 Temperature distribution of the rig wall for the most heavily loaded rig (cases with the cooling channel cross section area reduced by 20%; reference design is presented for the comparison – case 1).

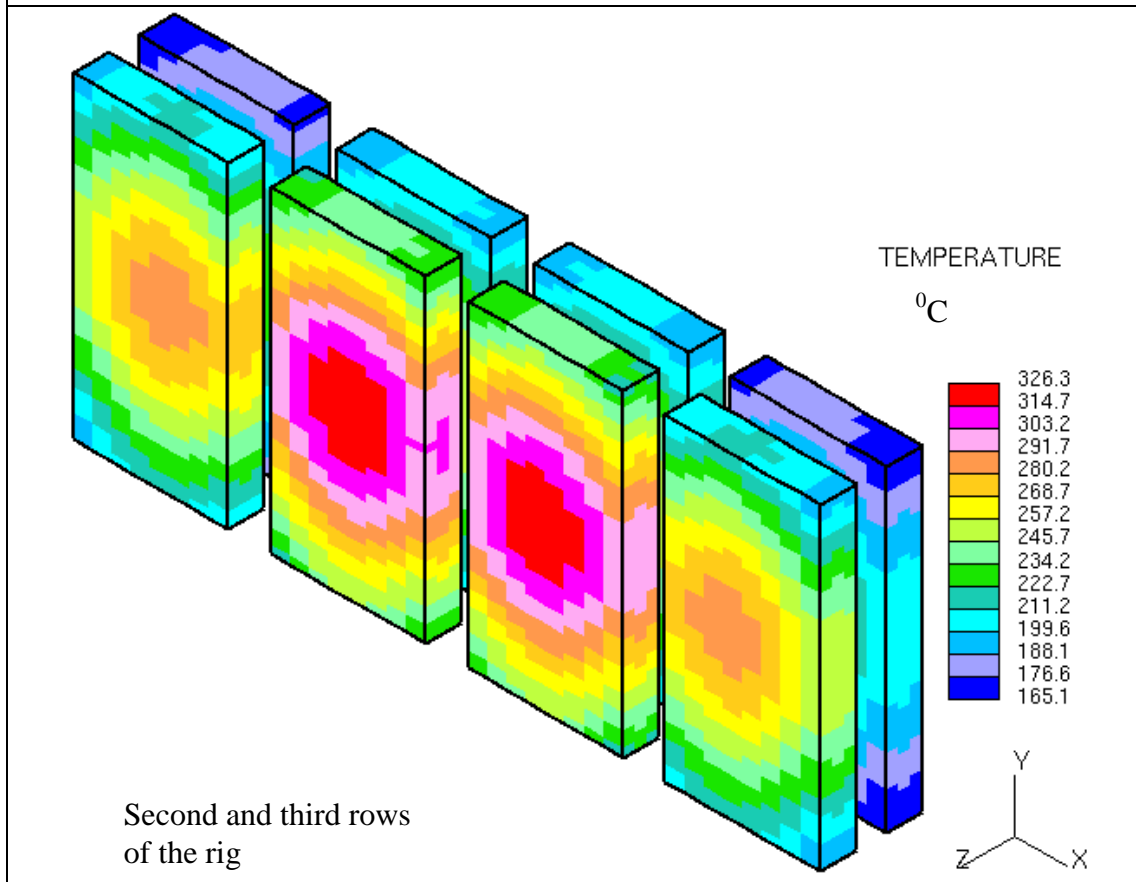
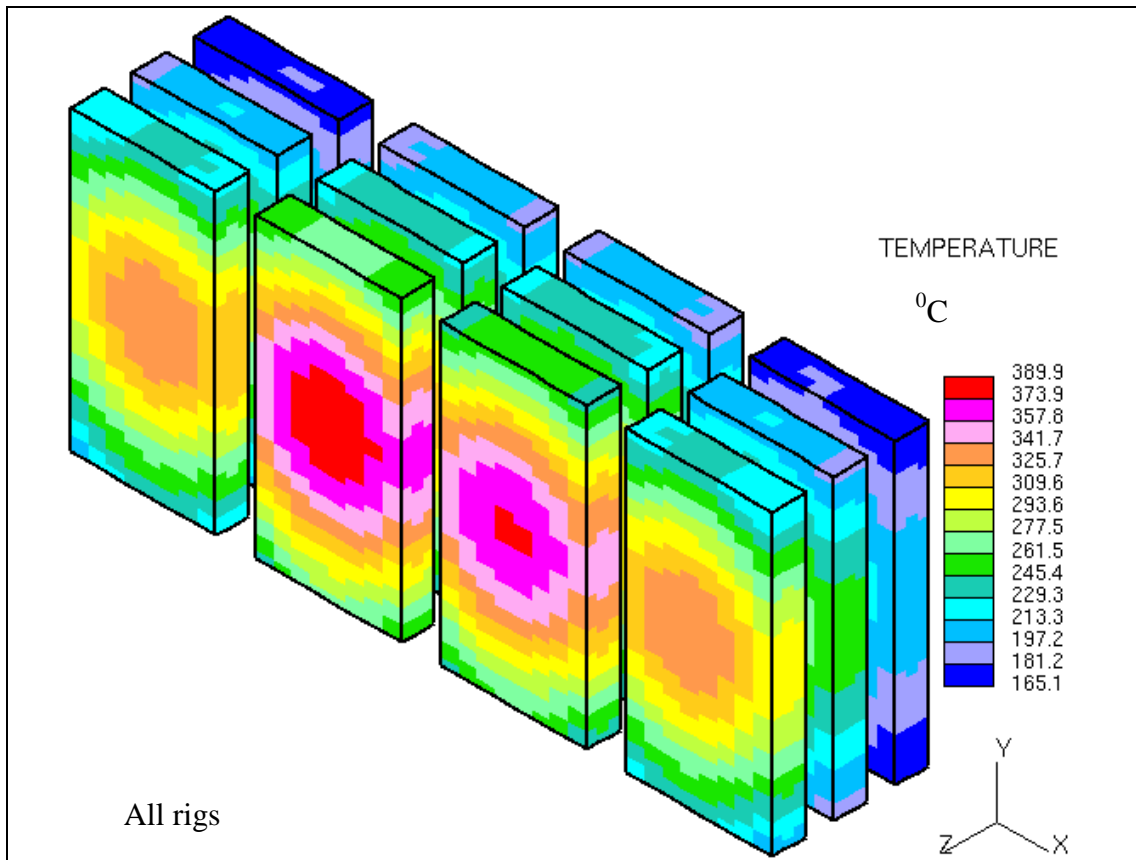


Fig. 2.41 Temperature distribution in the volume with samples for case 8.

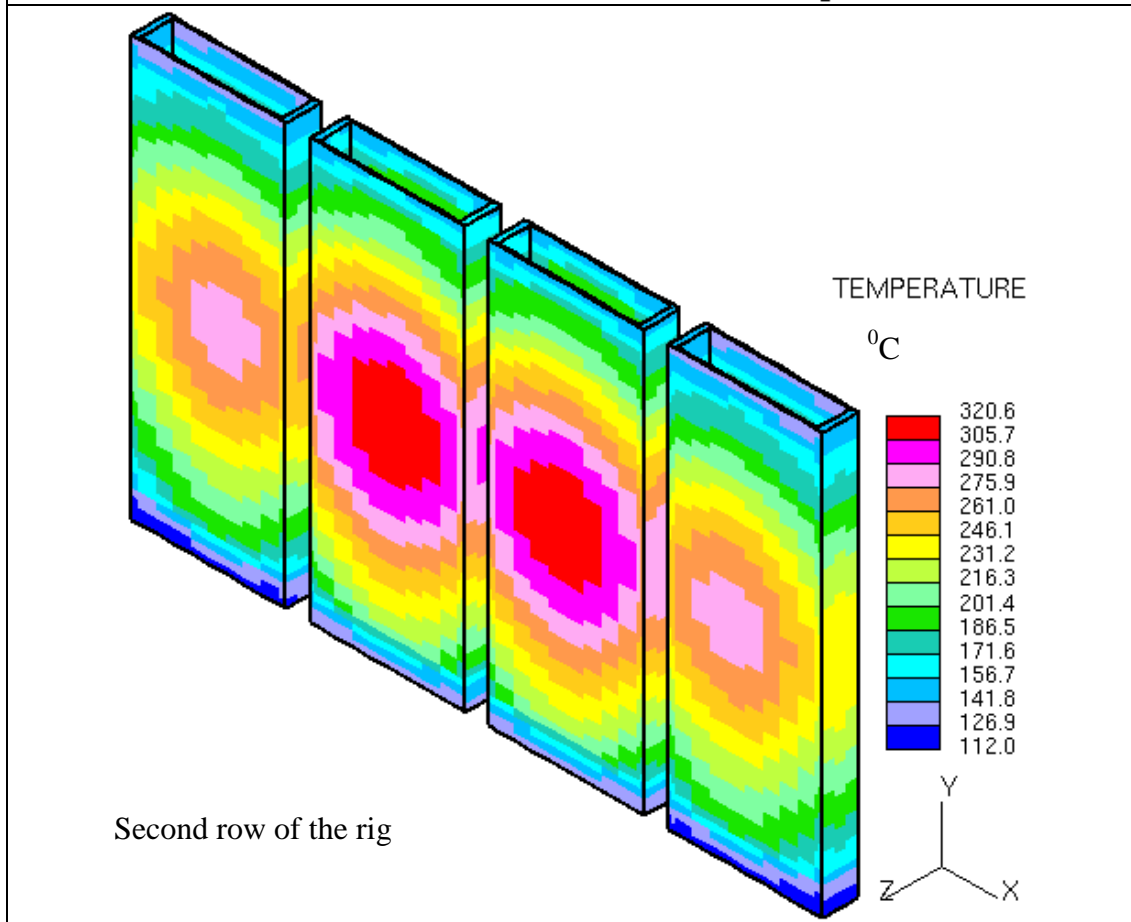
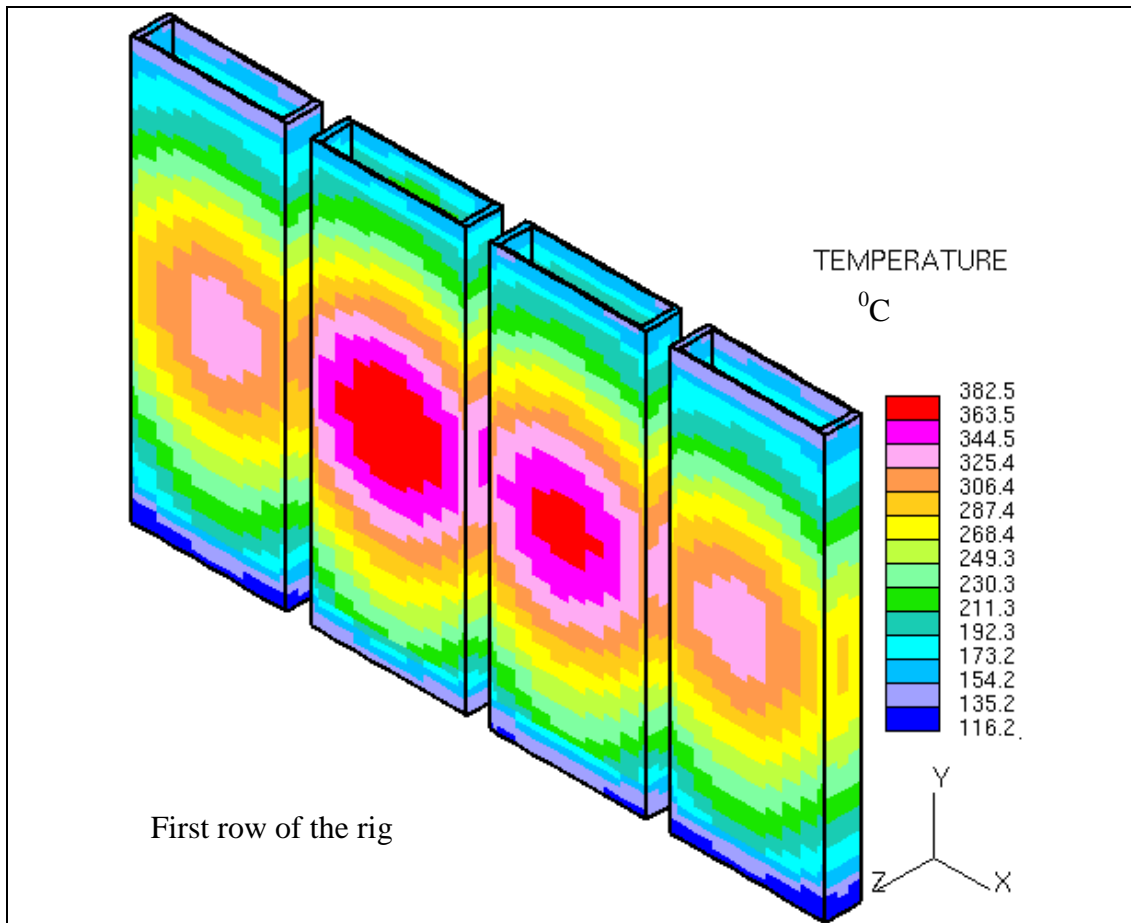


Fig. 2.42 Temperature distribution in the capsule walls for case 8.

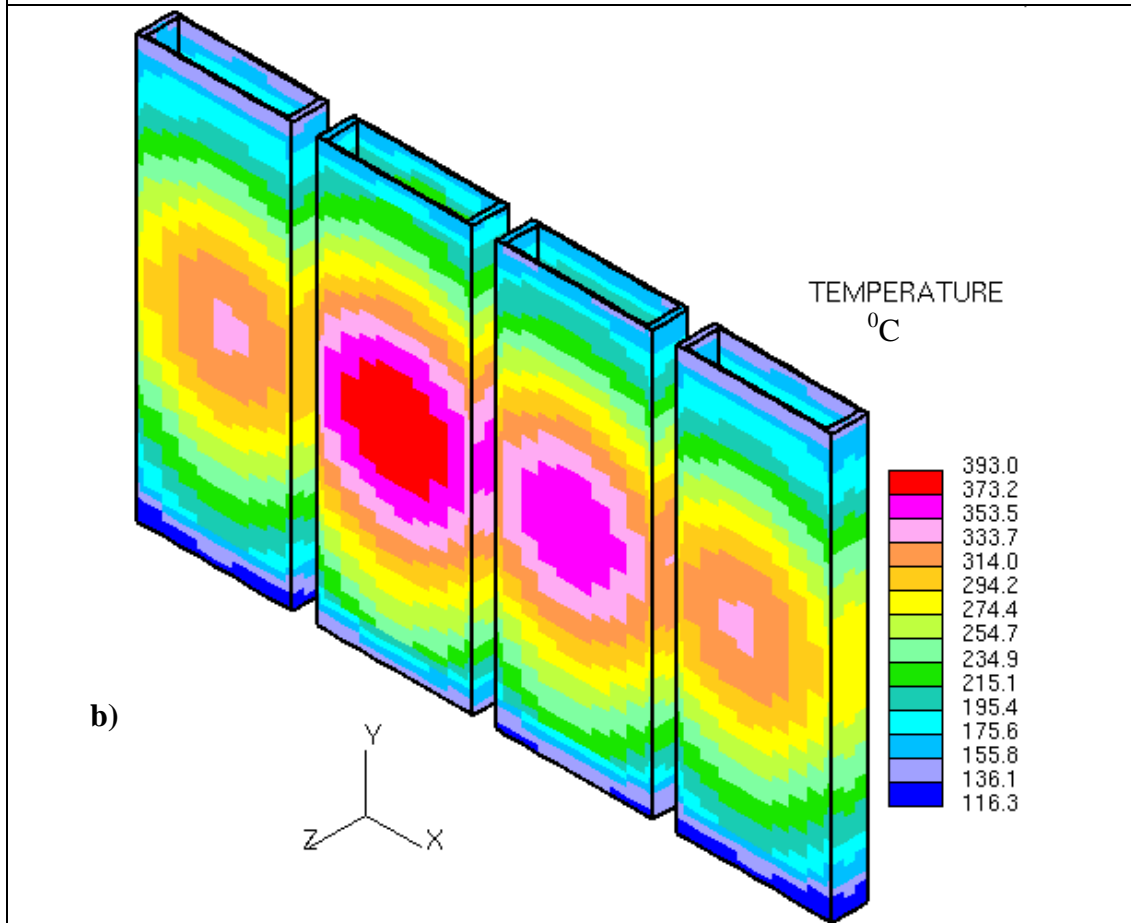
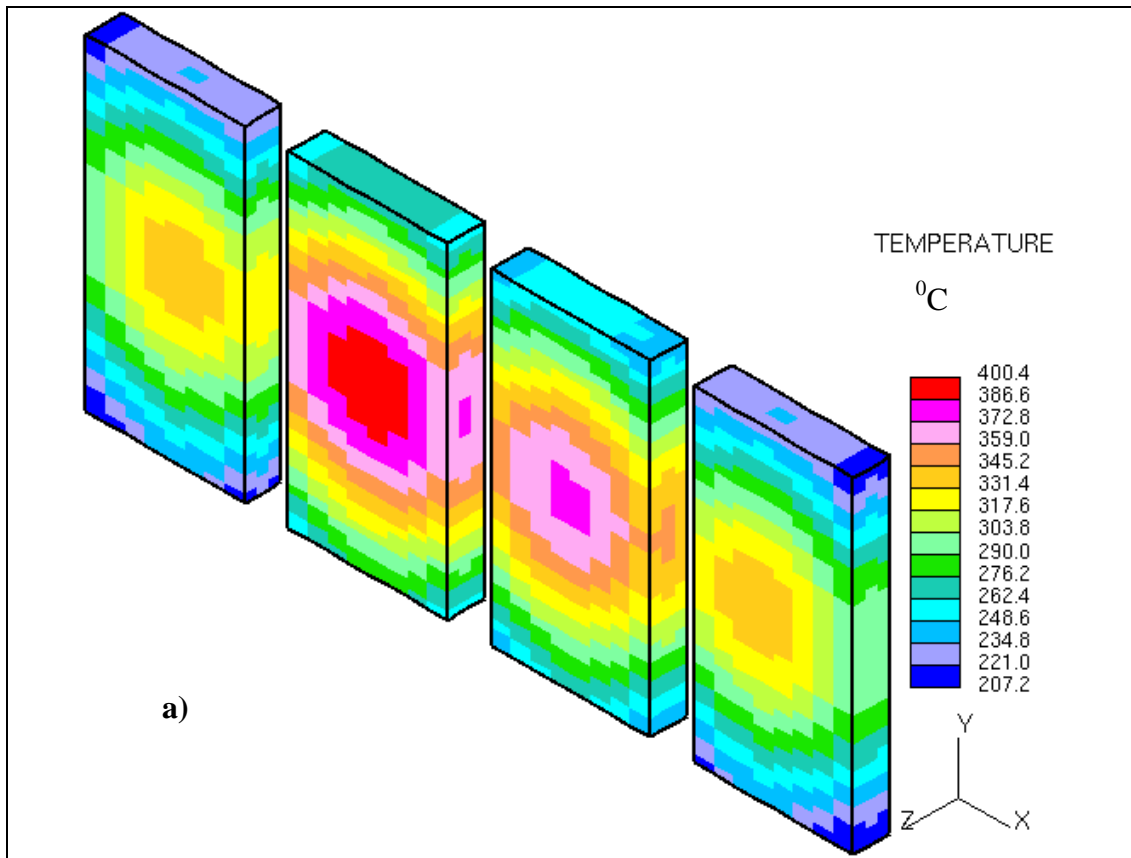


Fig. 2.43. Temperature distribution in the volume with samples (a) and in the capsule walls (b) for case 9.

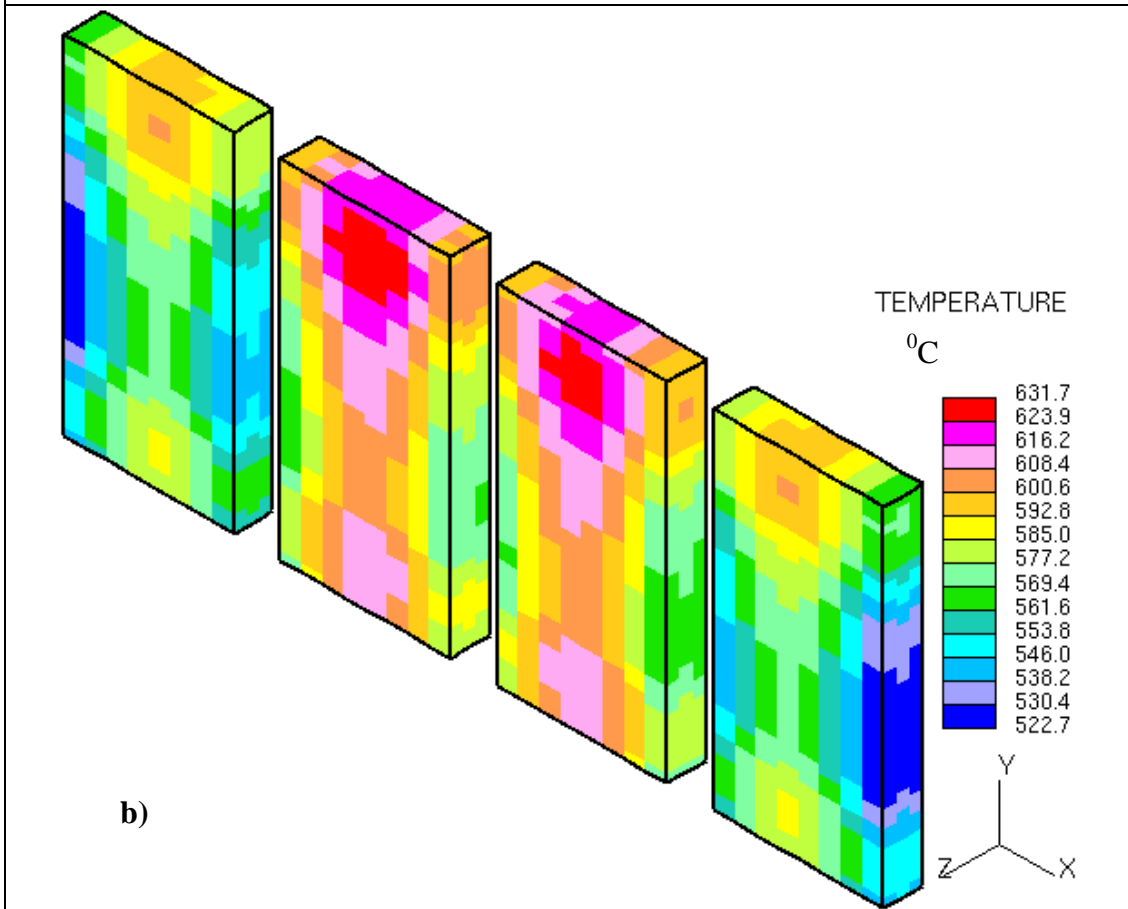
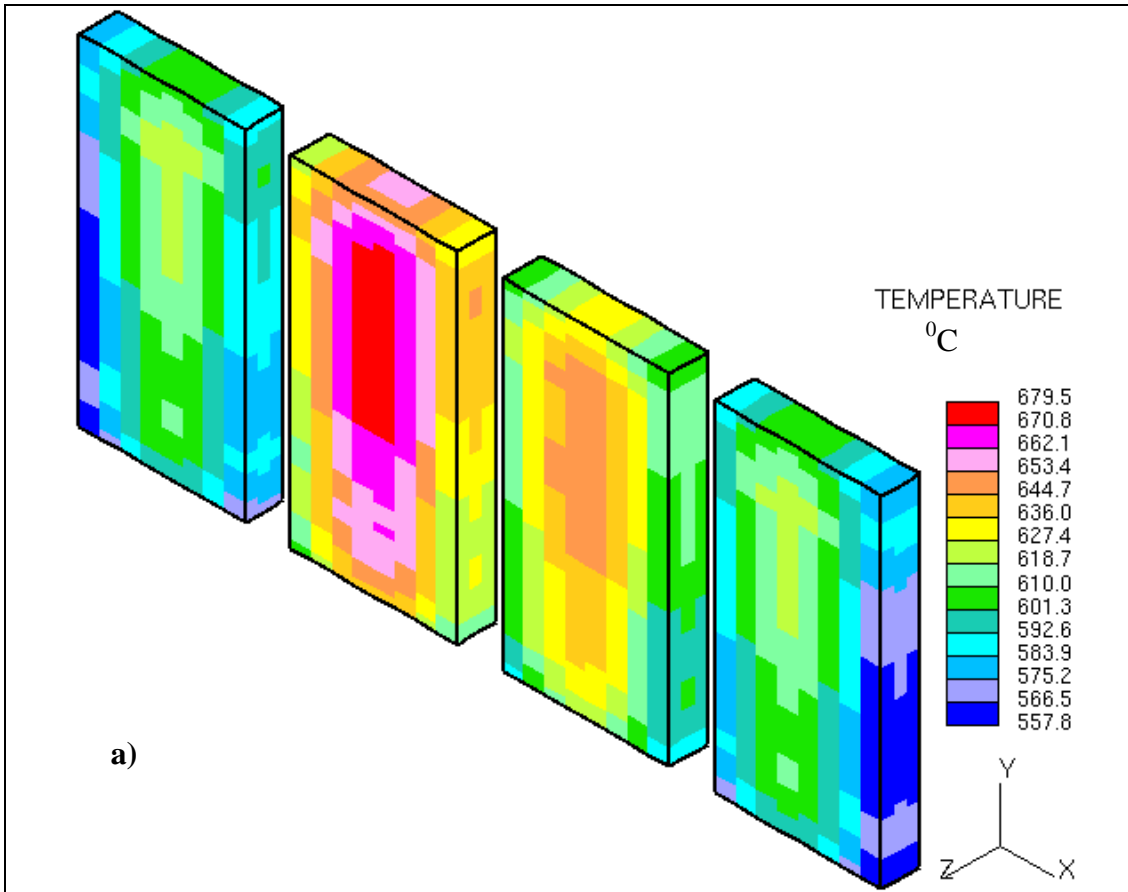


Fig.2.44 Temperature distribution in the volume with samples of the first (a) and second (b) row of rig under nuclear and electrical heating, case 11.

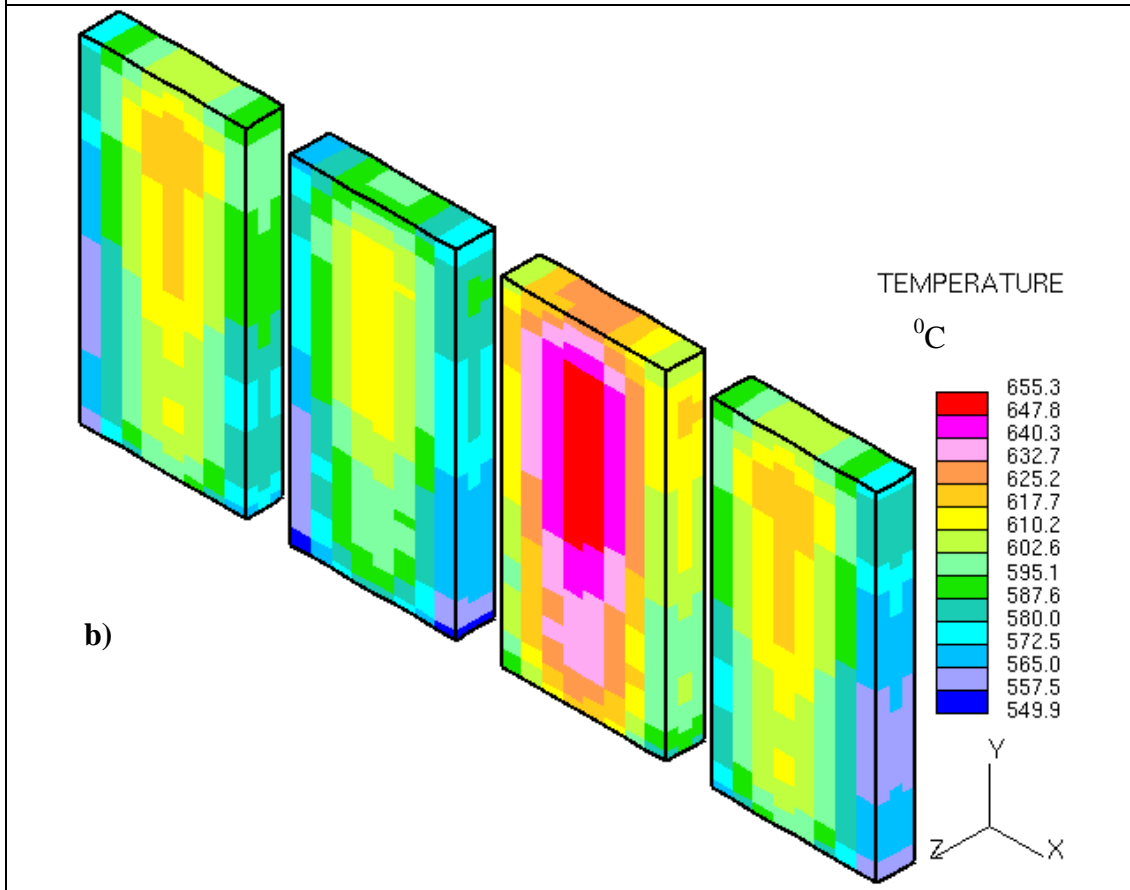
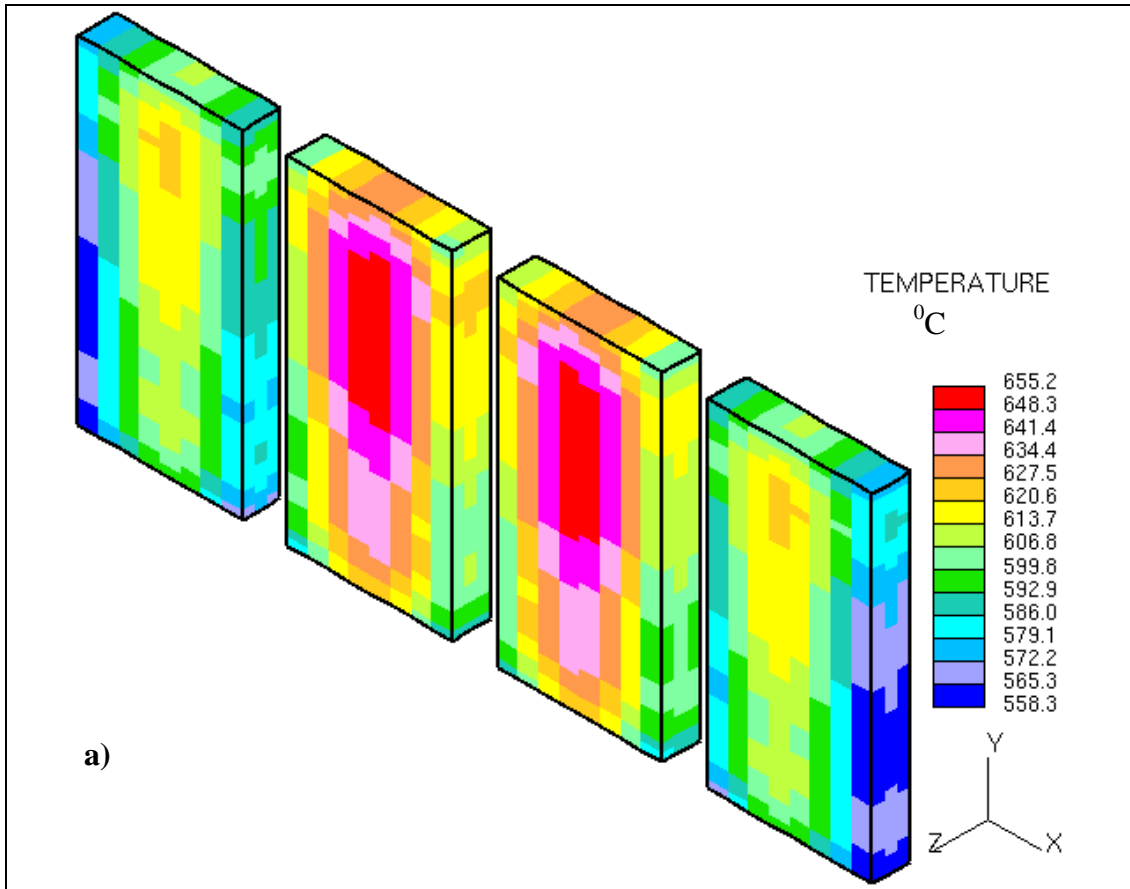


Fig.2.45 Temperature distribution in the volume with samples of the first row of rig under nuclear and electrical heating: **a** – reference design, **b** –case 13.

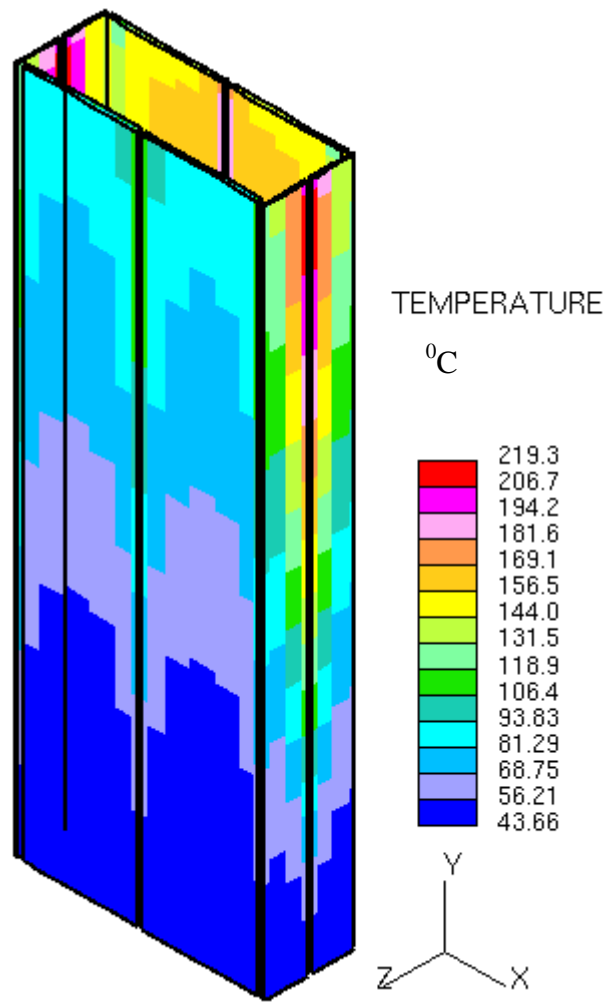


Fig. 2.46 Fluid flow temperature field in the cooling channels of rig 2, case 11.

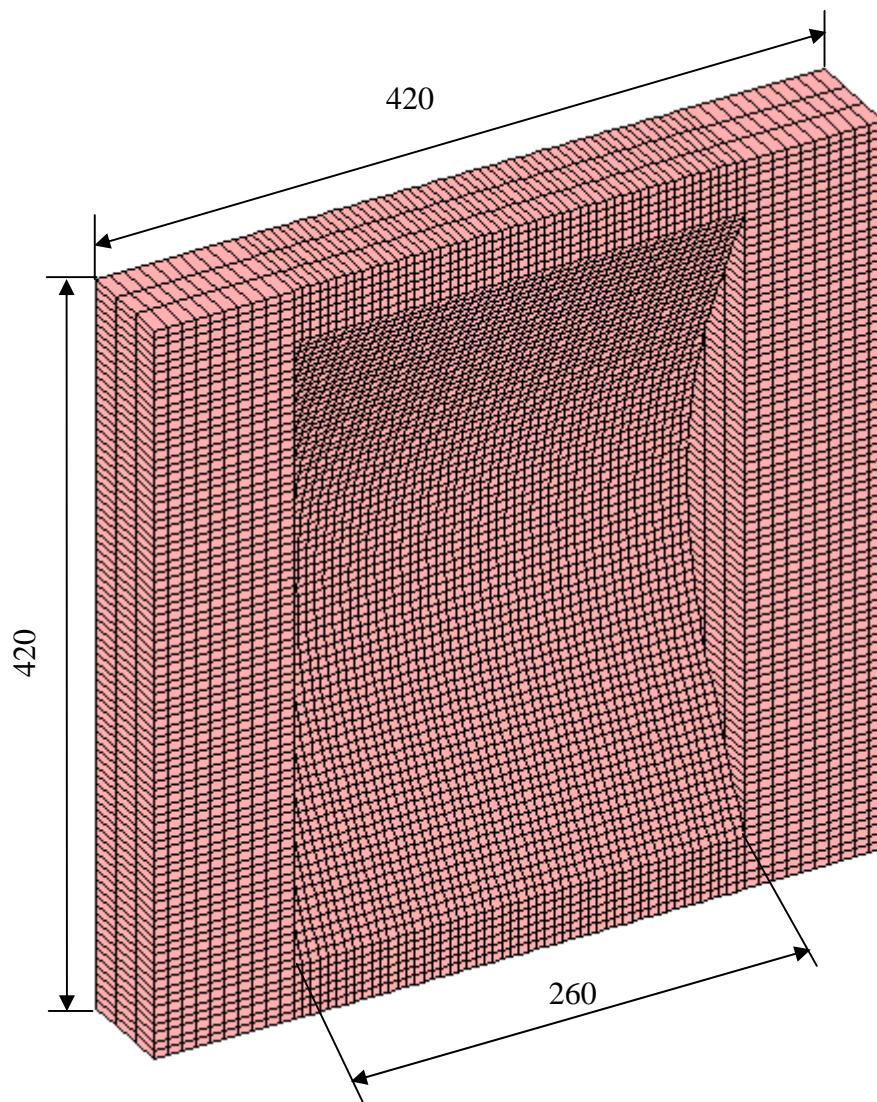


Fig. 2.47. General view of the back wall section simulated

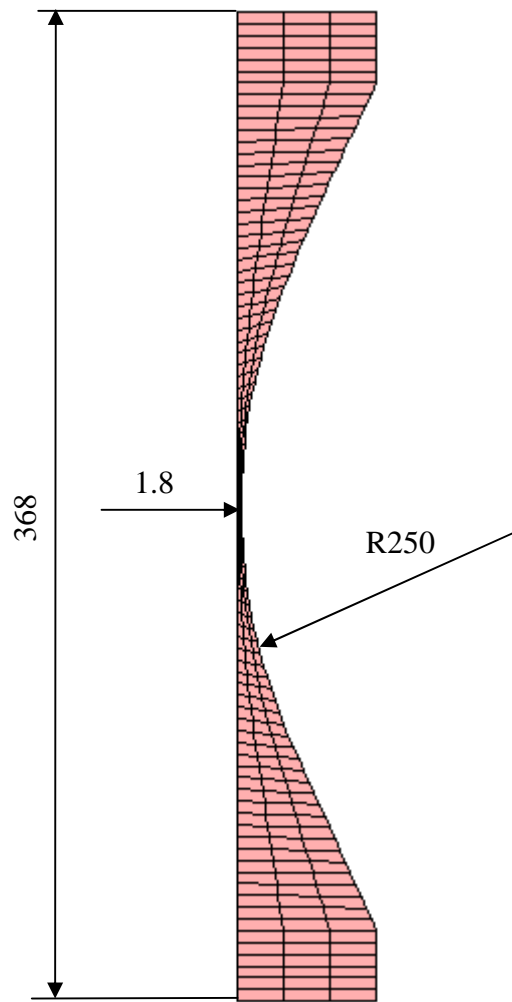


Fig. 2.48 Some dimensions of the back wall

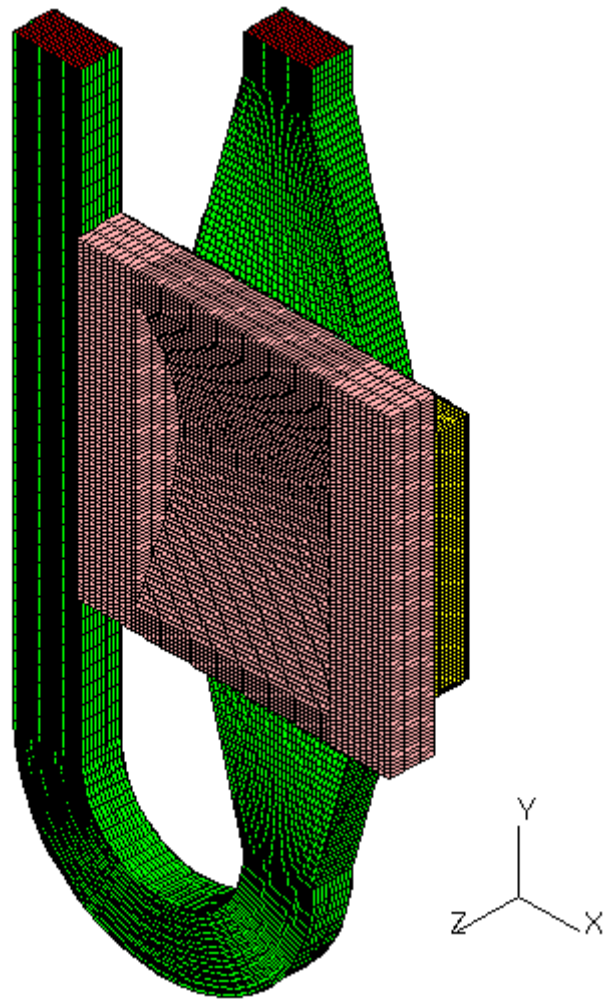


Fig. 2.49 Isometric view of the model simulated.

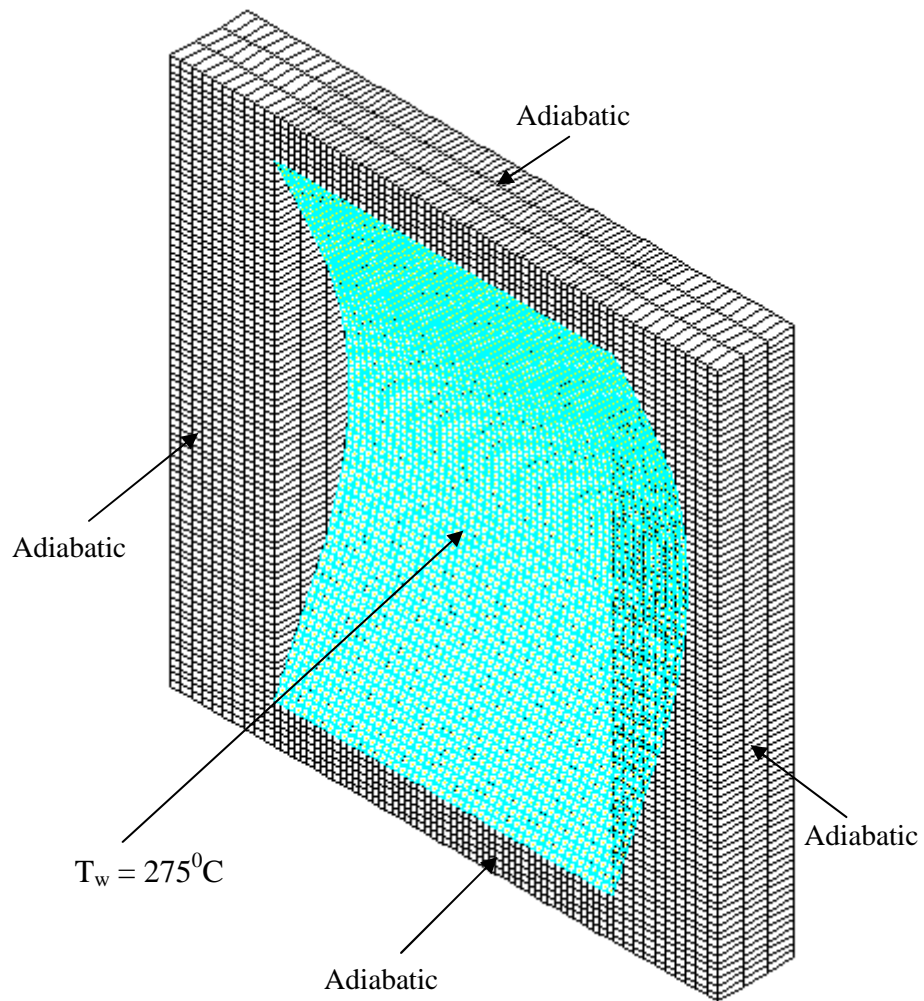
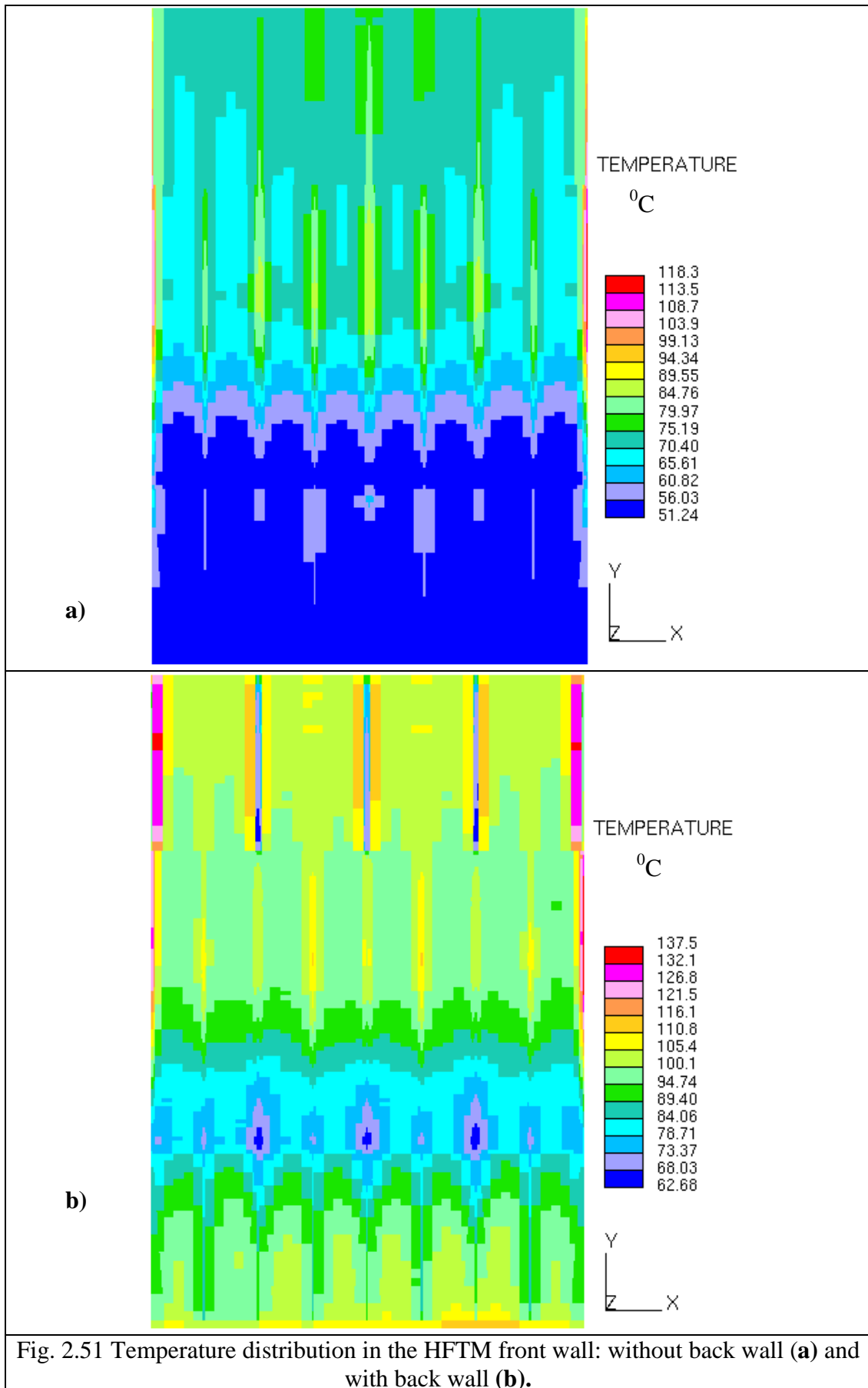
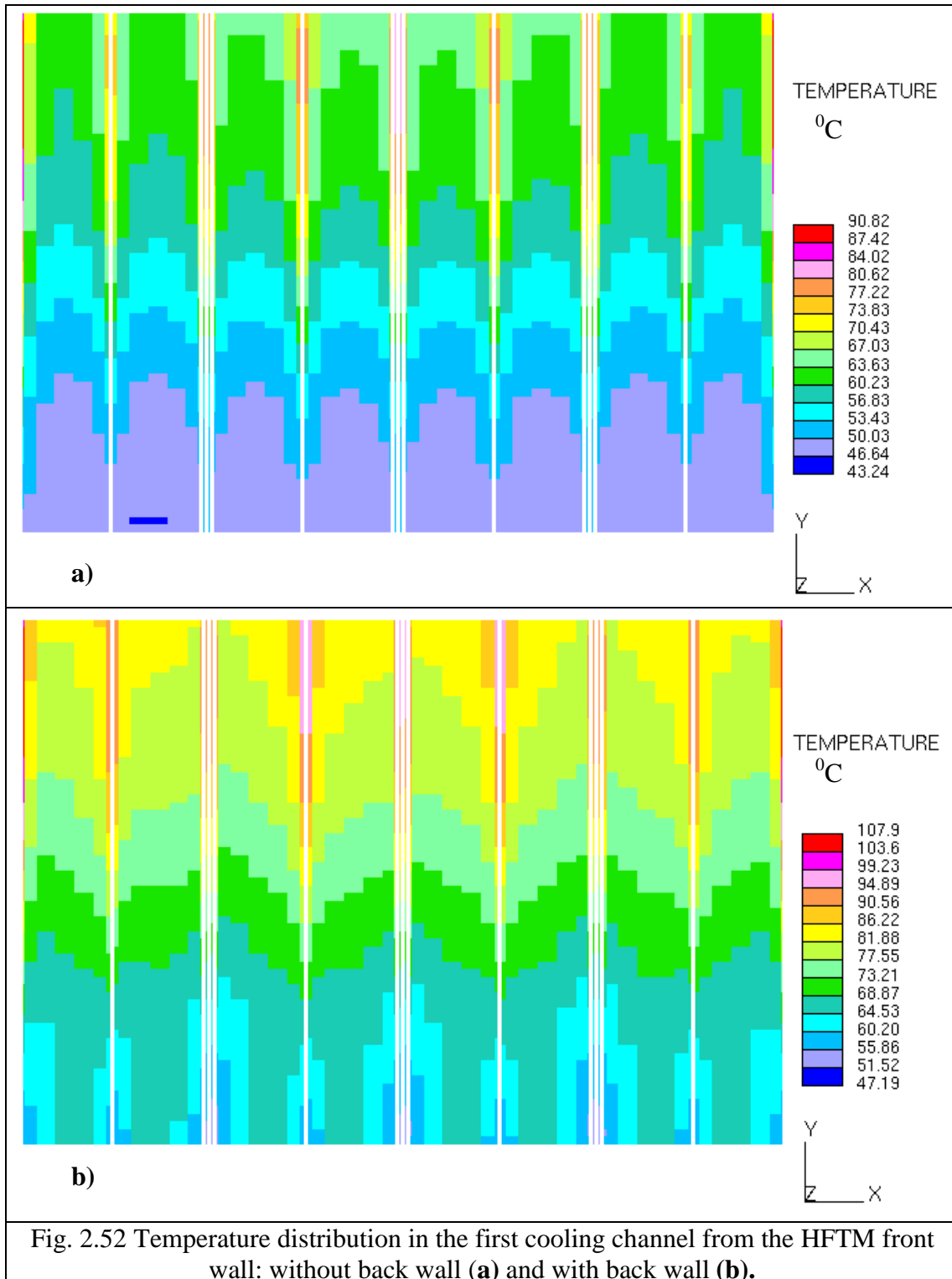


Fig. 2.50 Boundary condition on the target back wall.





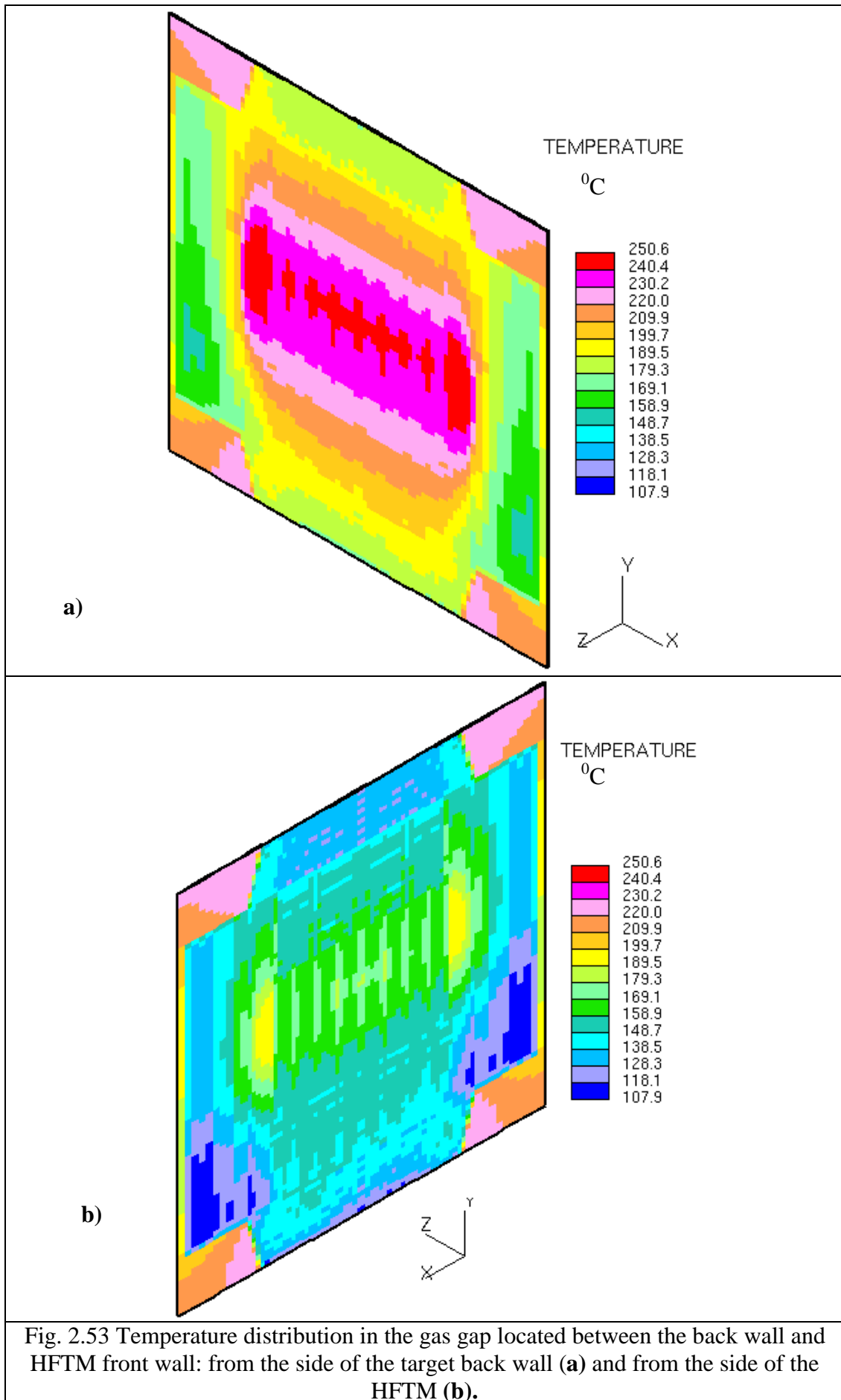


Fig. 2.53 Temperature distribution in the gas gap located between the back wall and HFTM front wall: from the side of the target back wall (a) and from the side of the HFTM (b).

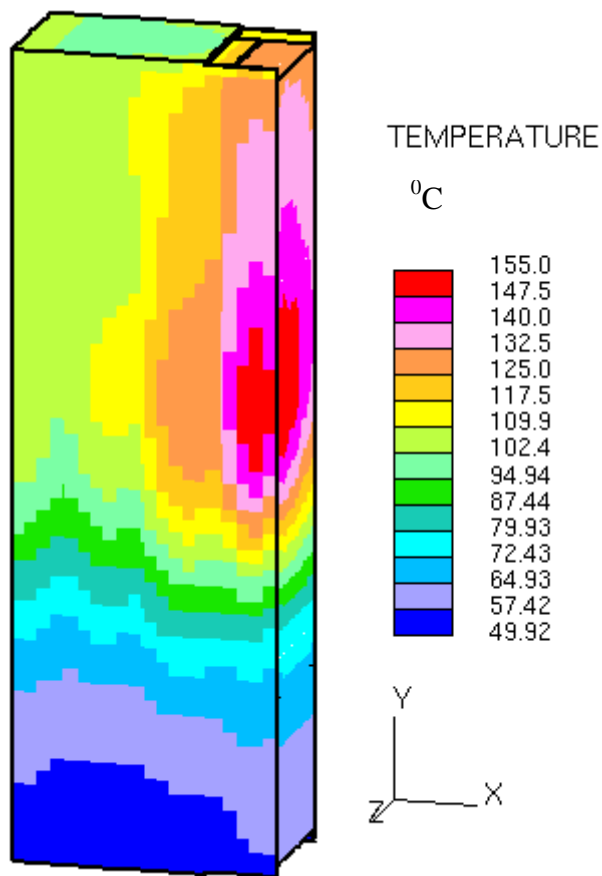


Fig. 2.54 Temperature distribution in the lateral reflector for initial location of the cooling channels at 20, 50 and 80mm from the test section.

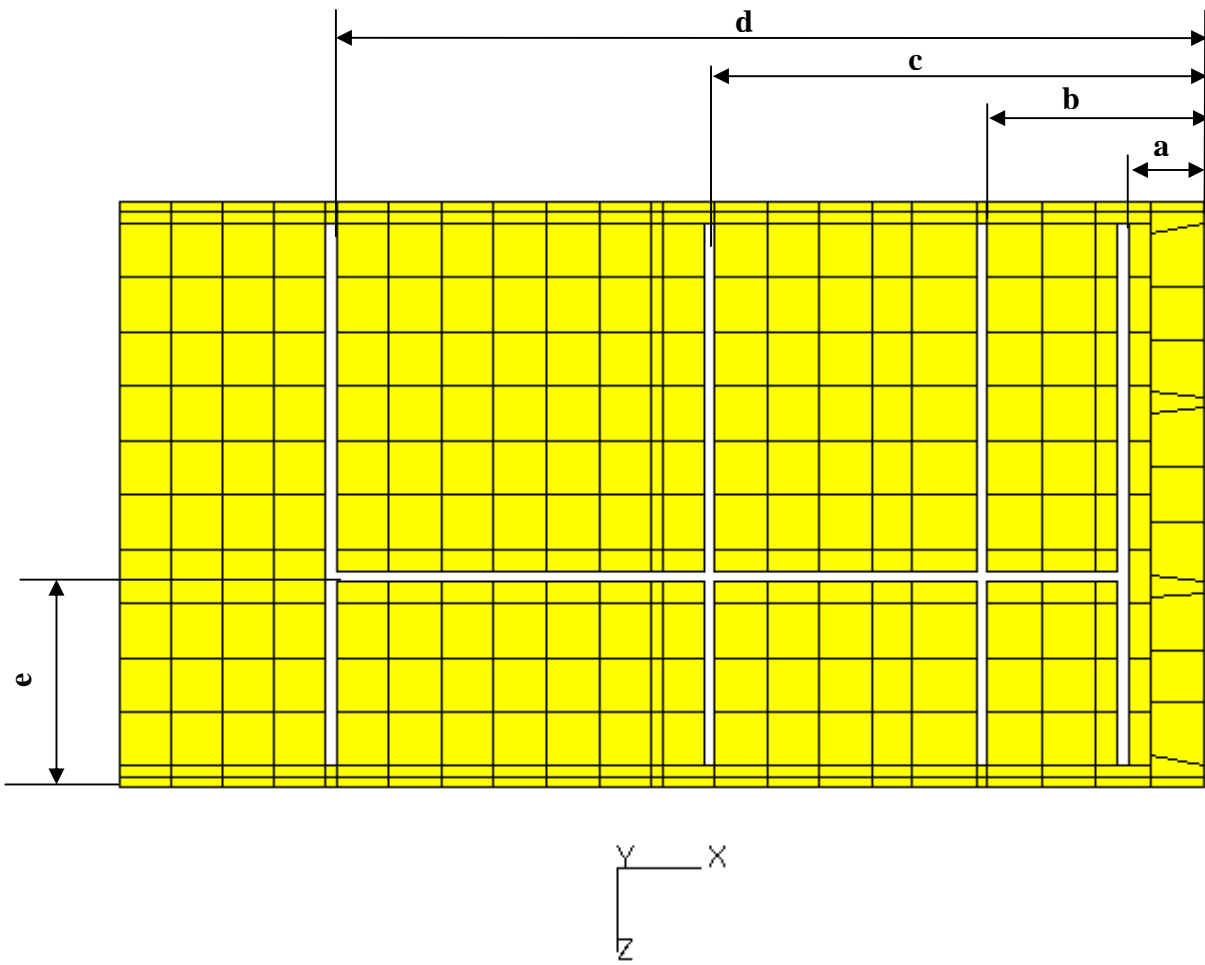


Fig. 2.55 Modified cooling system of the lateral reflector.

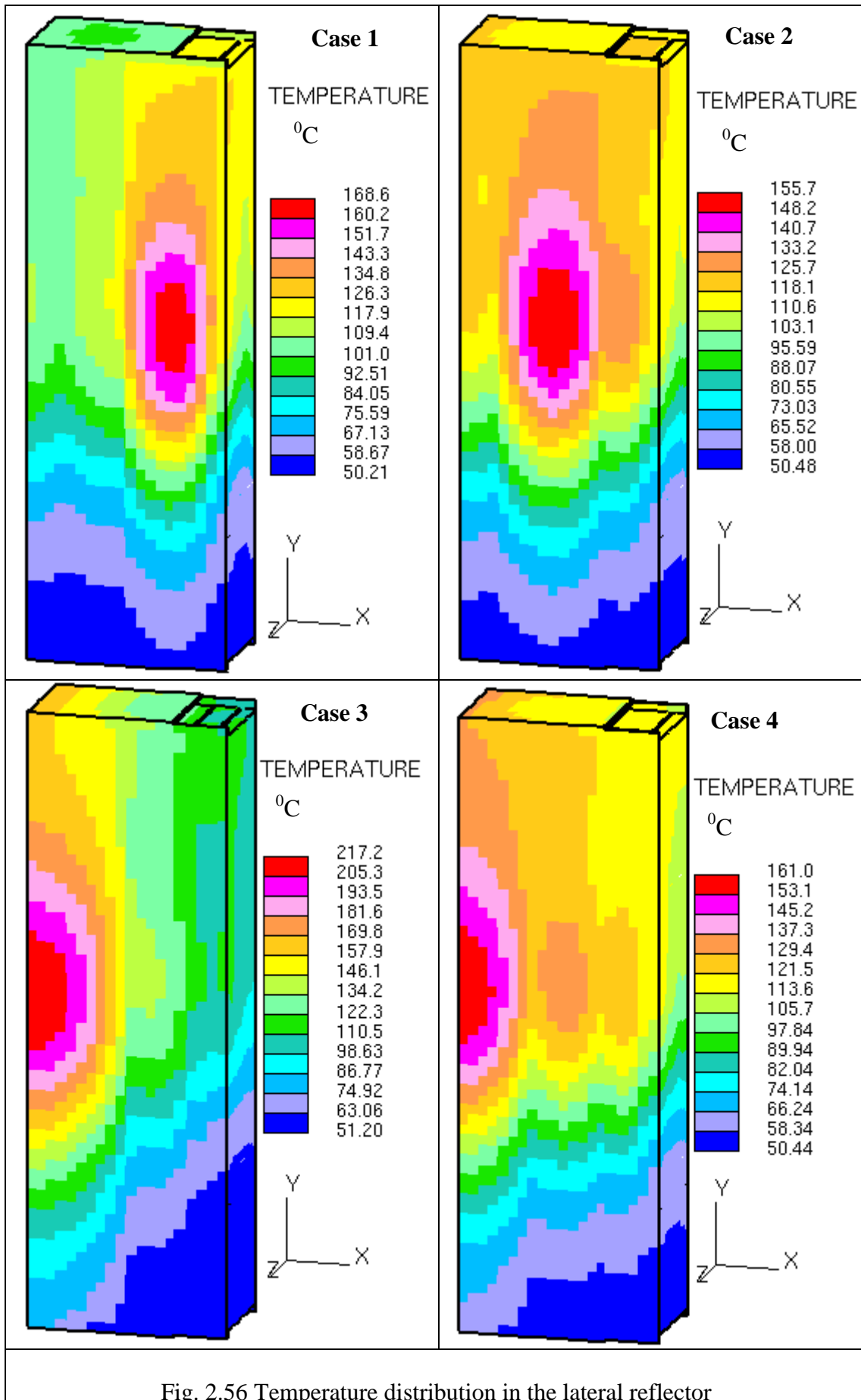


Fig. 2.56 Temperature distribution in the lateral reflector

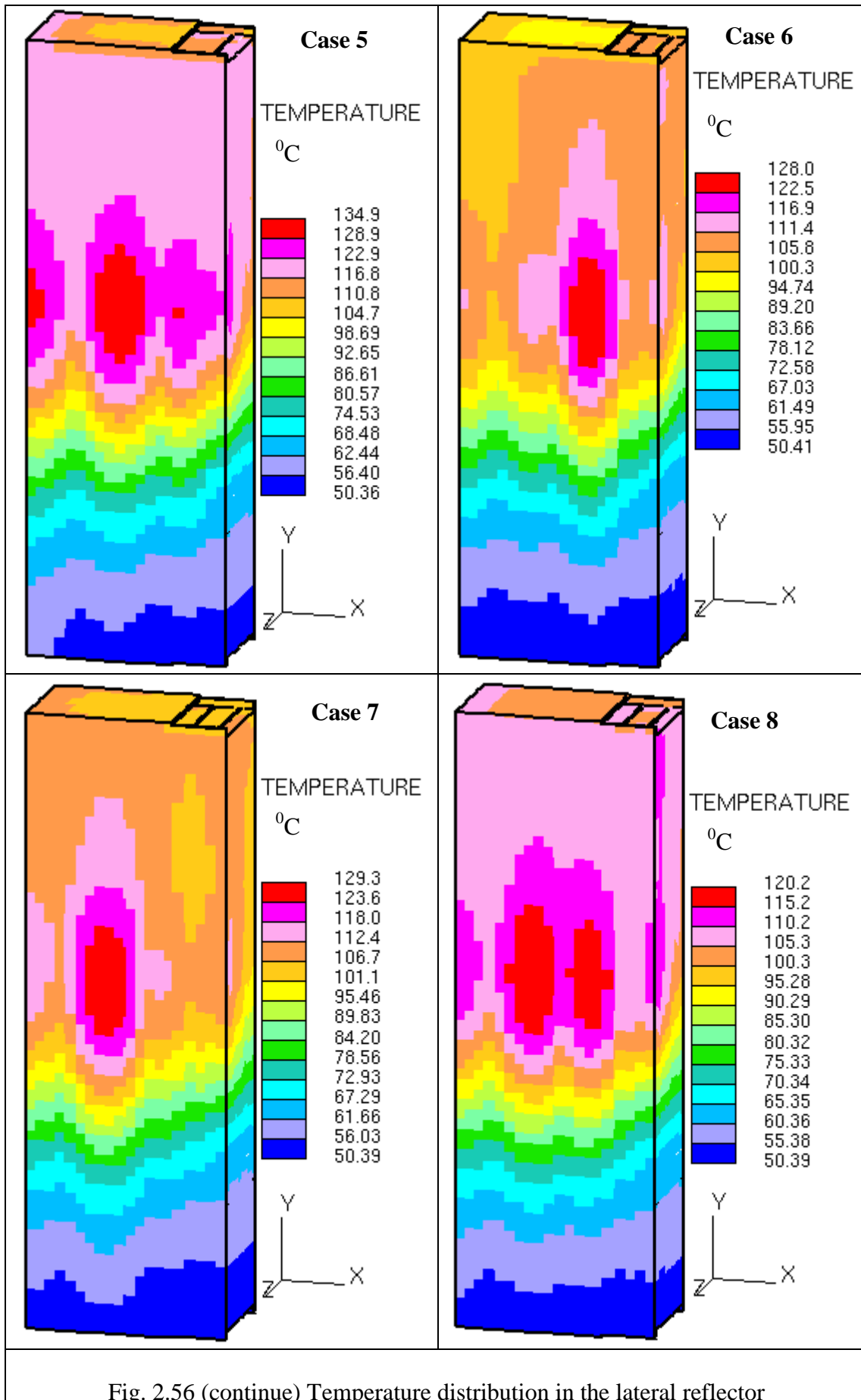


Fig. 2.56 (continue) Temperature distribution in the lateral reflector

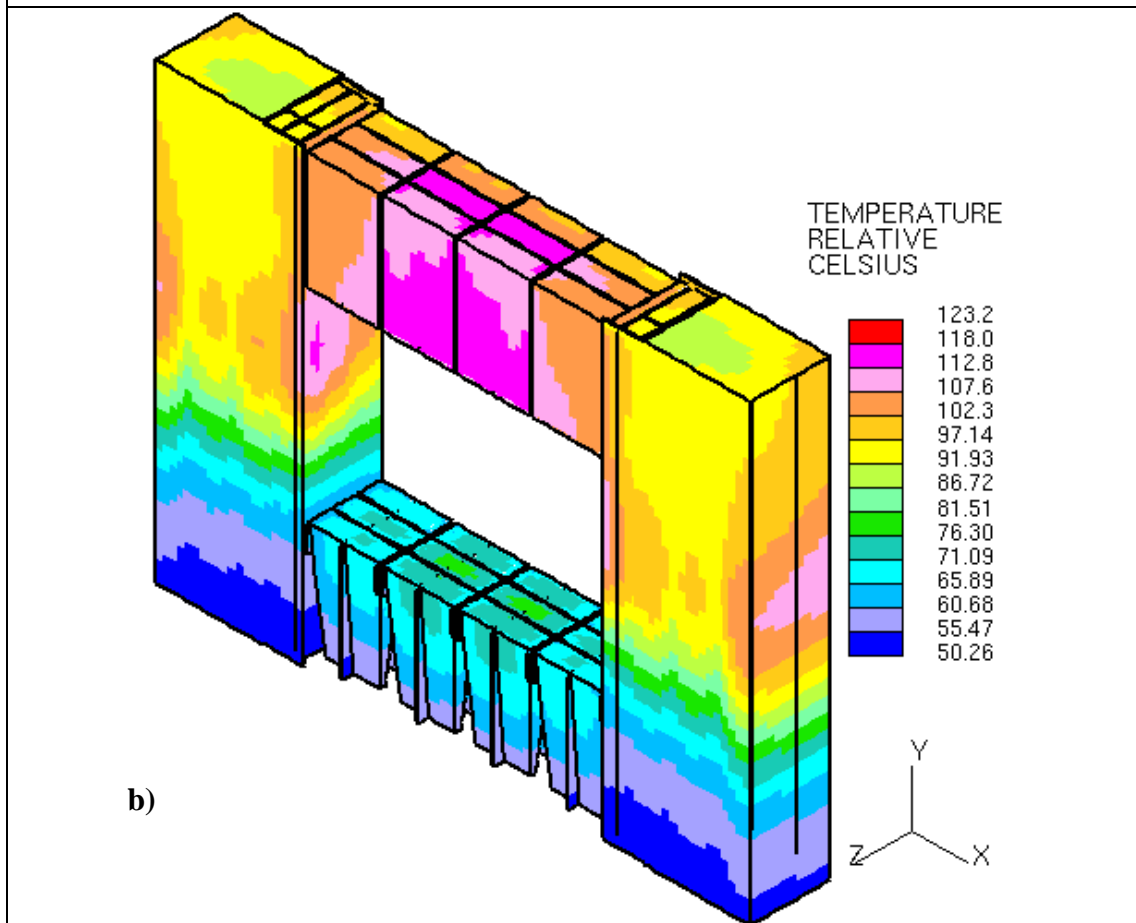
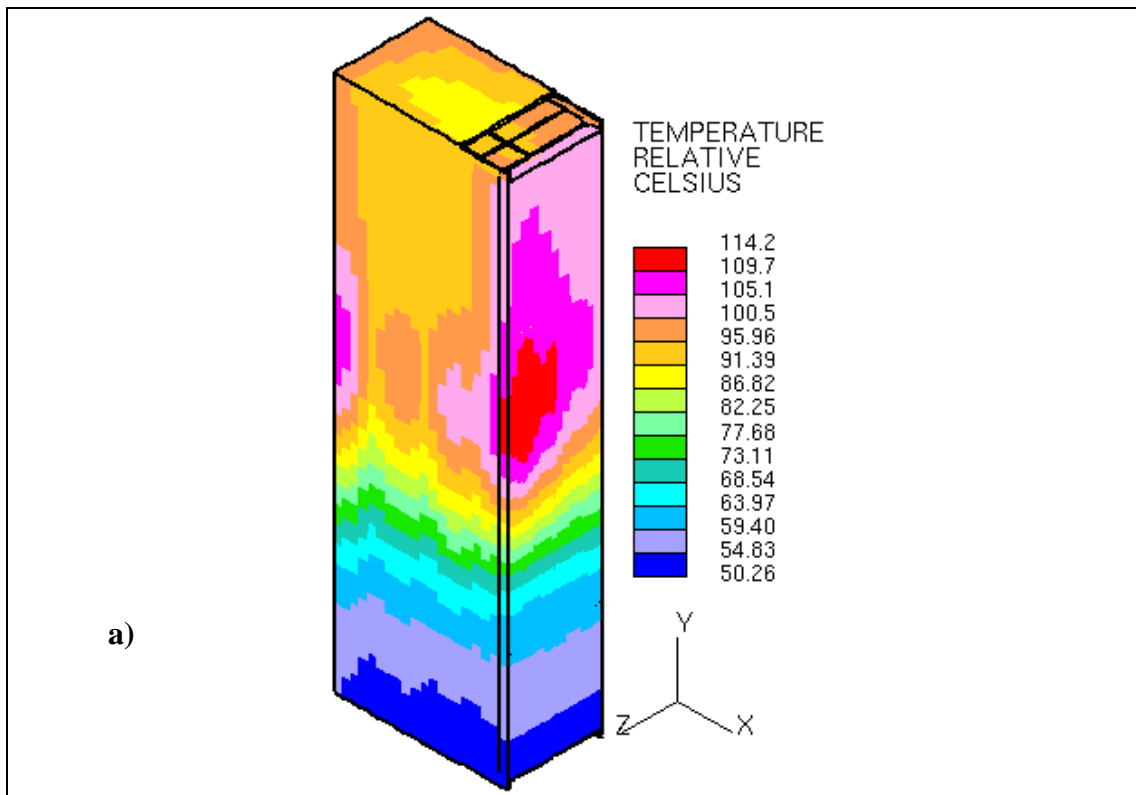


Fig. 2.57 Temperature distribution in the lateral (a) and in all the reflector (b) for case 8m.

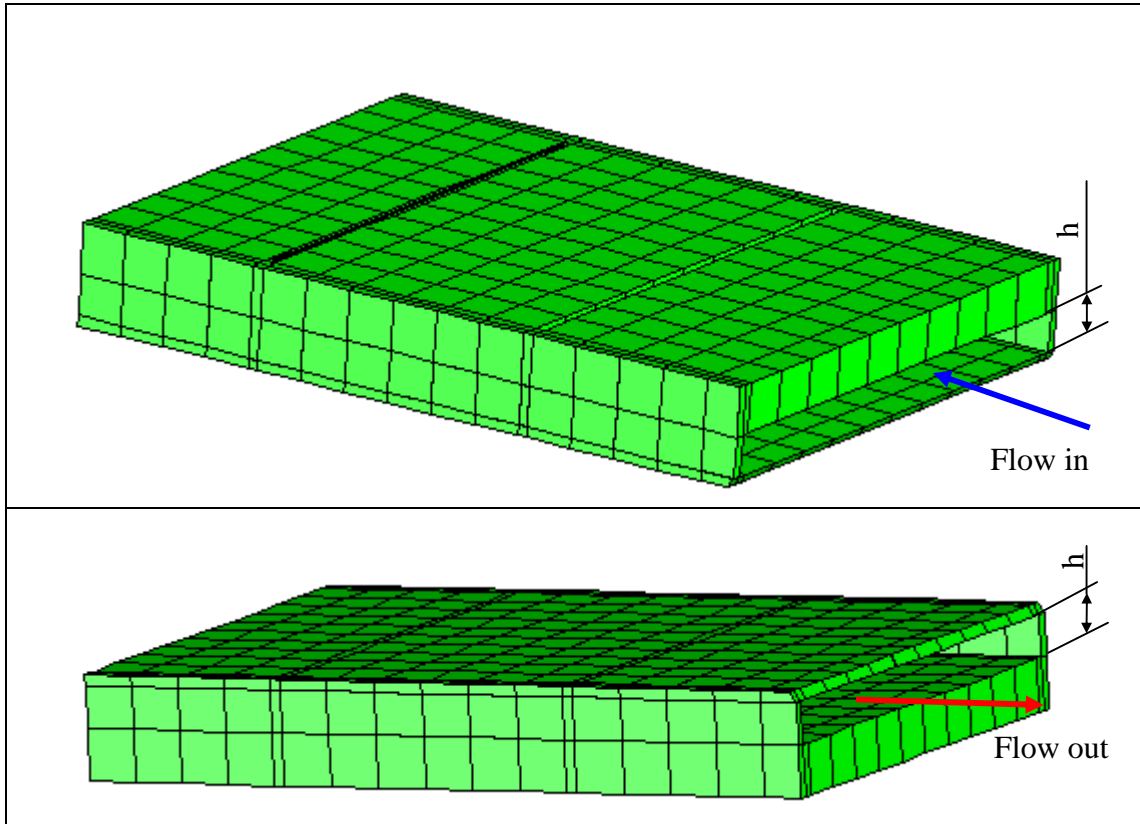


Fig. 2.58. Bypass flow supply and remove gap for the lateral reflector cooling system.

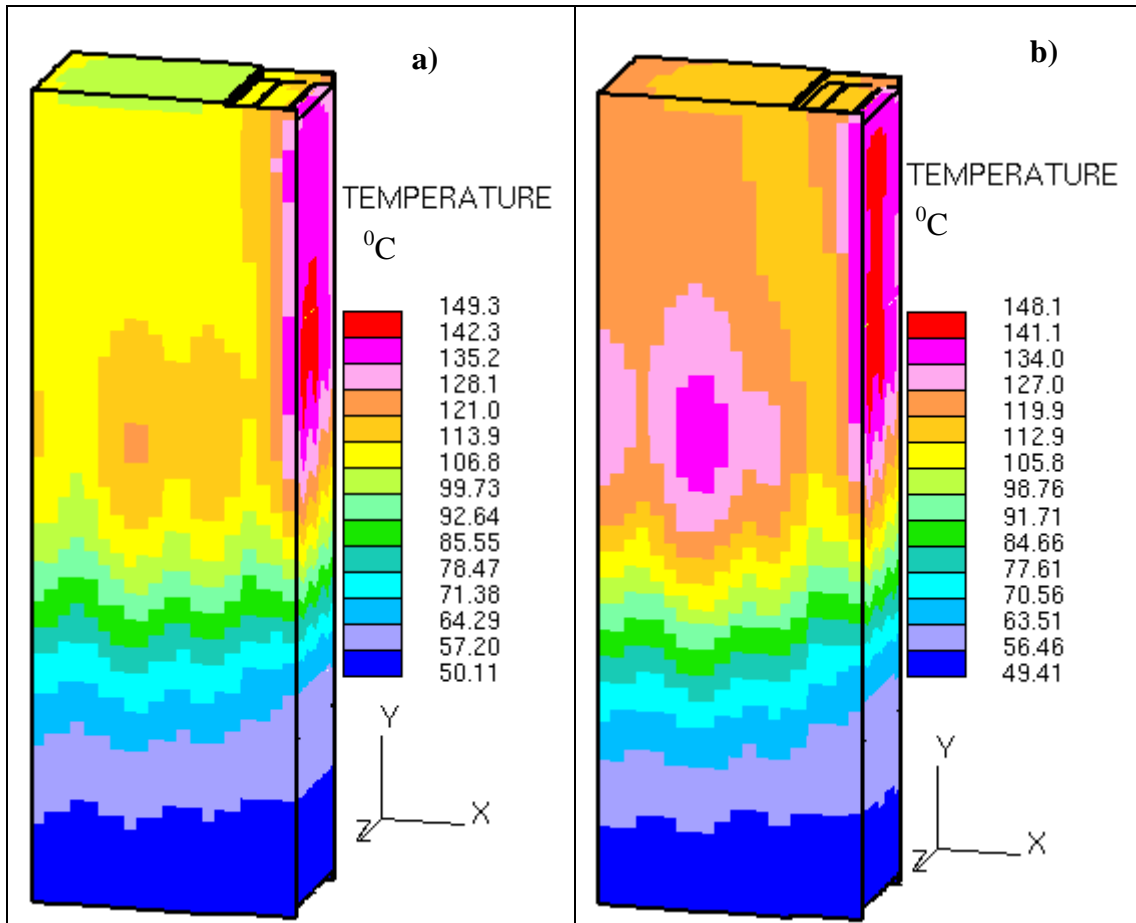


Fig. 2.59 Temperature distribution in the lateral reflector under nuclear and electrical heating, **a** –  $h = 2\text{mm}$ , **b** –  $h = 1\text{ mm}$  ( $h$  – see Fig. 2.58)

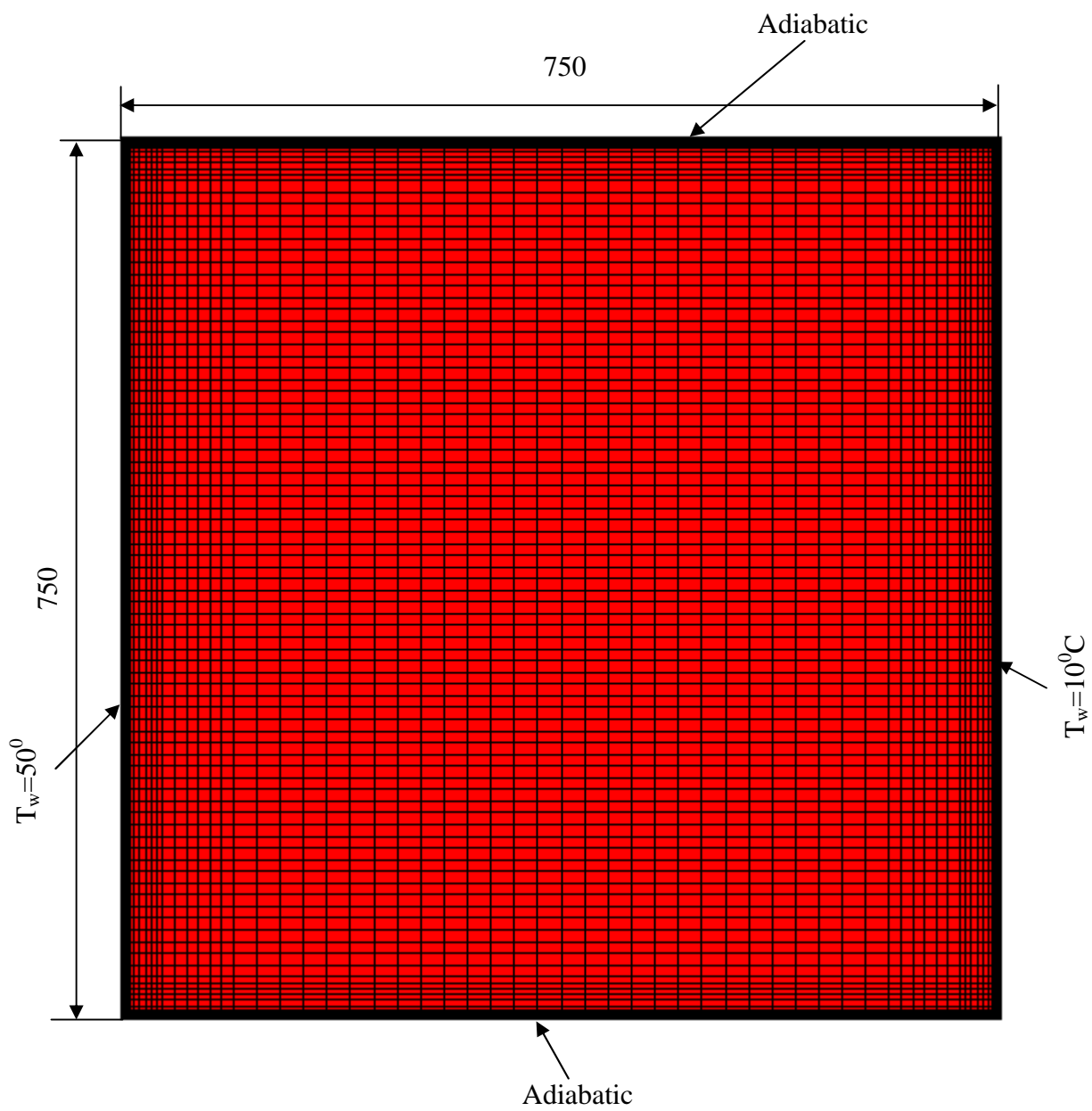


Fig. 3.1 Natural convection simulation: model simulated and boundary conditions.

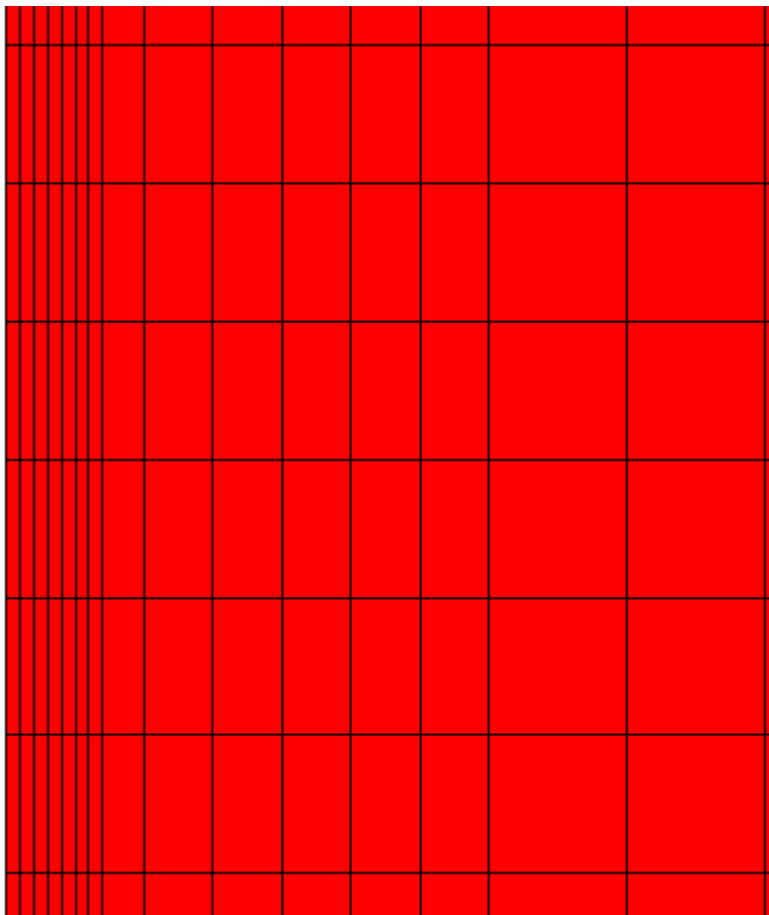
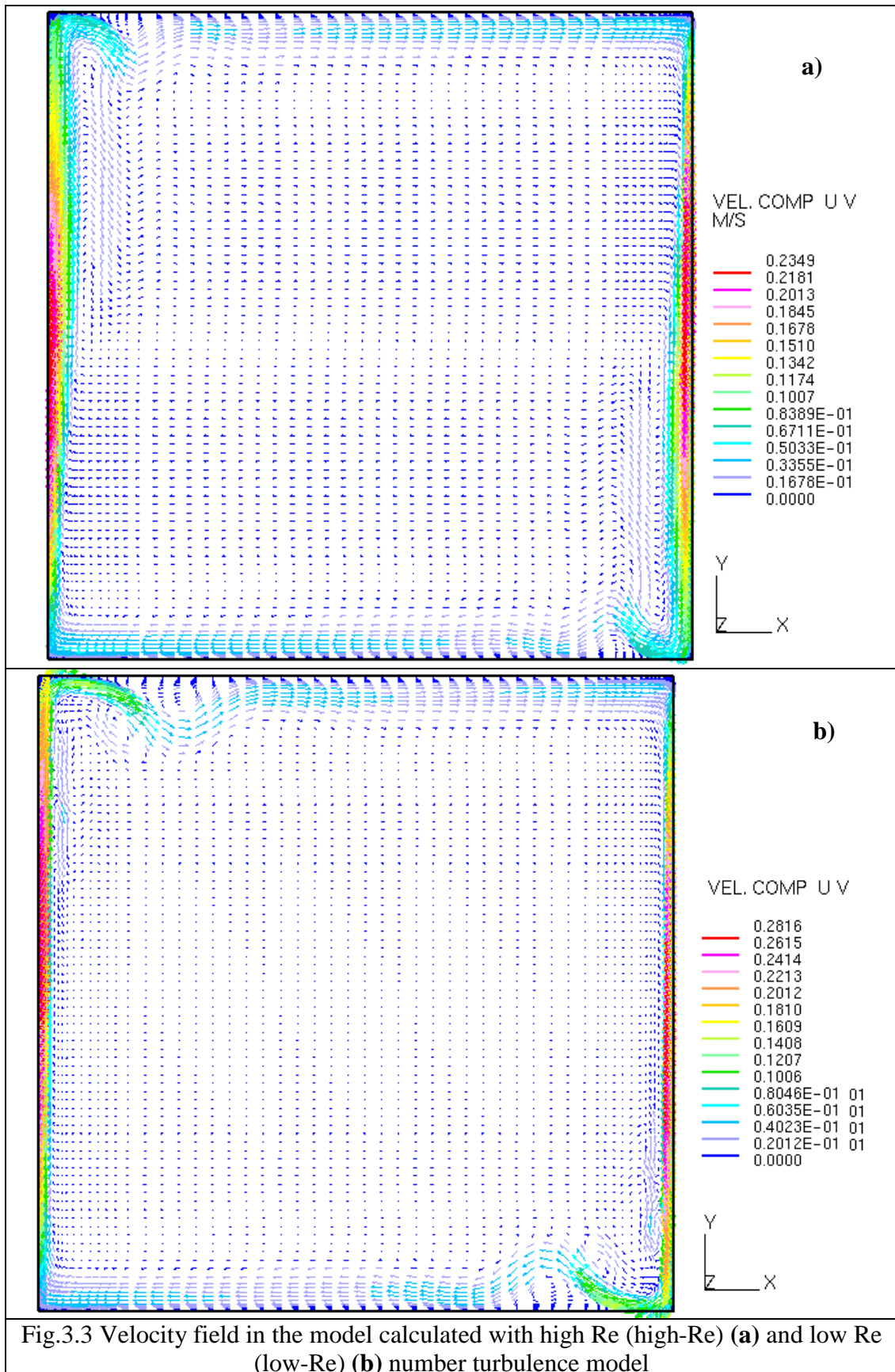
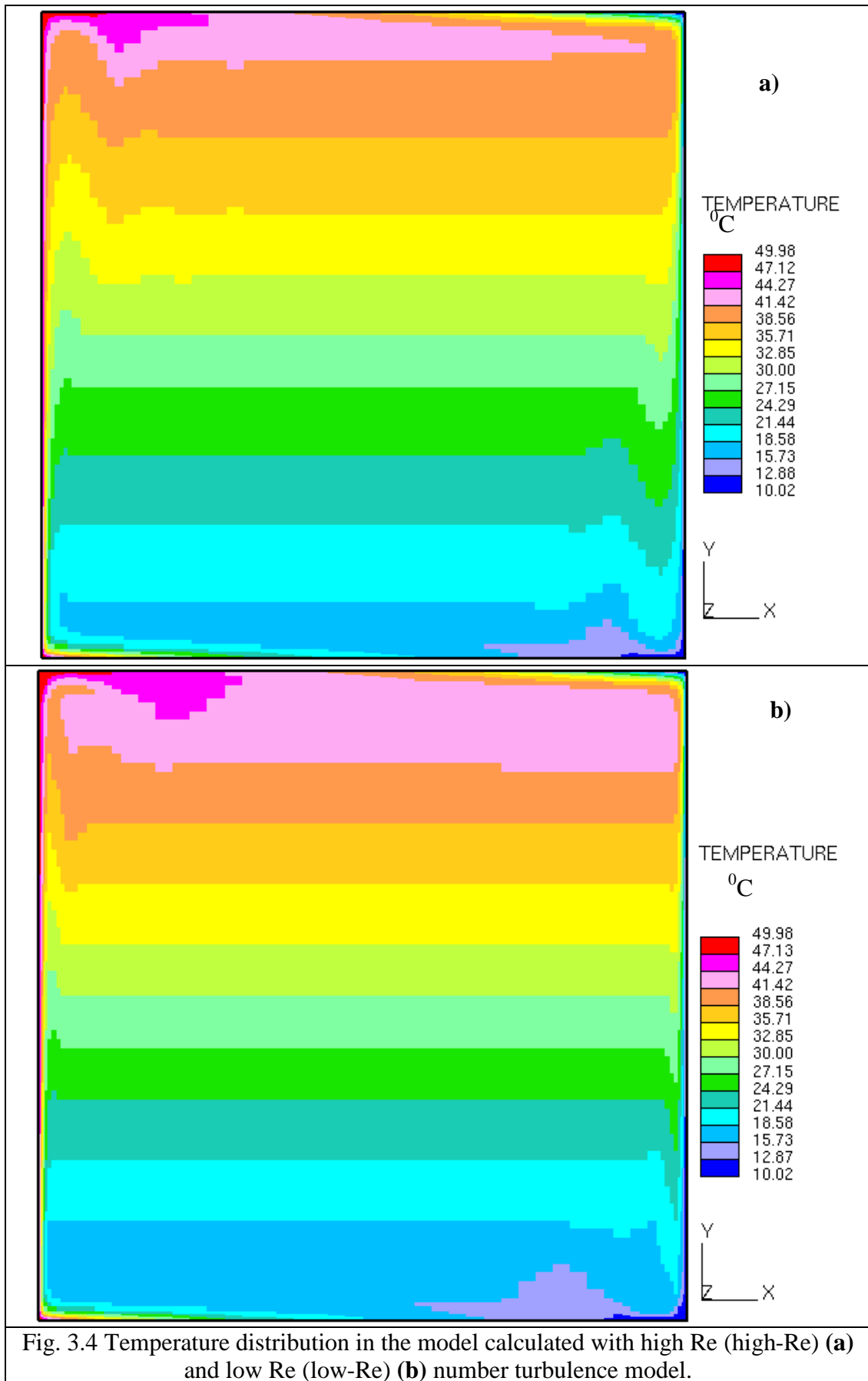


Fig. 3.2 Mesh of the calculation domain near the wall.





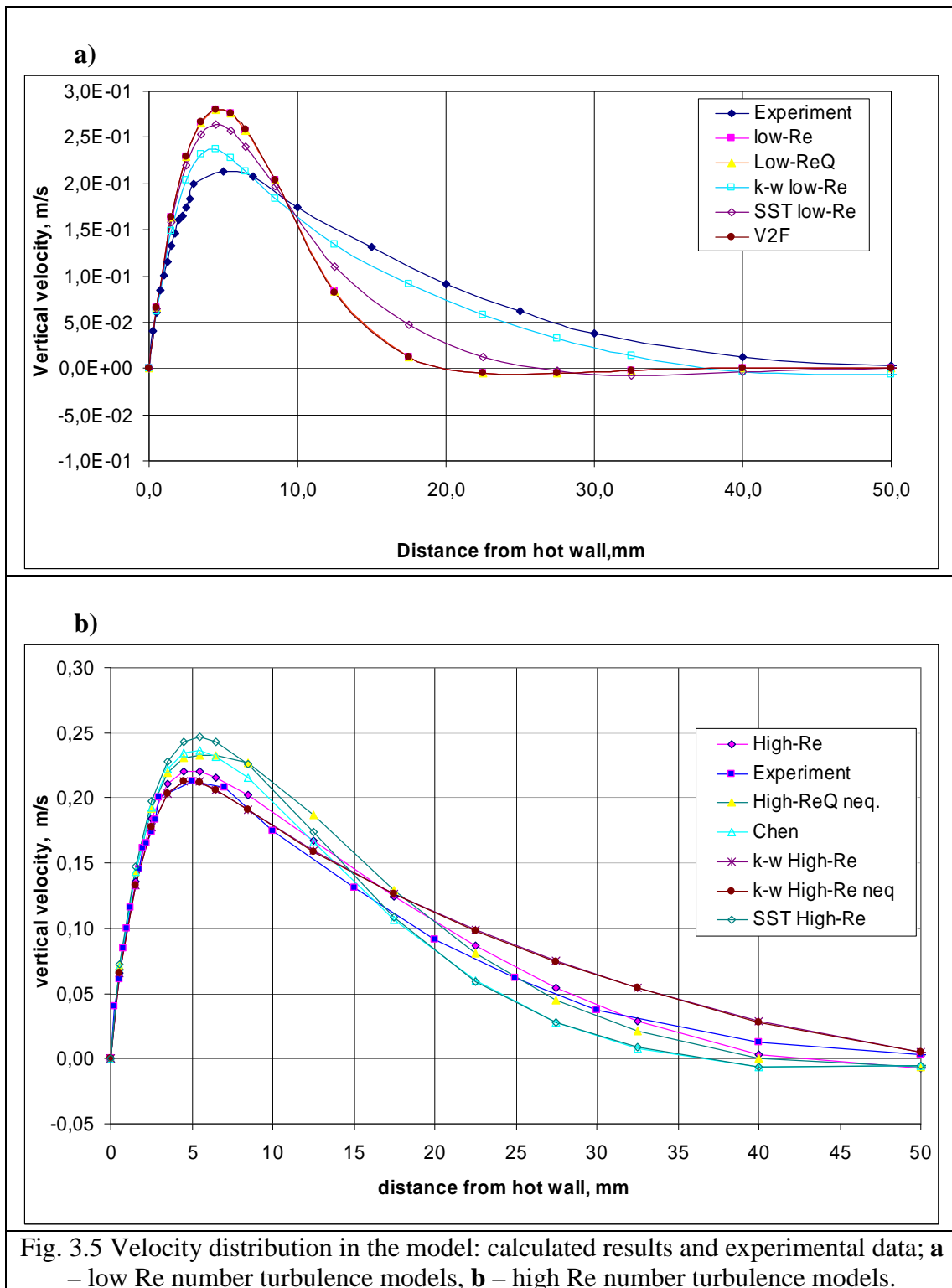
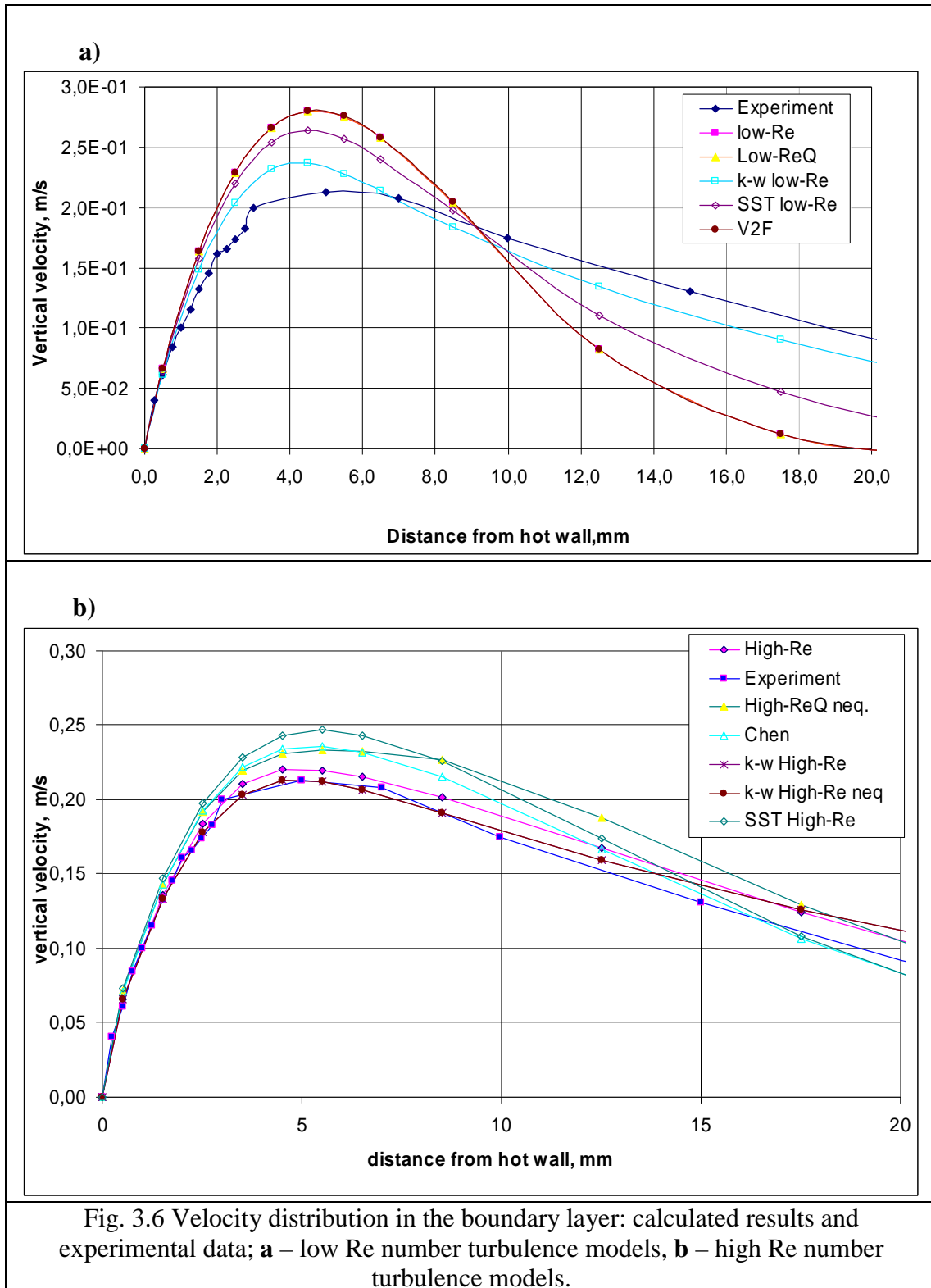
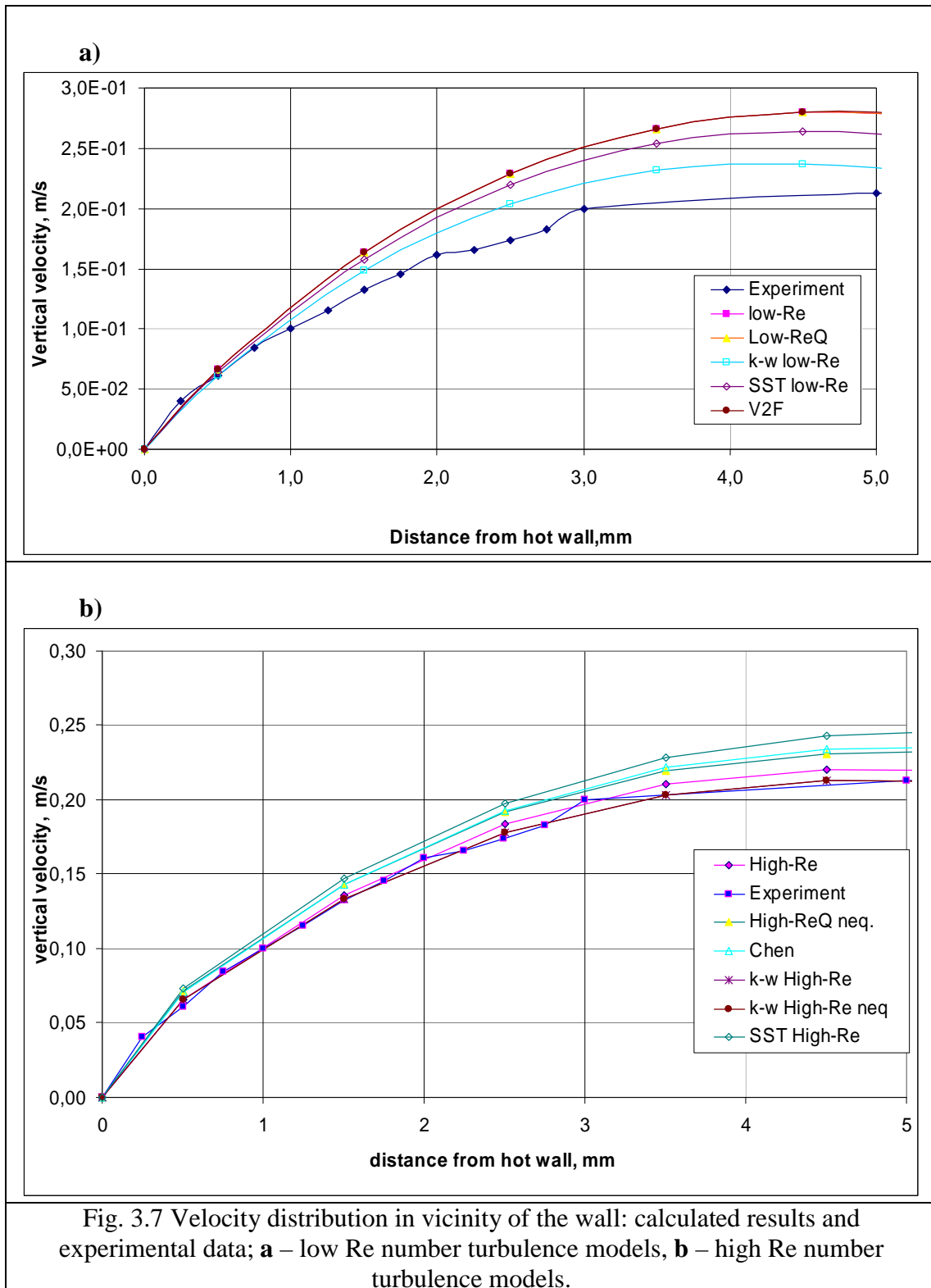


Fig. 3.5 Velocity distribution in the model: calculated results and experimental data; **a** – low Re number turbulence models, **b** – high Re number turbulence models.





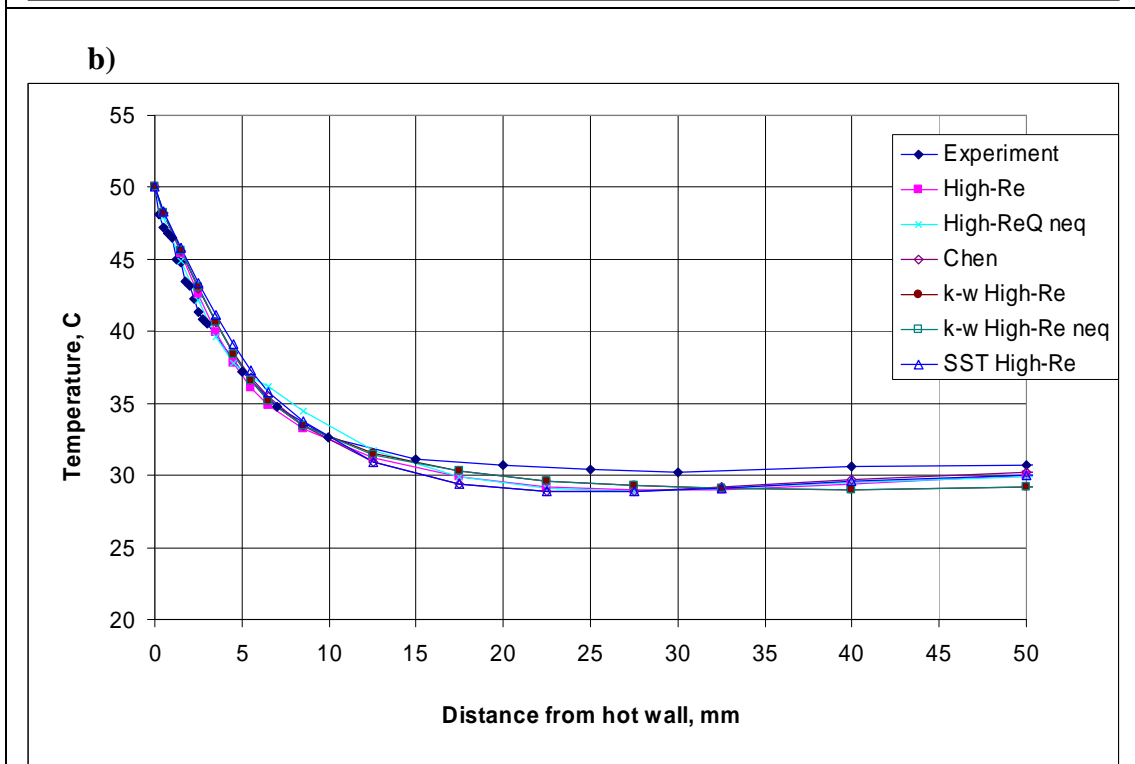
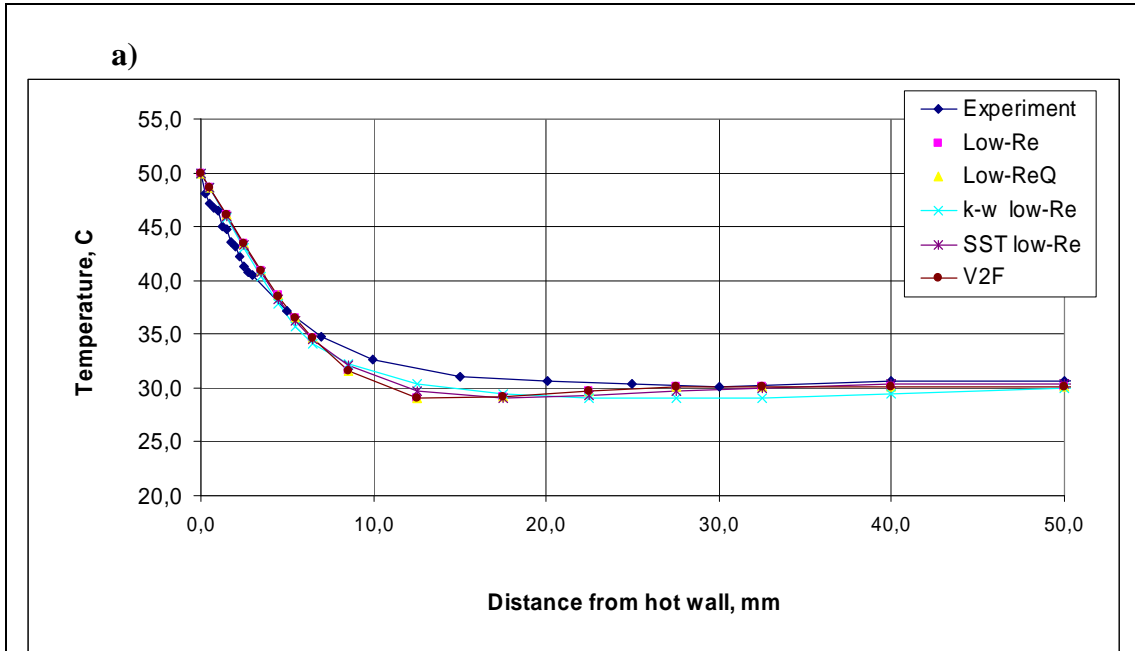
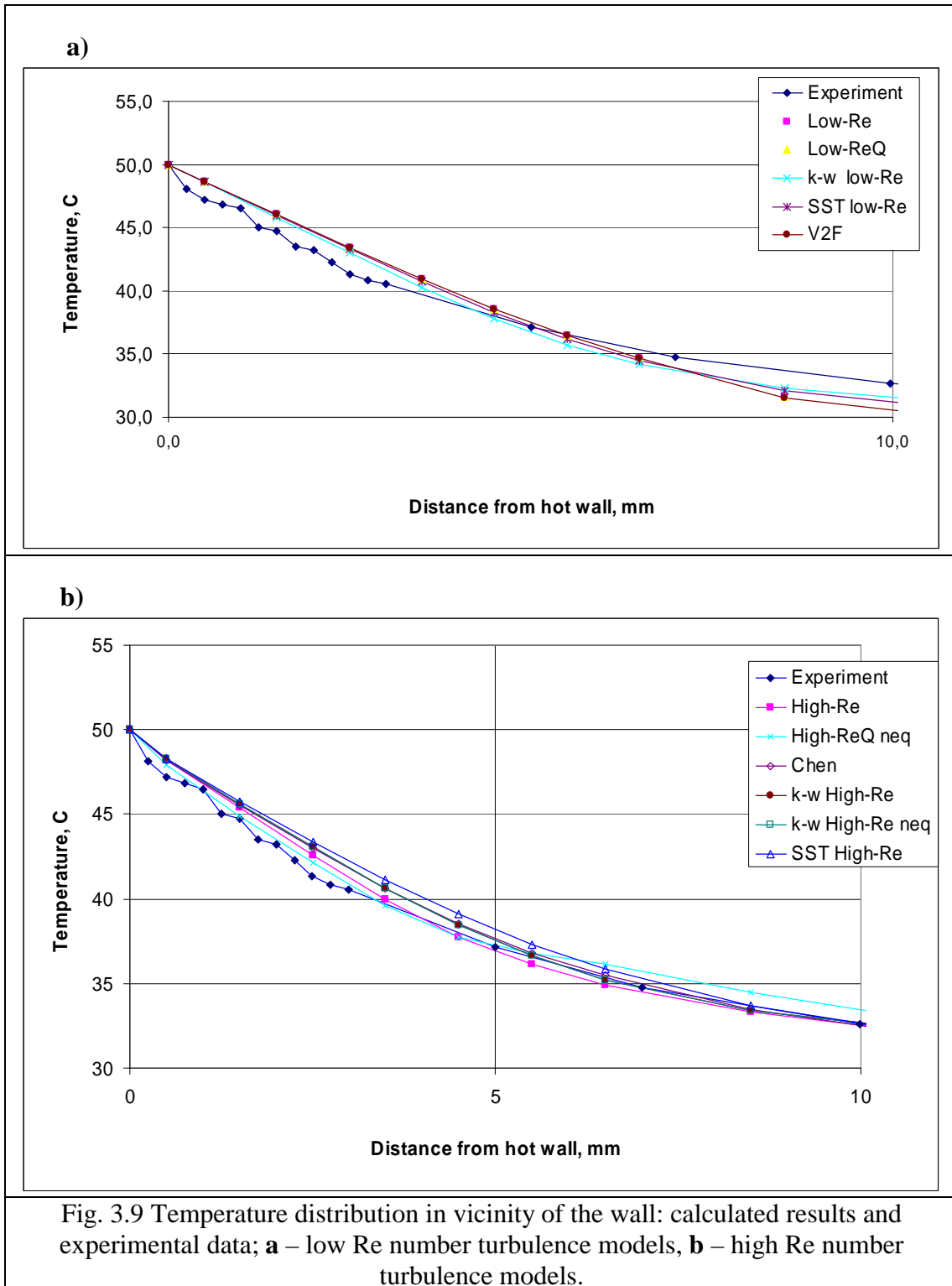
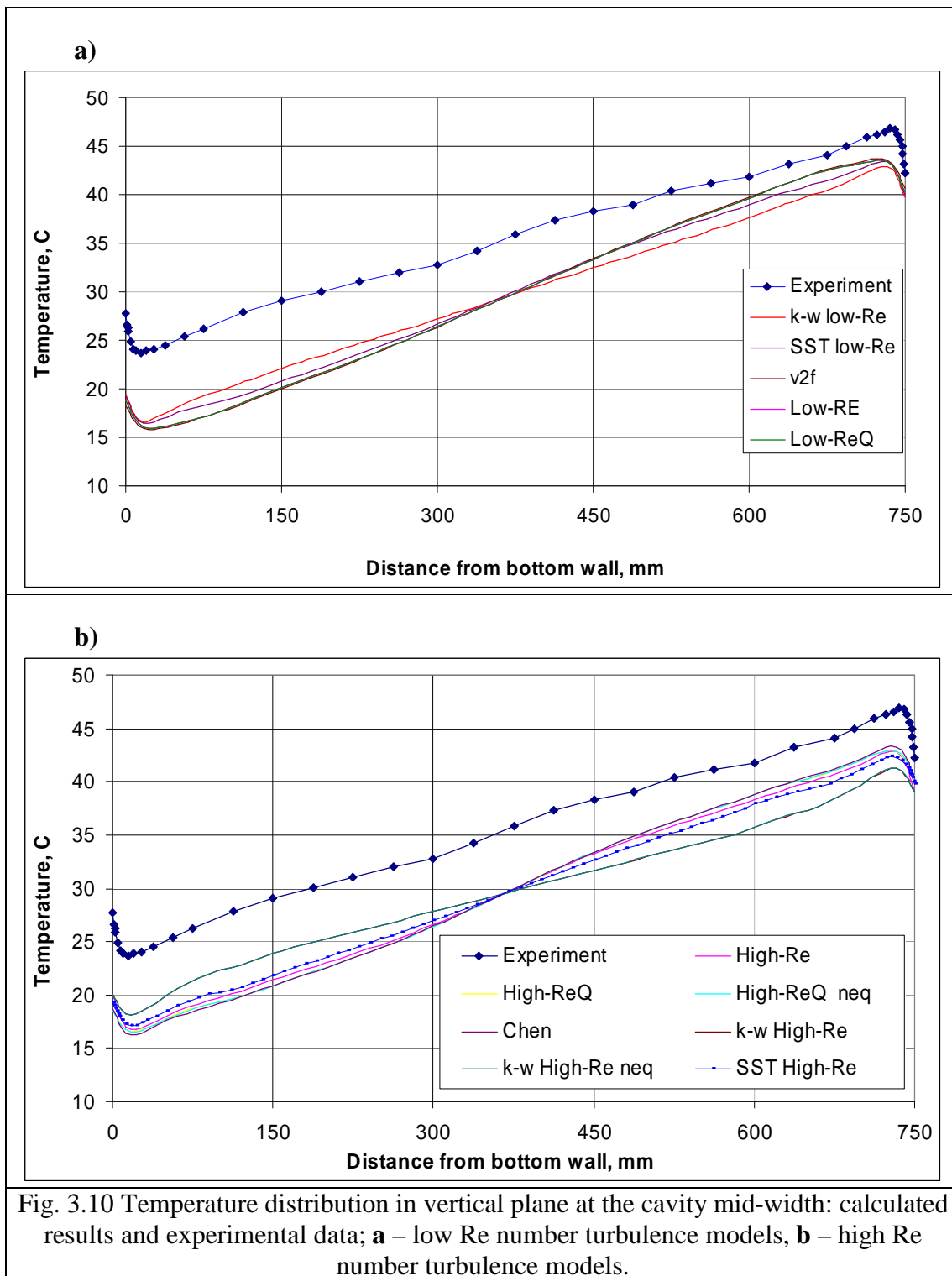


Fig. 3.8 Temperature distribution in the model: calculated results and experimental data; **a** – low Re number turbulence models, **b** – high Re number turbulence models.





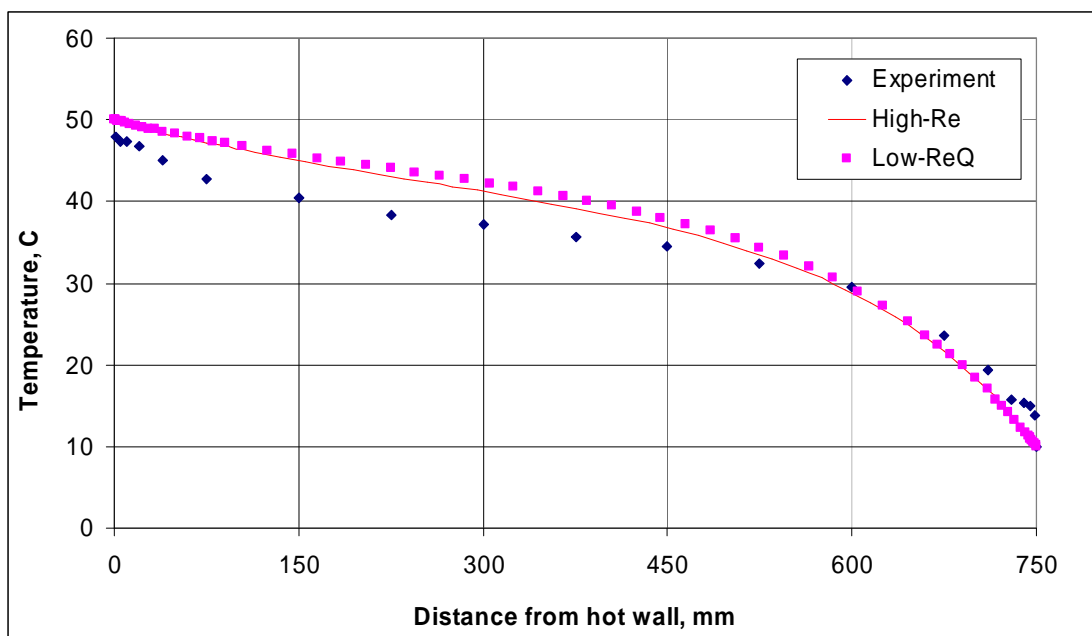


Fig. 3.11 Temperature distribution along the top wall

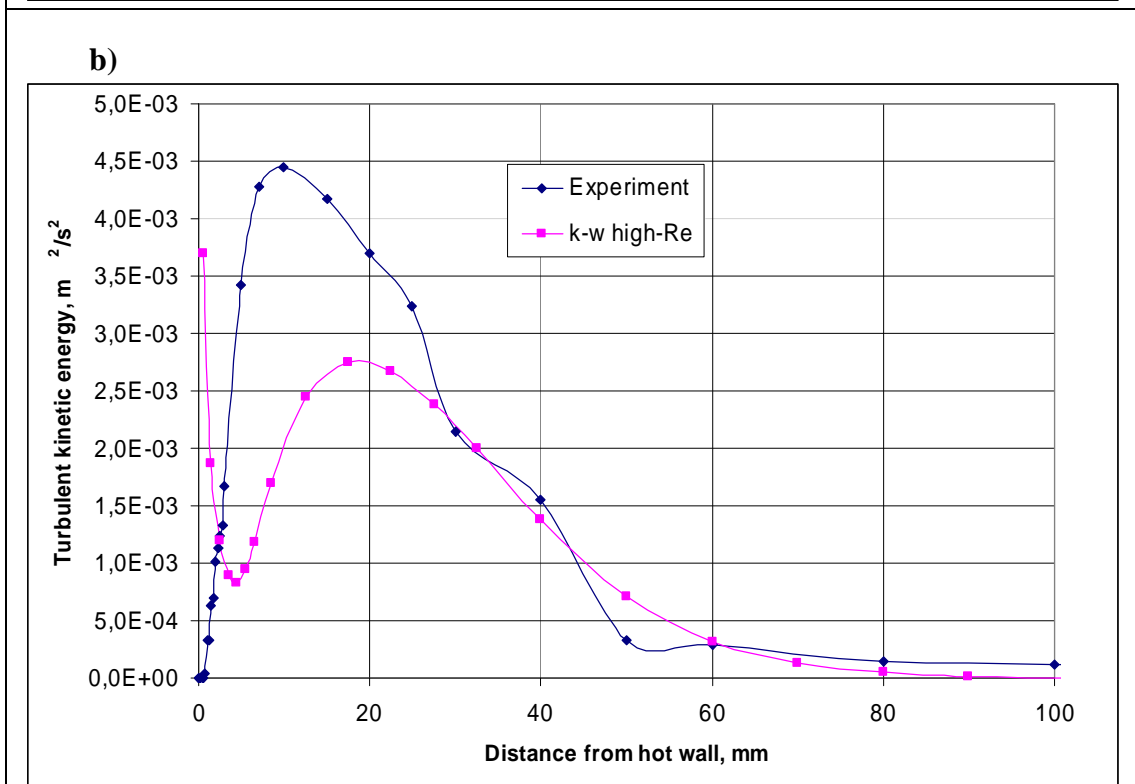
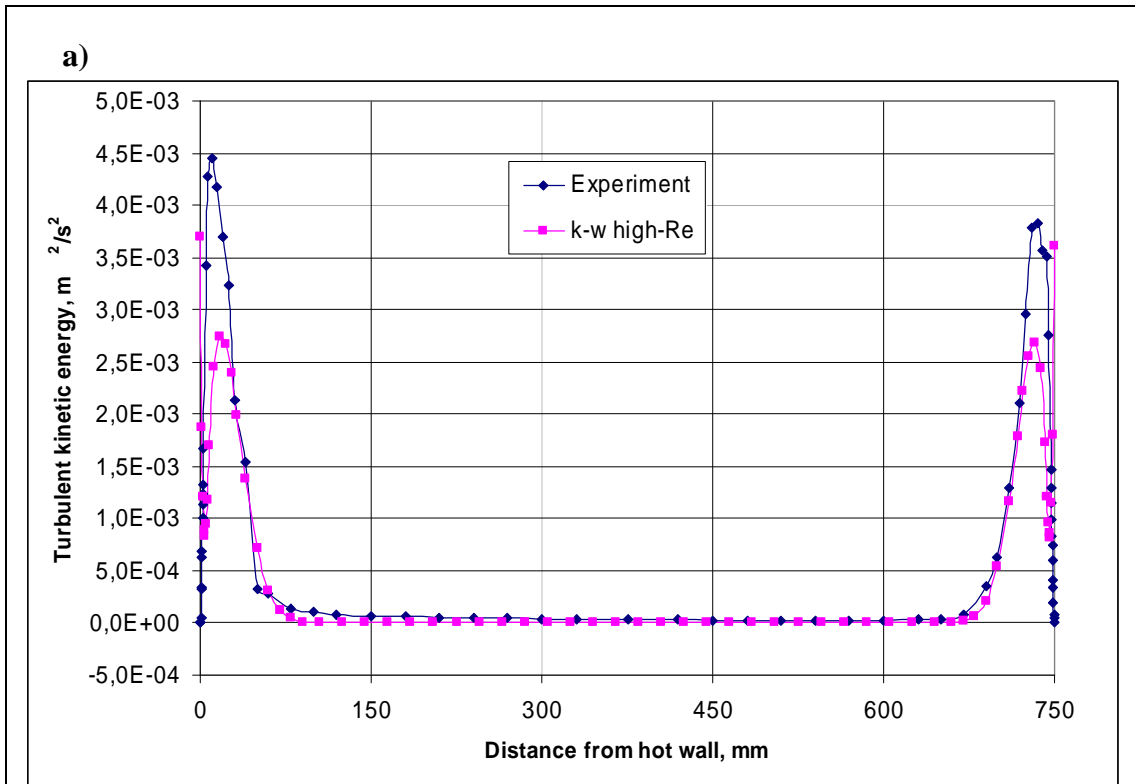


Fig. 3.12 Turbulent kinetic energy distribution in the model (a) and near the wall region (b) at the cavity mid-height.

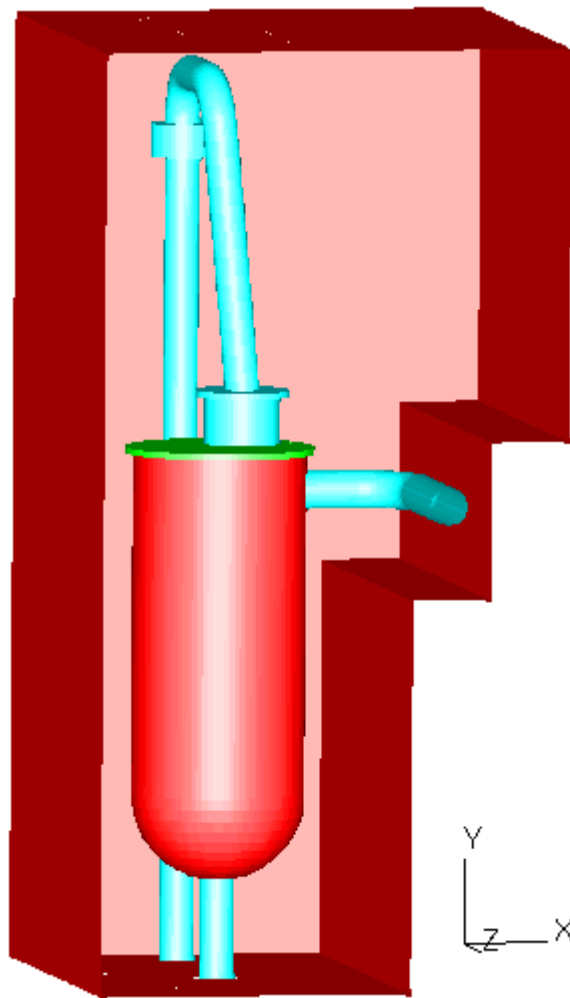


Fig. 3.13 General view of the model for simulation of the natural convection in test cell cavity.

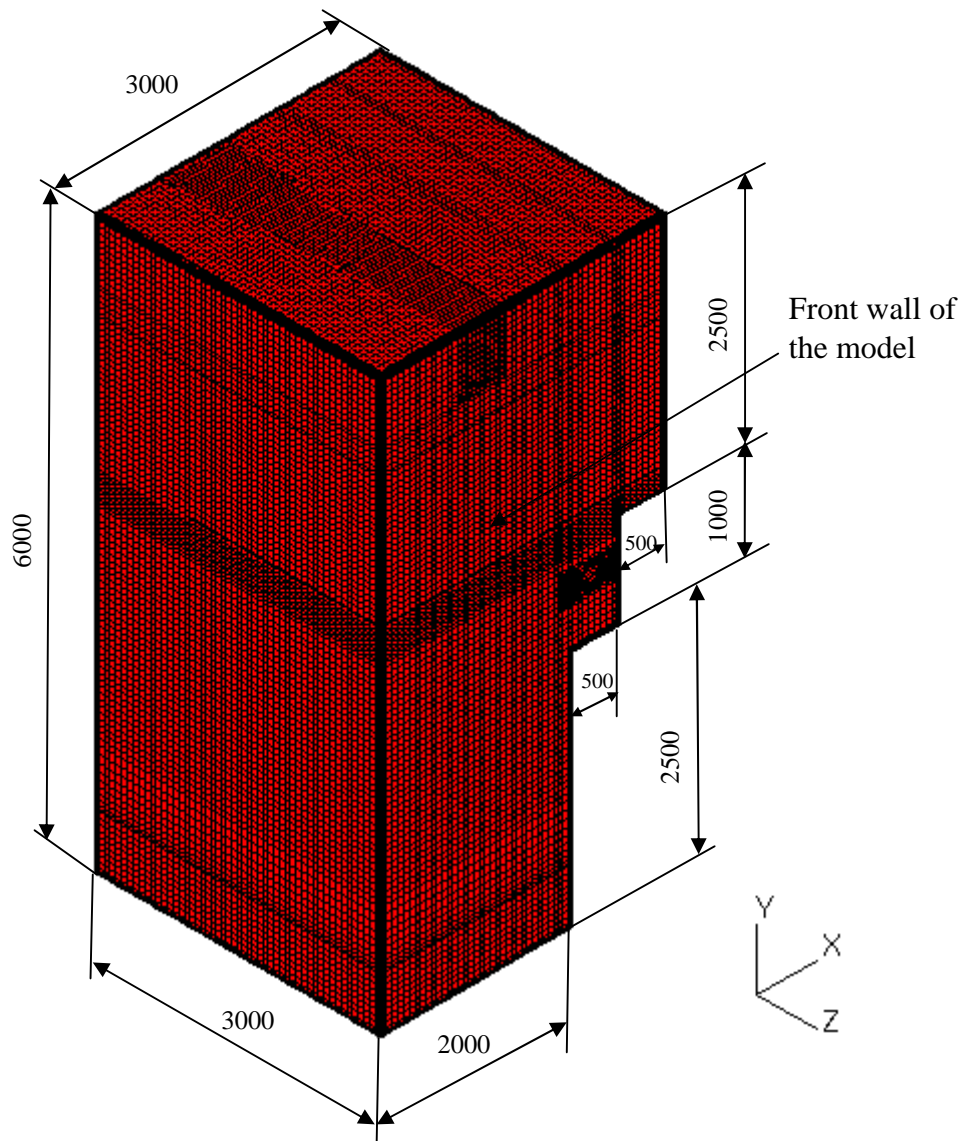


Fig. 3.14 Main external dimensions of the model (in mm).

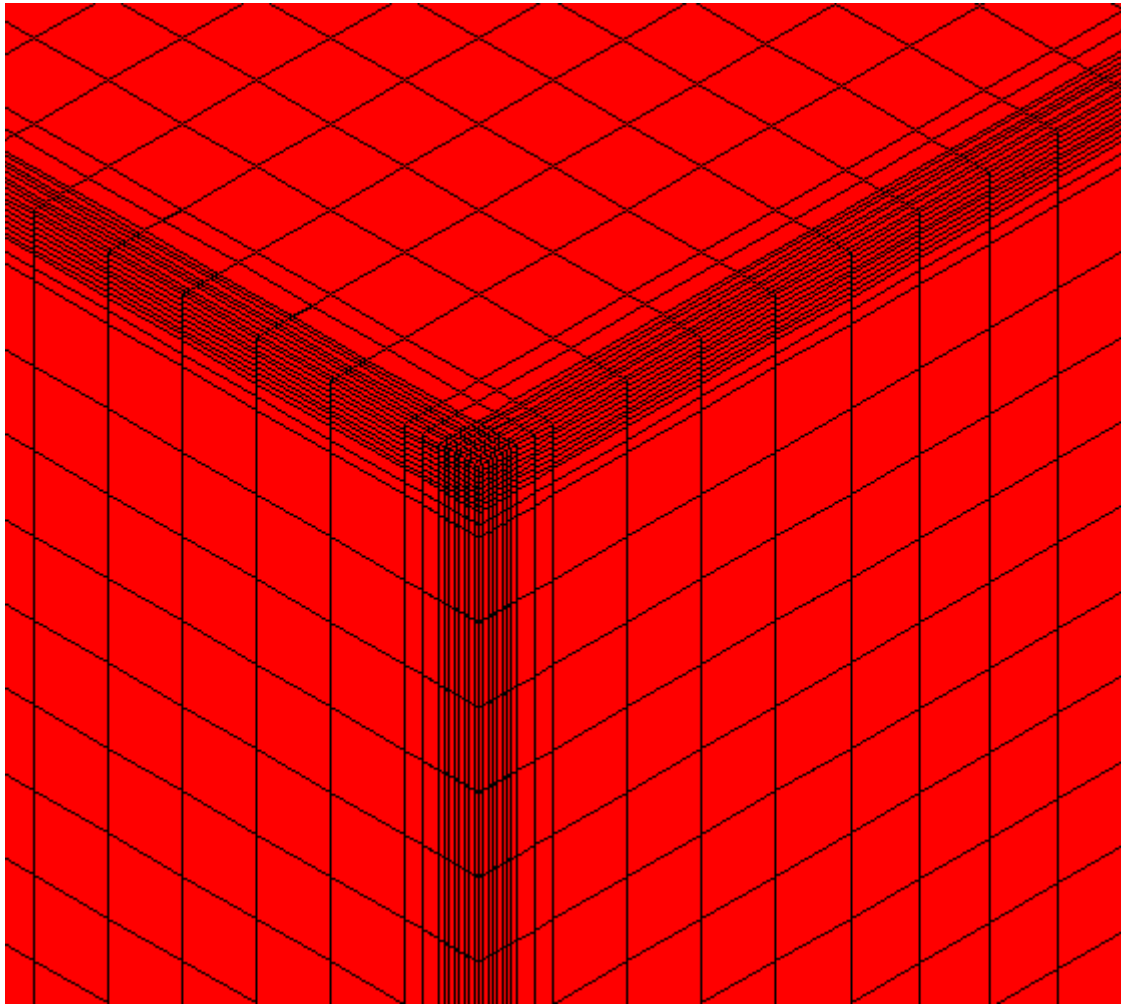


Fig.3.15 Non-uniform mesh in the near the wall region

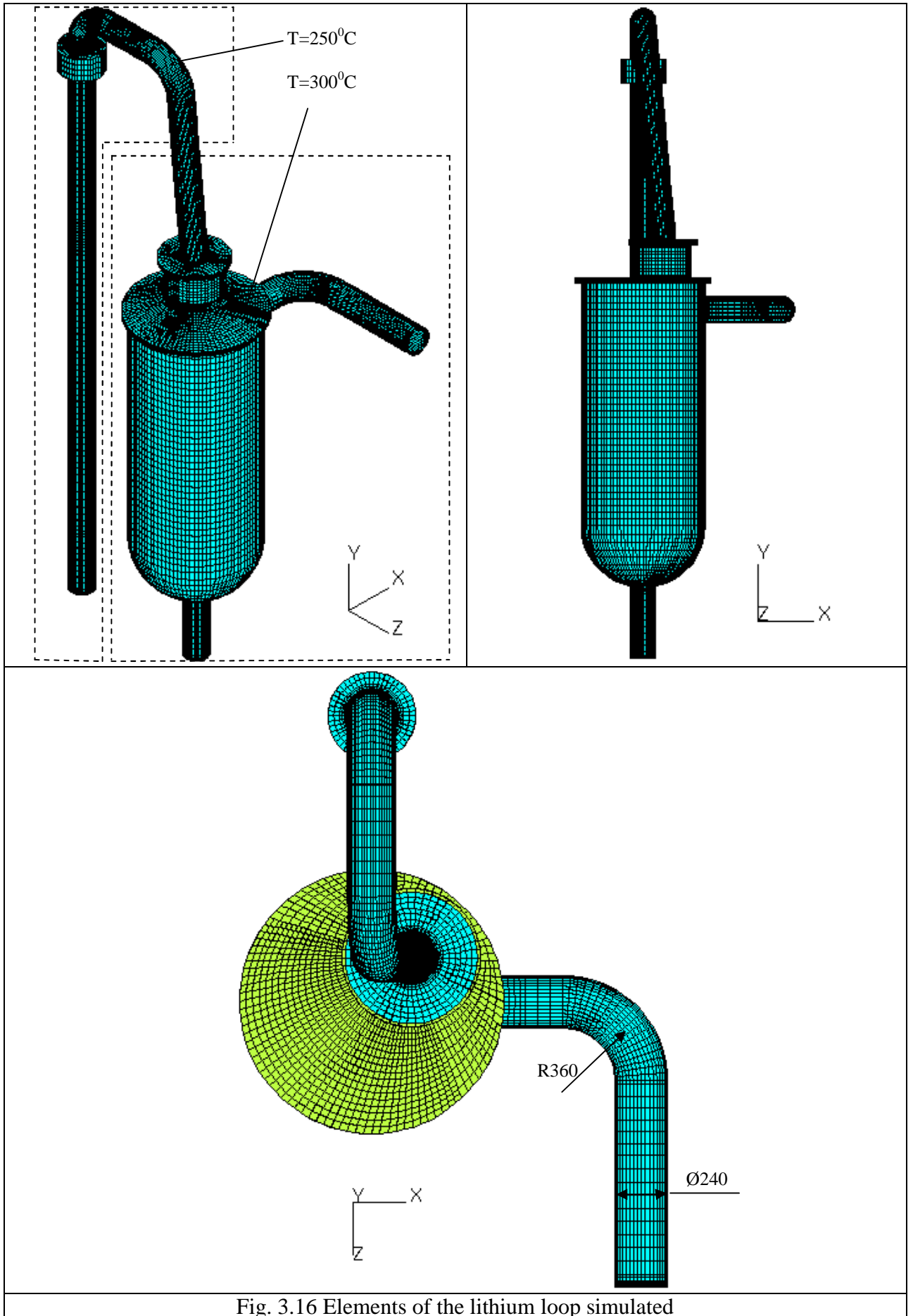


Fig. 3.16 Elements of the lithium loop simulated

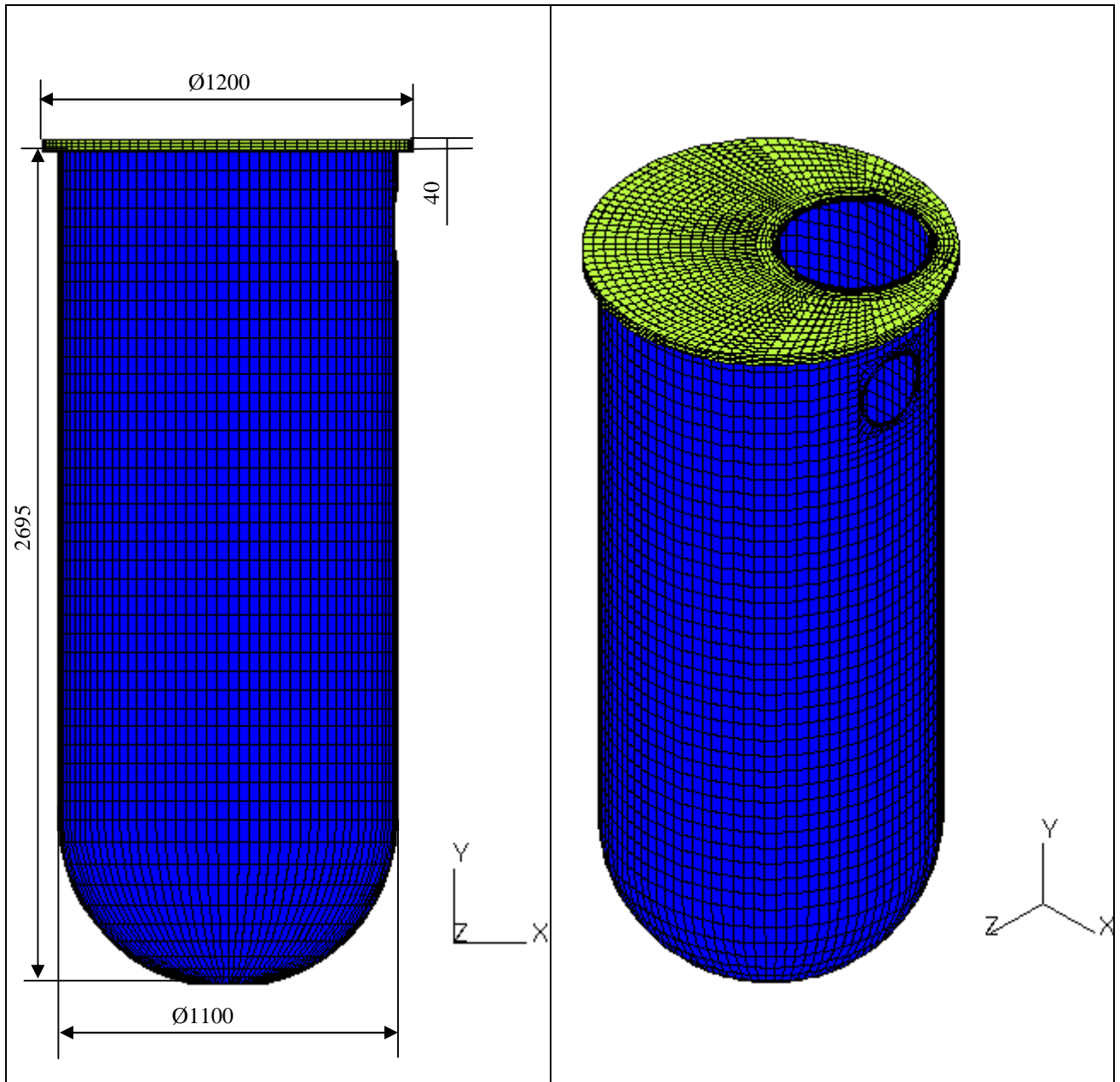


Fig. 3.17 Lithium tank with cover.

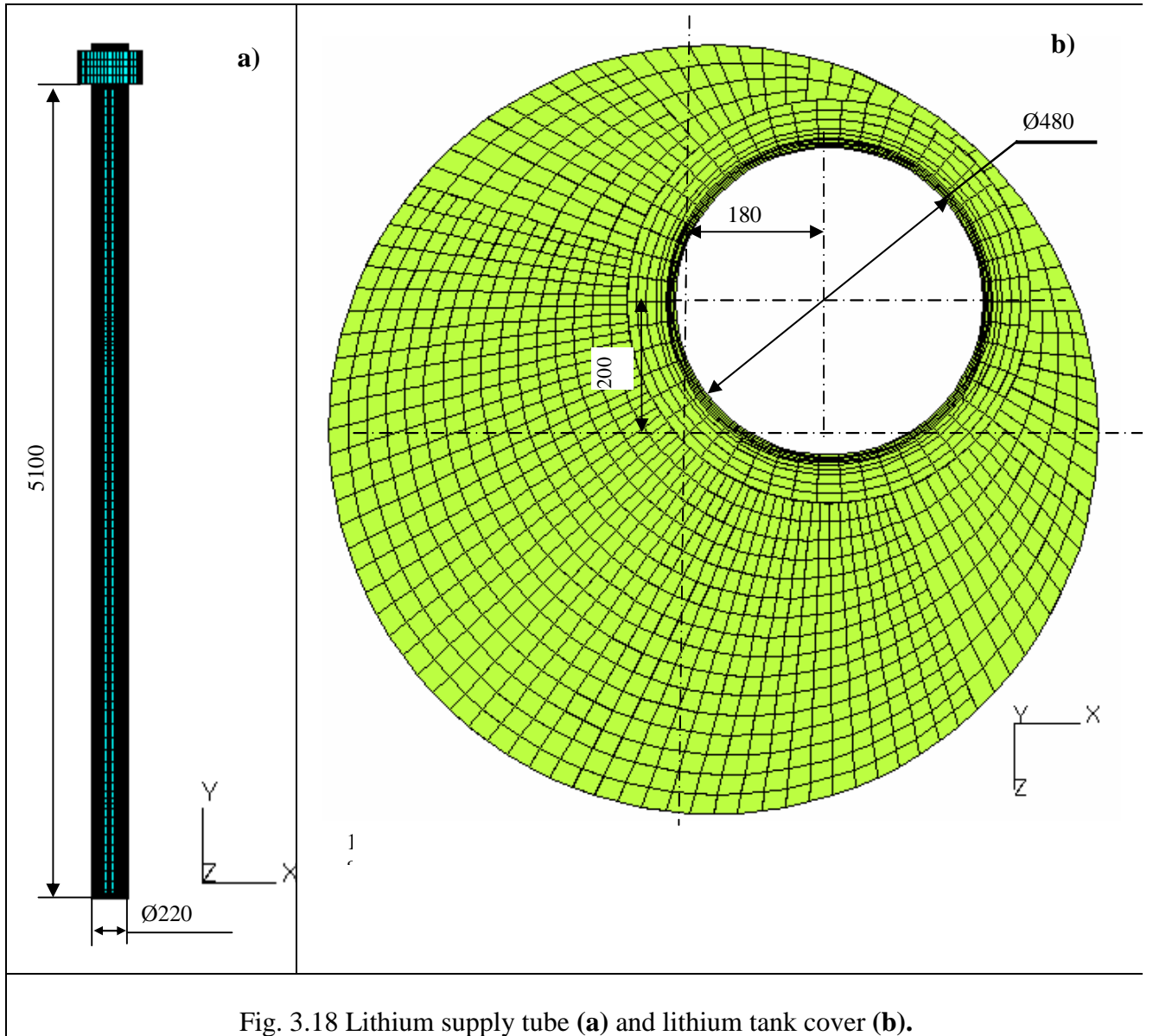


Fig. 3.18 Lithium supply tube (a) and lithium tank cover (b).

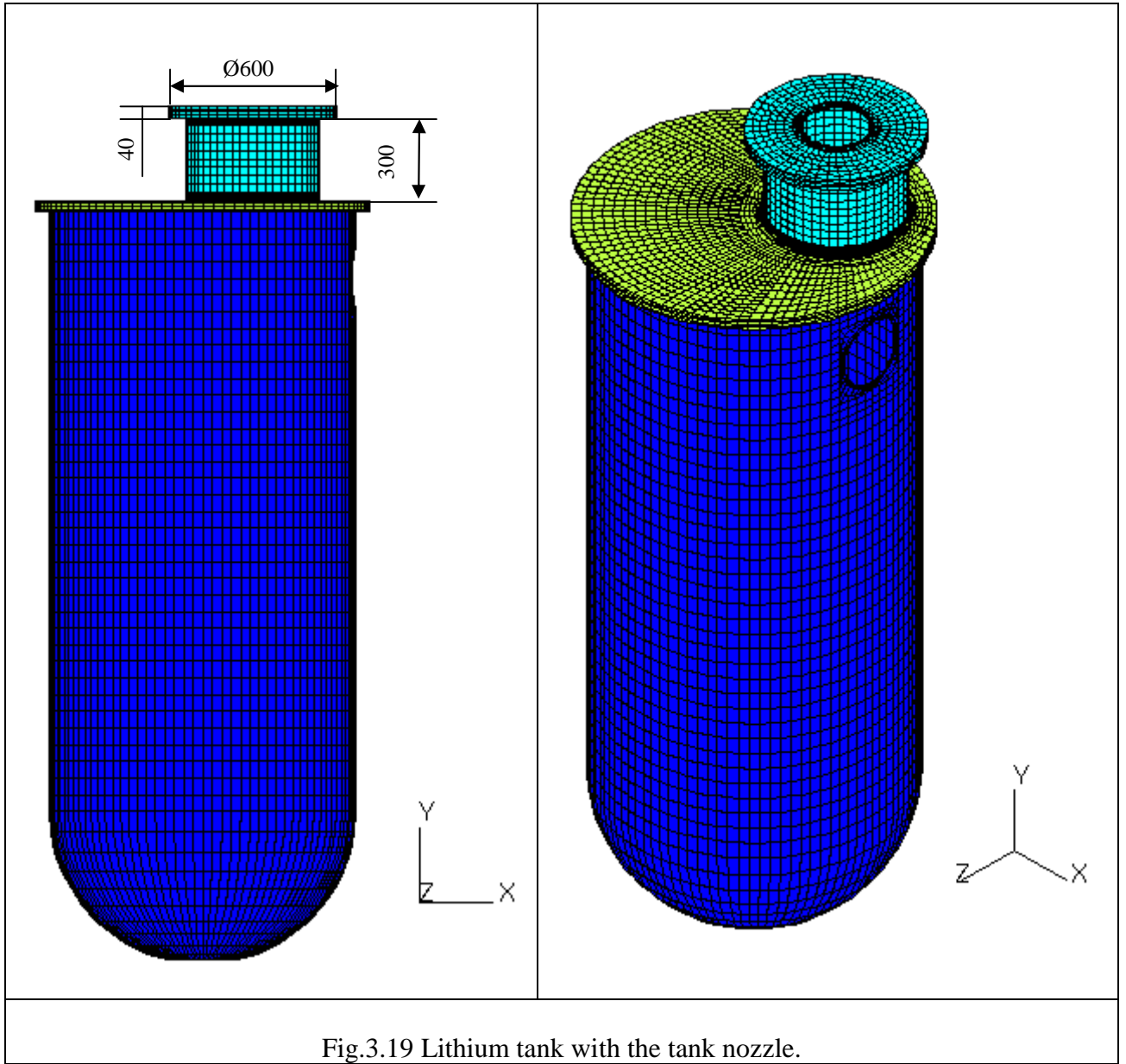
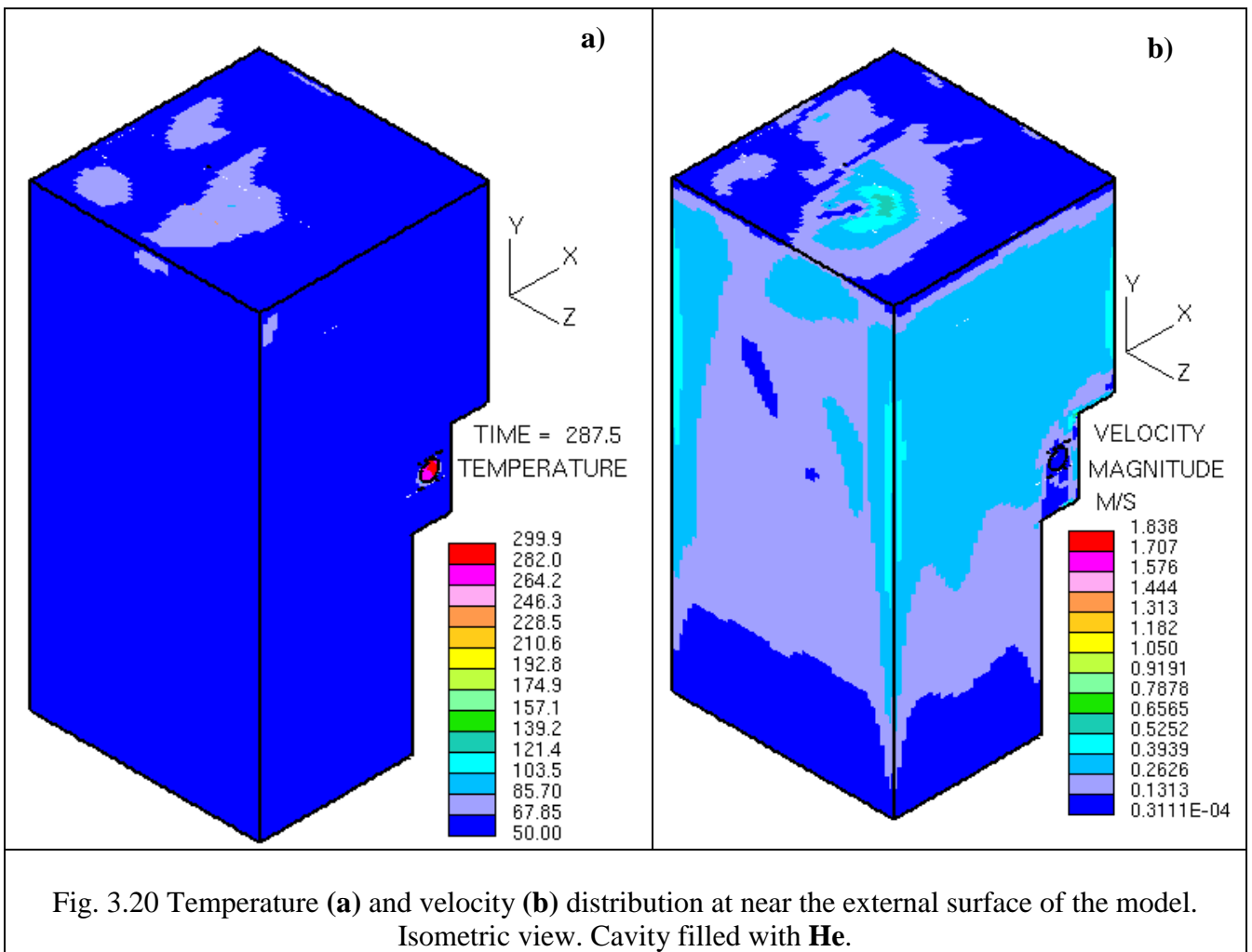


Fig.3.19 Lithium tank with the tank nozzle.



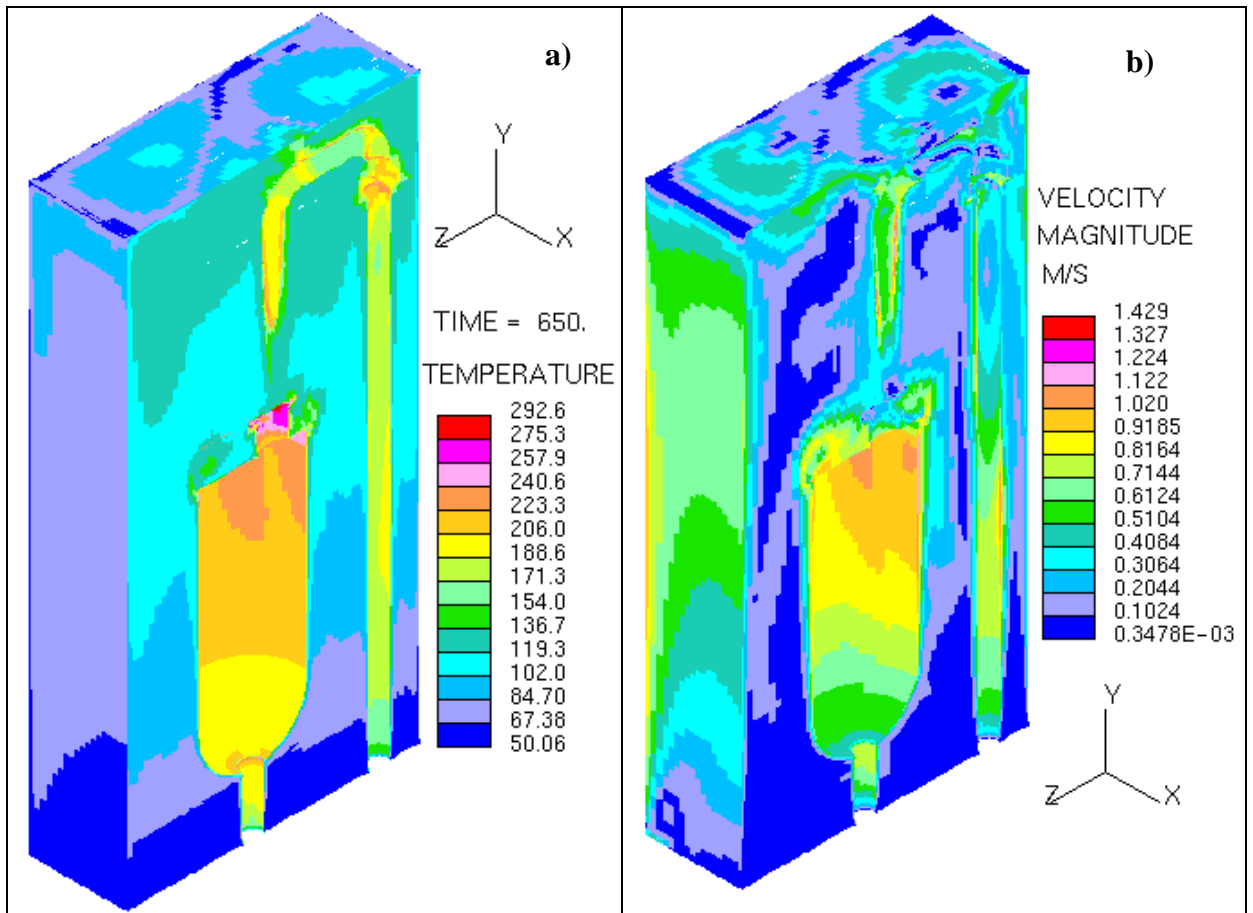


Fig.3.21 Temperature (a) and velocity (b) distribution inside the model. Isometric view. Cavity filled with Ar.

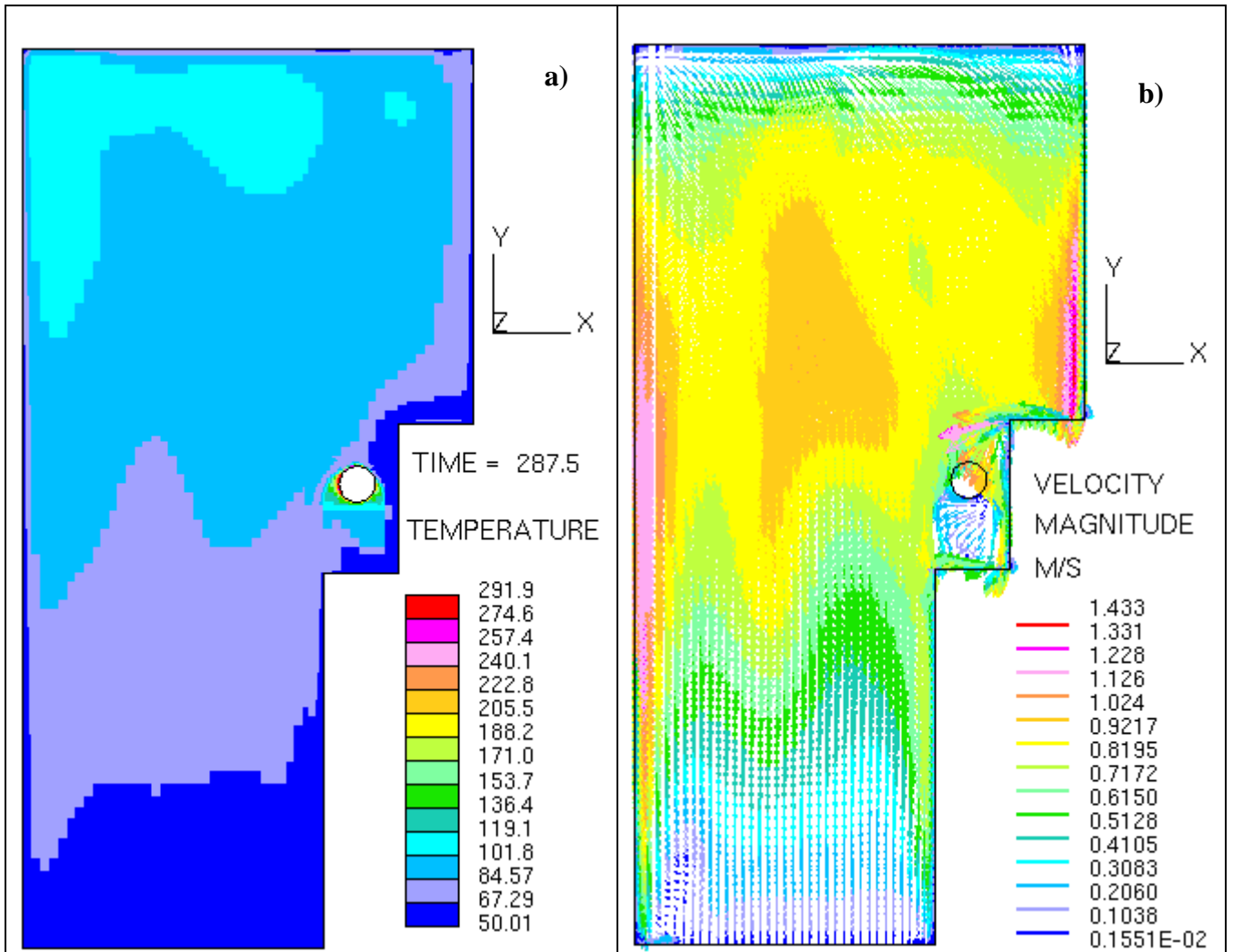


Fig.3.22 Temperature (a) and velocity (b) distribution in the model cross section located at 20 mm from the front wall of the model. X-Y coordinate plane. Cavity filled with He.

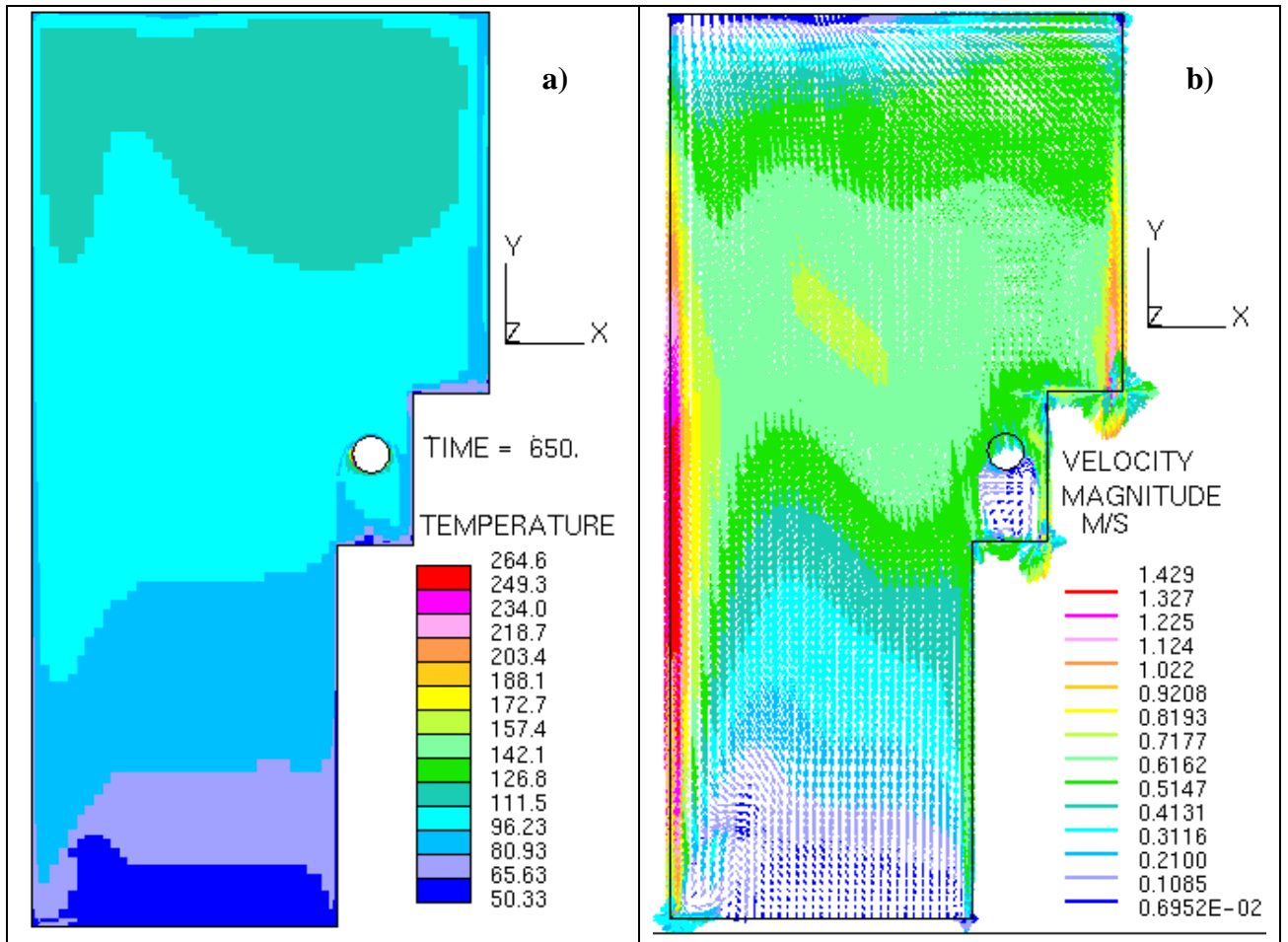


Fig. 3.23 Temperature (a) and velocity (b) distribution in the model cross section located at 20 mm from the front wall of the model. X-Y coordinate plane. Cavity filled with Ar.

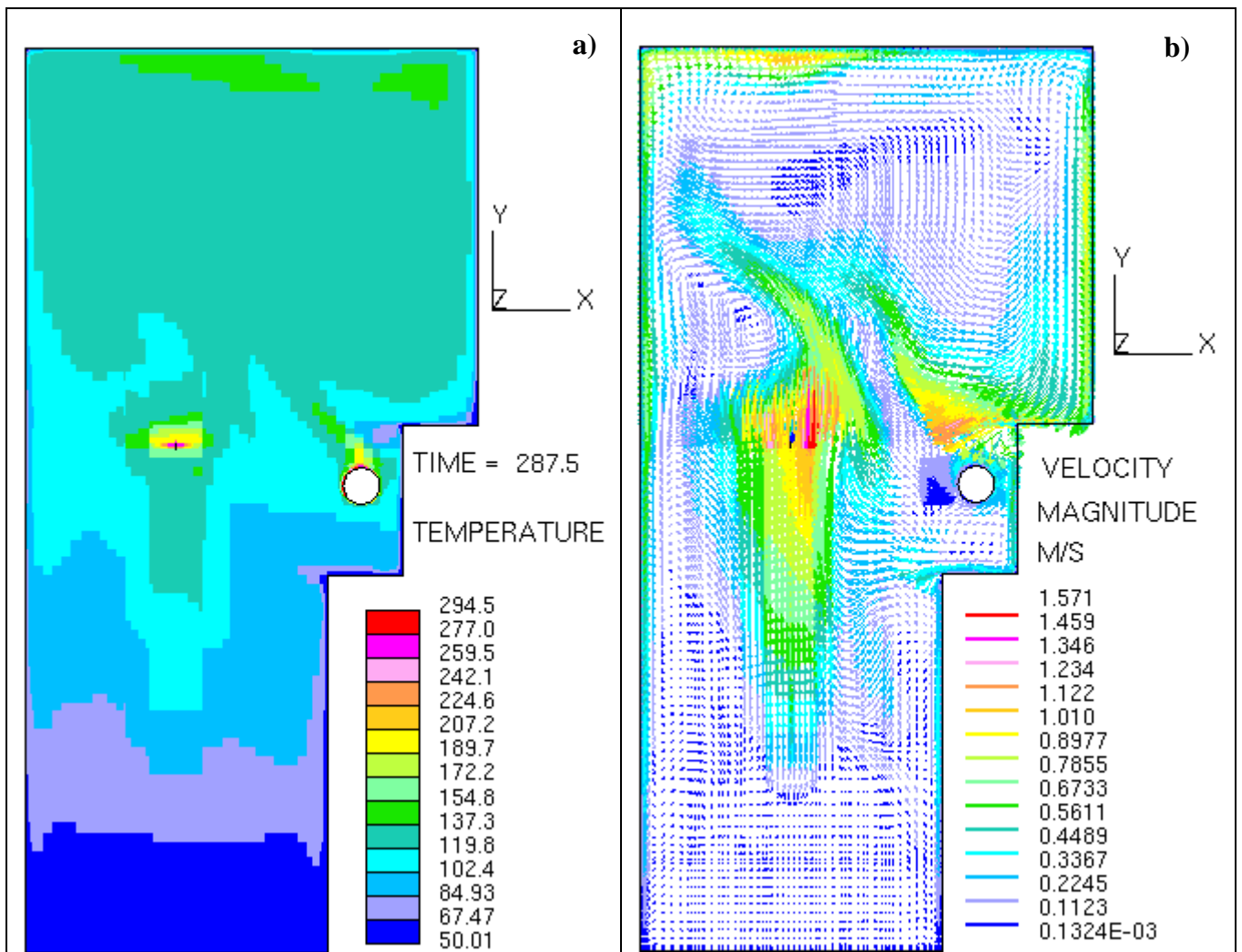


Fig. 3.24 Temperature **(a)** and velocity **(b)** distribution in the model cross section located at 700 mm from the front wall (cross section near the lithium tank wall). X-Y coordinate plane. Cavity filled with **He**.

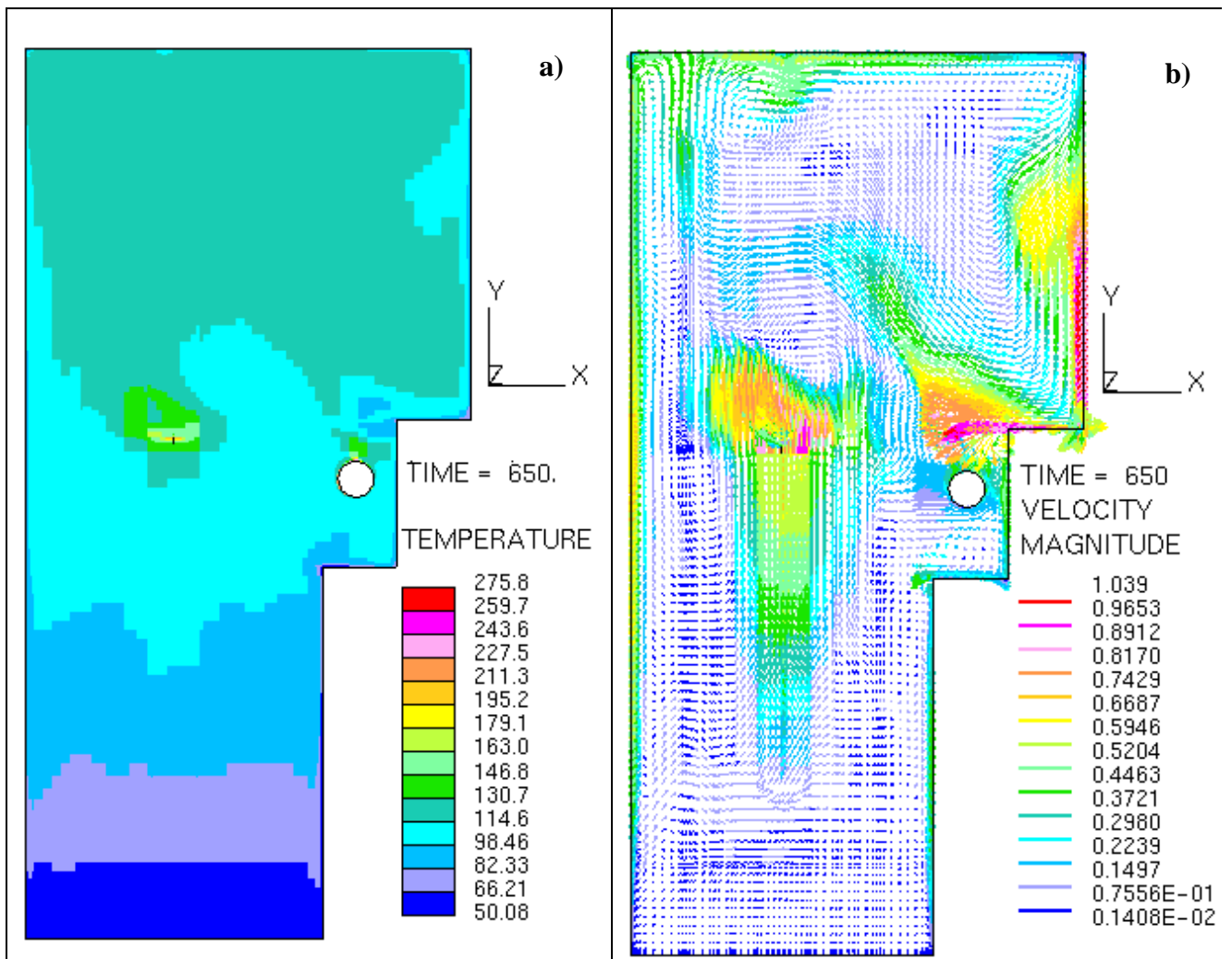


Fig.3.25 Temperature **(a)** and velocity **(b)** distribution in the model cross section located at 700 mm from the front wall (cross section near the lithium tank wall). X-Y coordinate plane. Cavity filled with **Ar**.

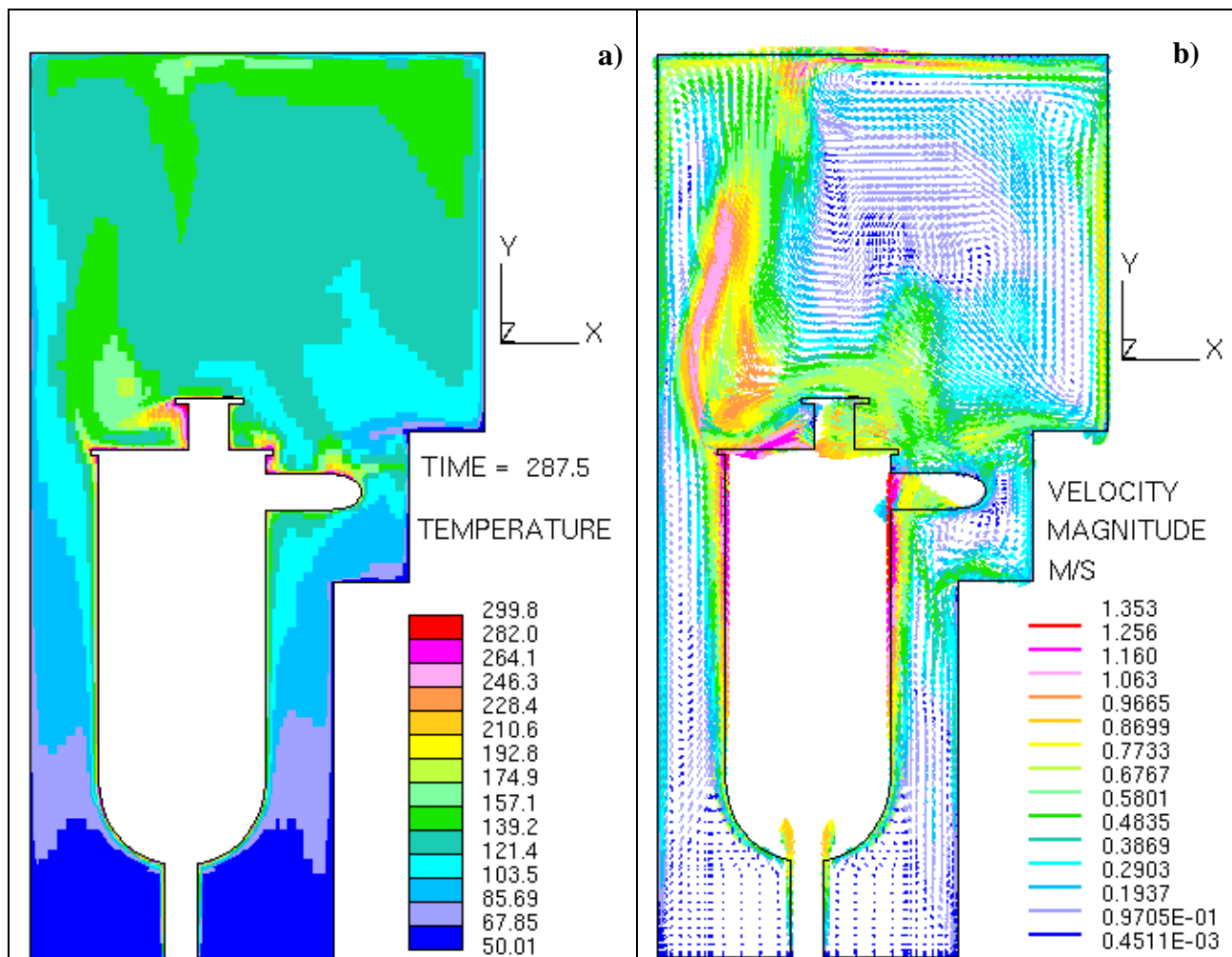


Fig.3.26 Temperature **(a)** and velocity **(b)** distribution in the plane passing through the lithium tank mid cross section. X-Y coordinate plane. Cavity filled with **He**.

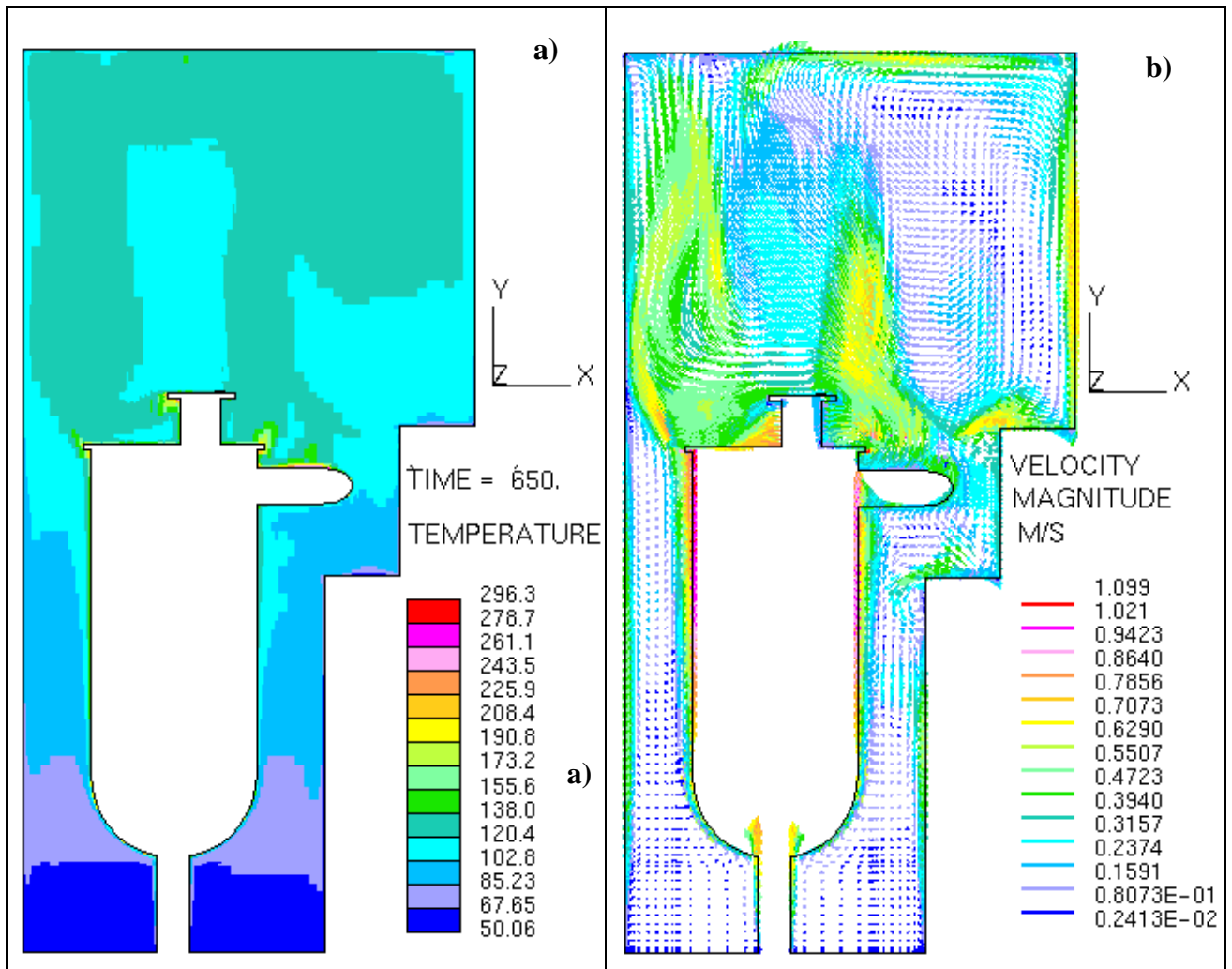


Fig. 3.27 Temperature (a) and velocity (b) distribution in the plane passing through the lithium tank mid cross section. X-Y coordinate plane. Cavity filled with Ar.

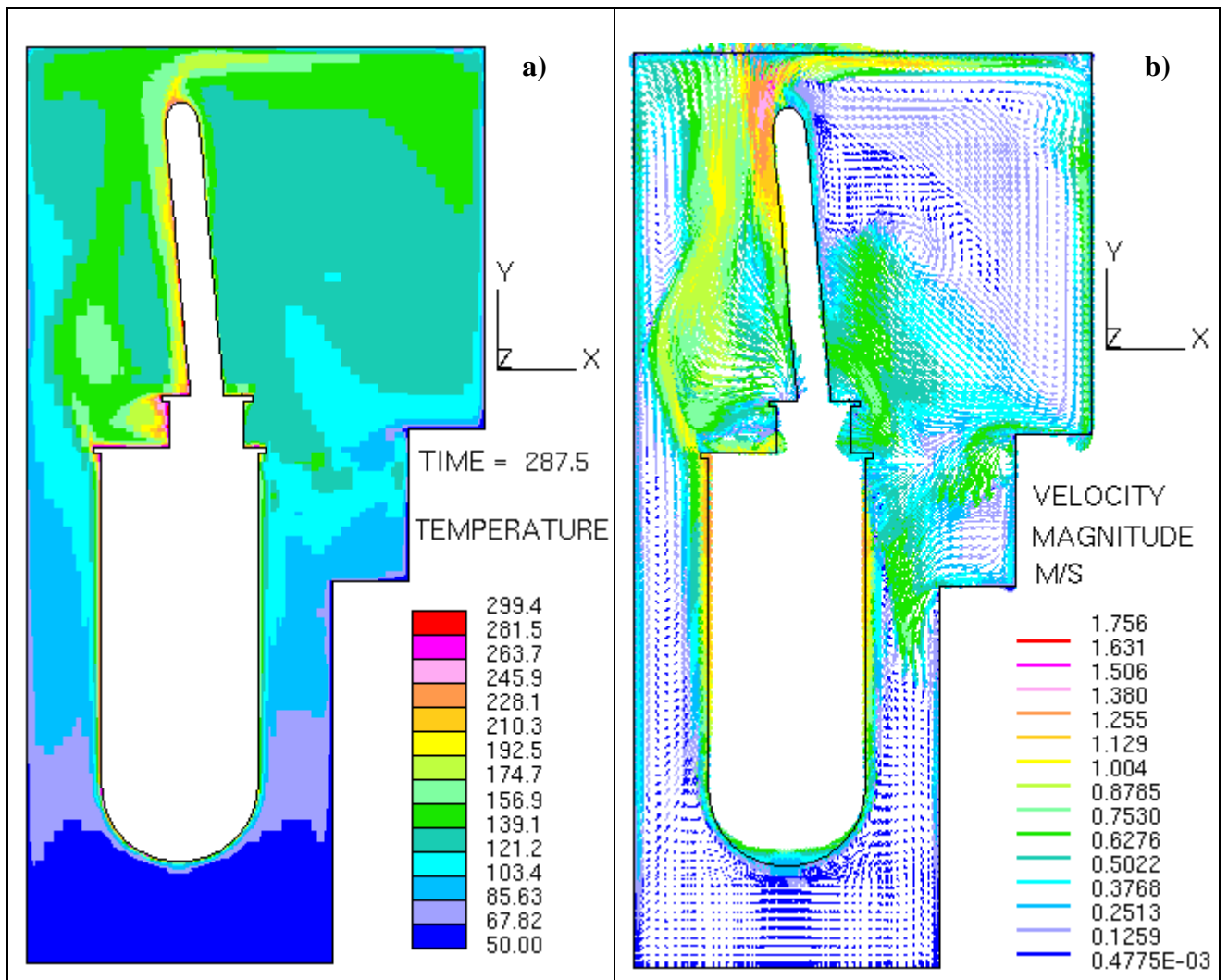


Fig.3.28 Temperature (a) and velocity (b) distribution in the plane passing through the tank nozzle mid cross section. X-Y coordinate plane. Cavity filled with He.

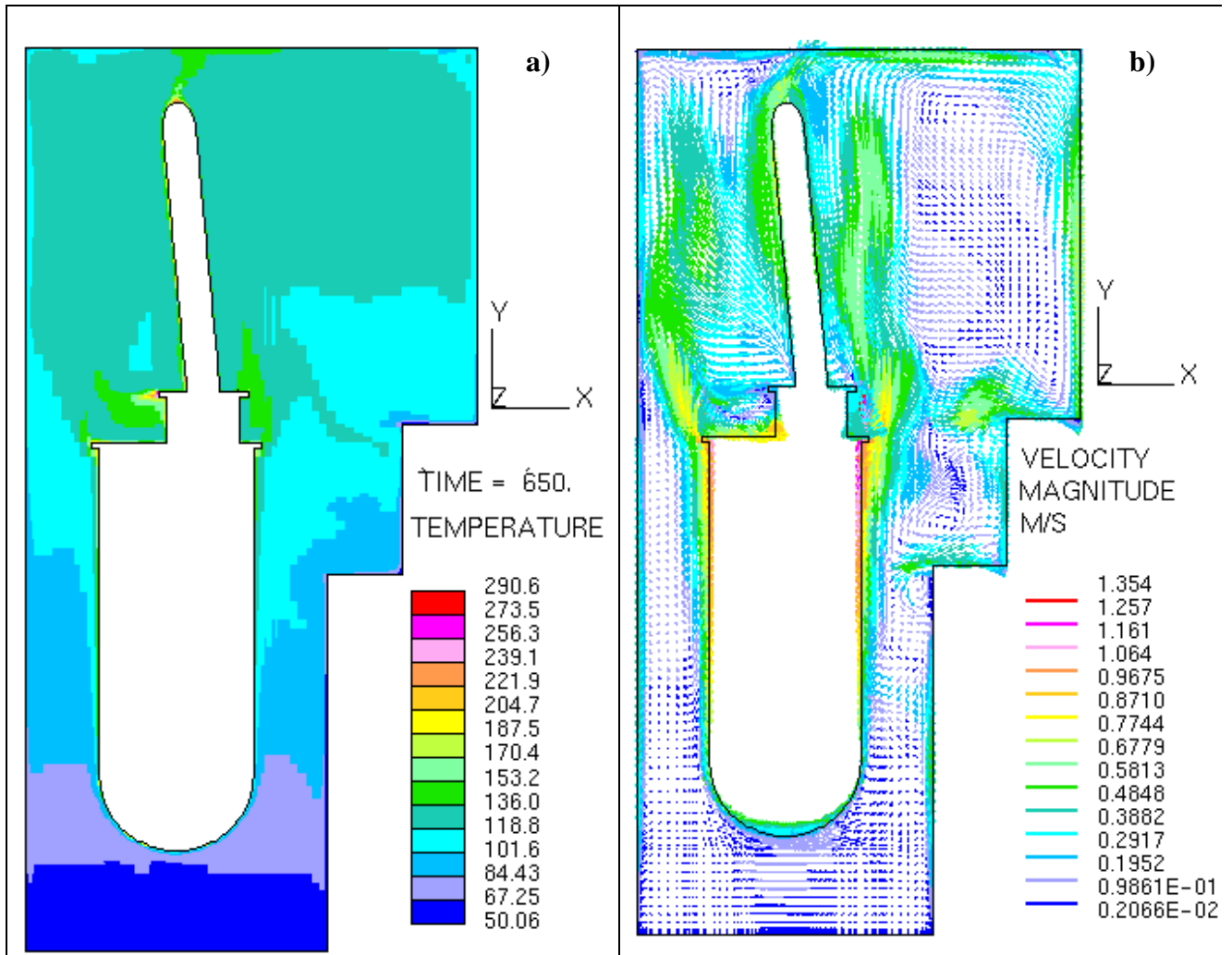


Fig.3.29 Temperature (a) and velocity (b) distribution in the plane passing through the tank nozzle mid cross section. X-Y coordinate plane. Cavity filled with Ar.

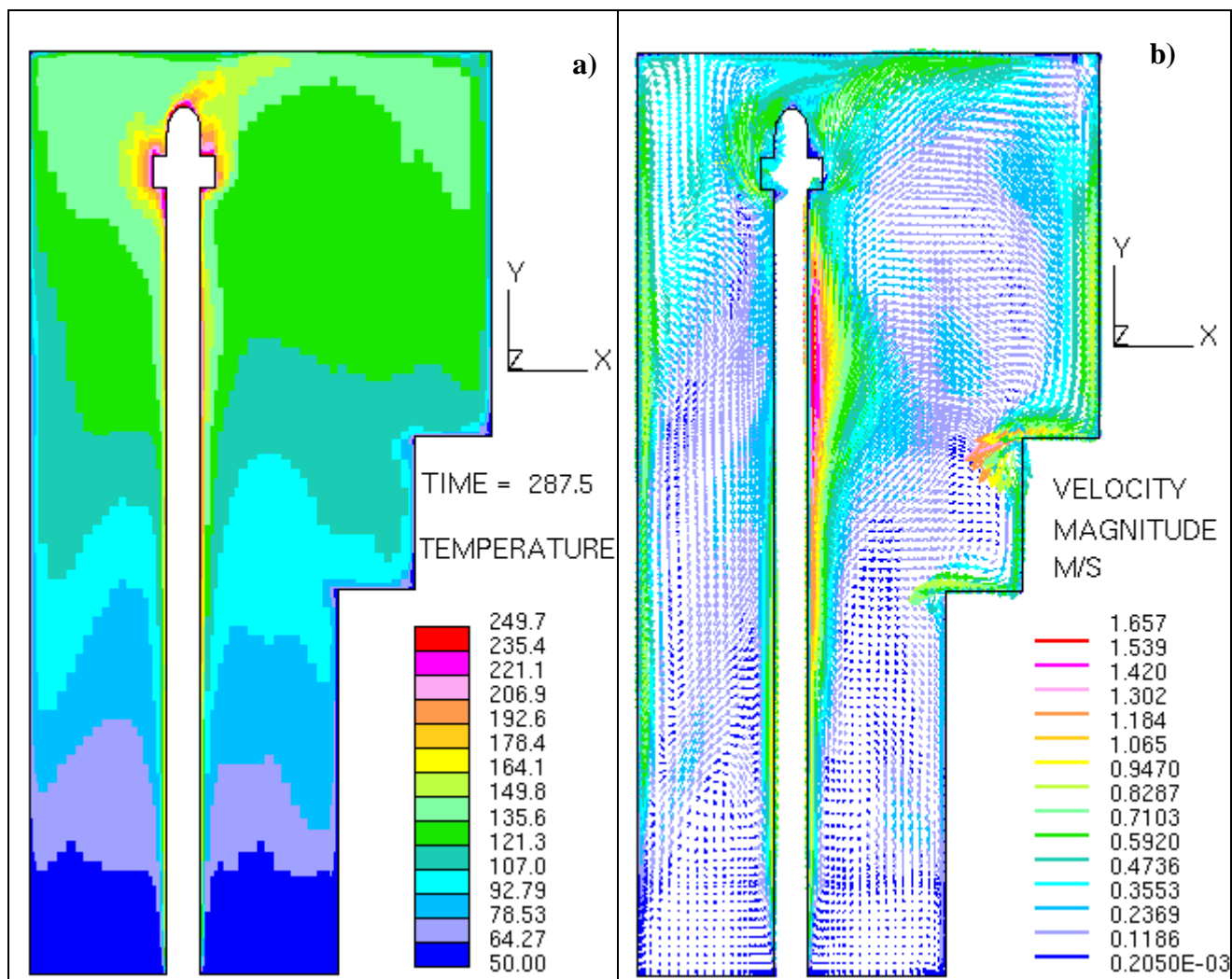


Fig.3.30 Temperature (a) and velocity (b) distribution in the plane passing through the lithium supply pipe mid cross section. X-Y coordinate plane. Cavity filled with He.

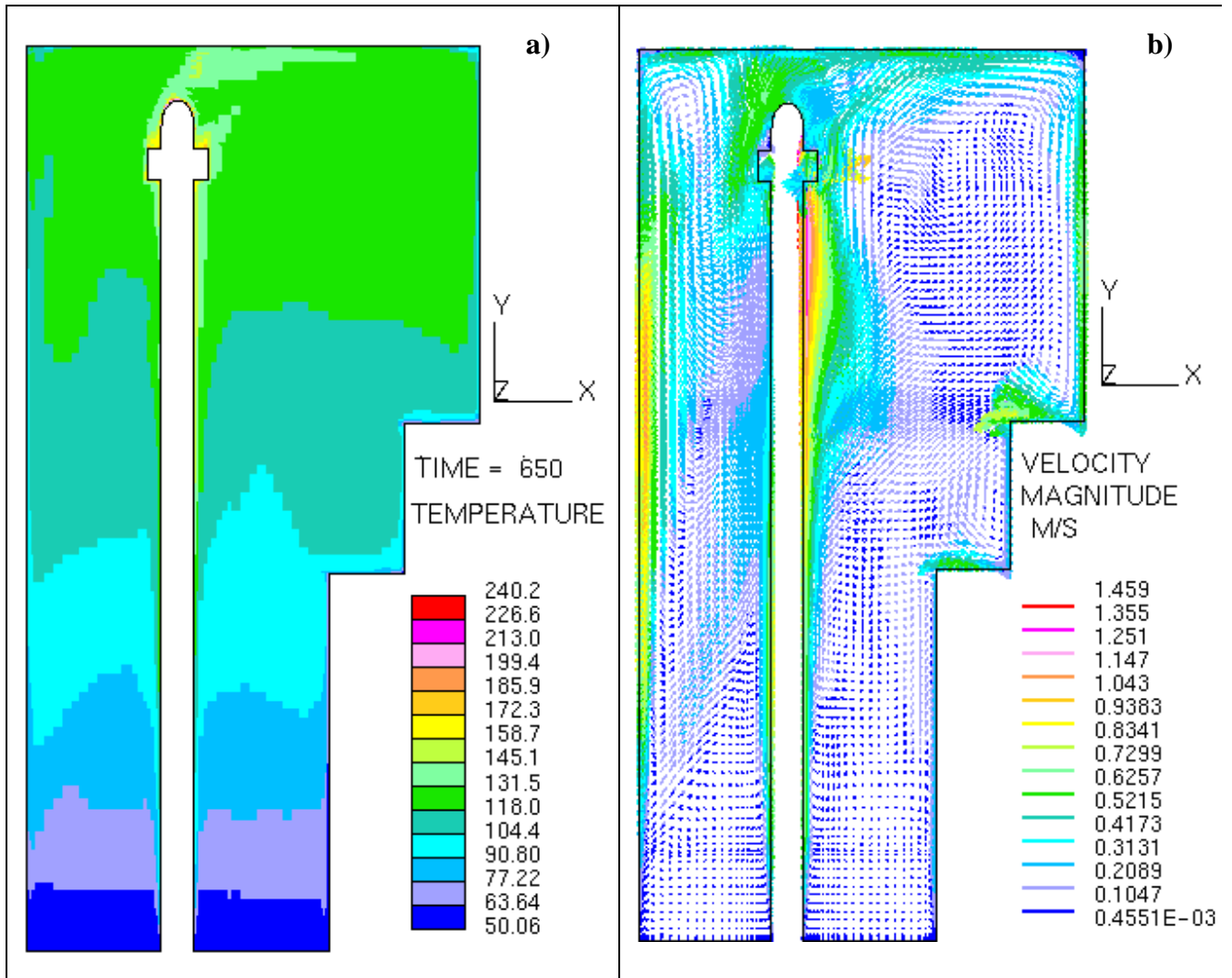


Fig.3.31 Temperature (a) and velocity (b) distribution in the plane passing through the lithium supply pipe mid cross section. X-Y coordinate plane. Cavity filled with Ar.

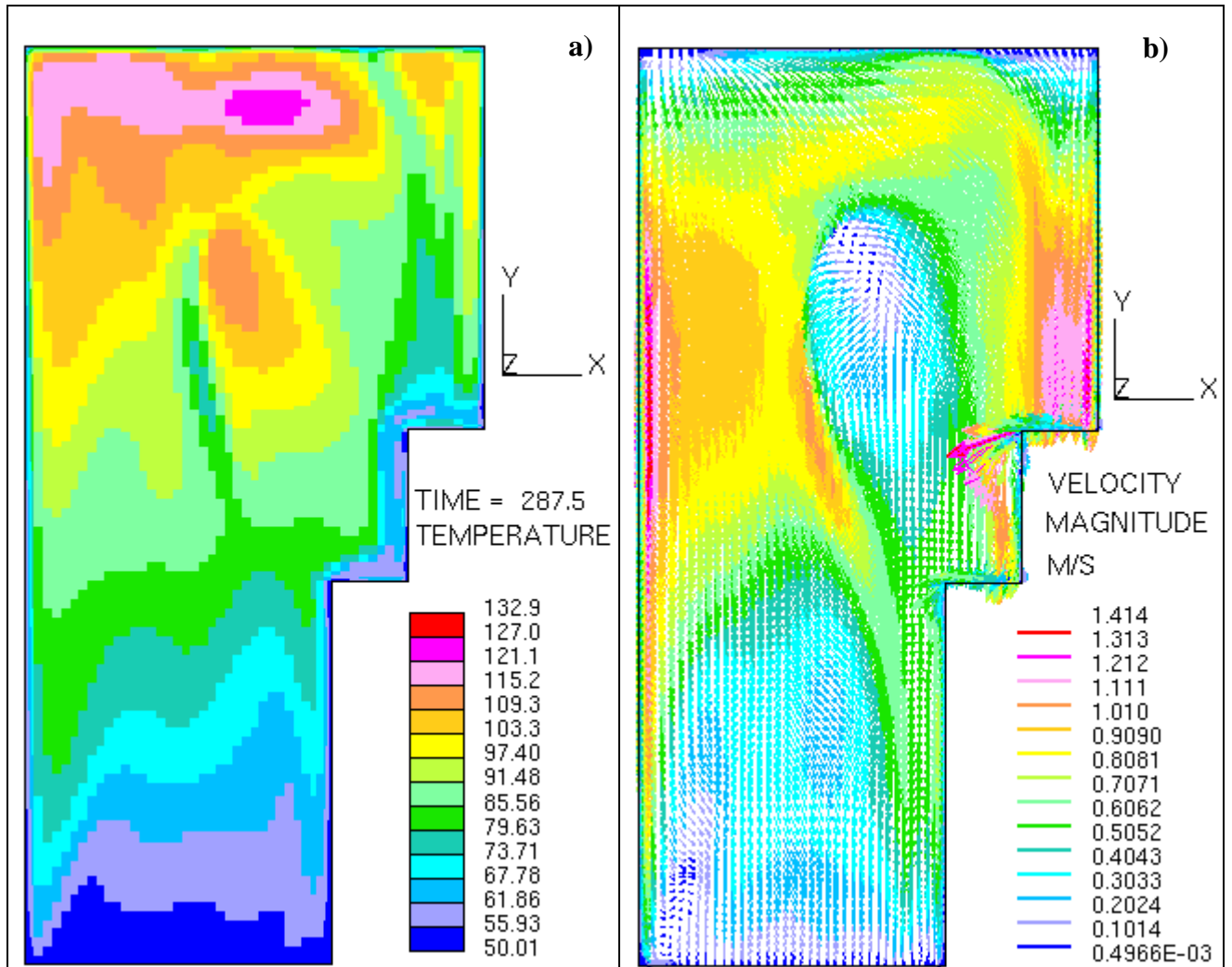


Fig. 3.32 Temperature **(a)** and velocity **(b)** distribution in the model cross section located at 20 mm from the back wall of the model. X-Y coordinate plane. Cavity filled with **He**

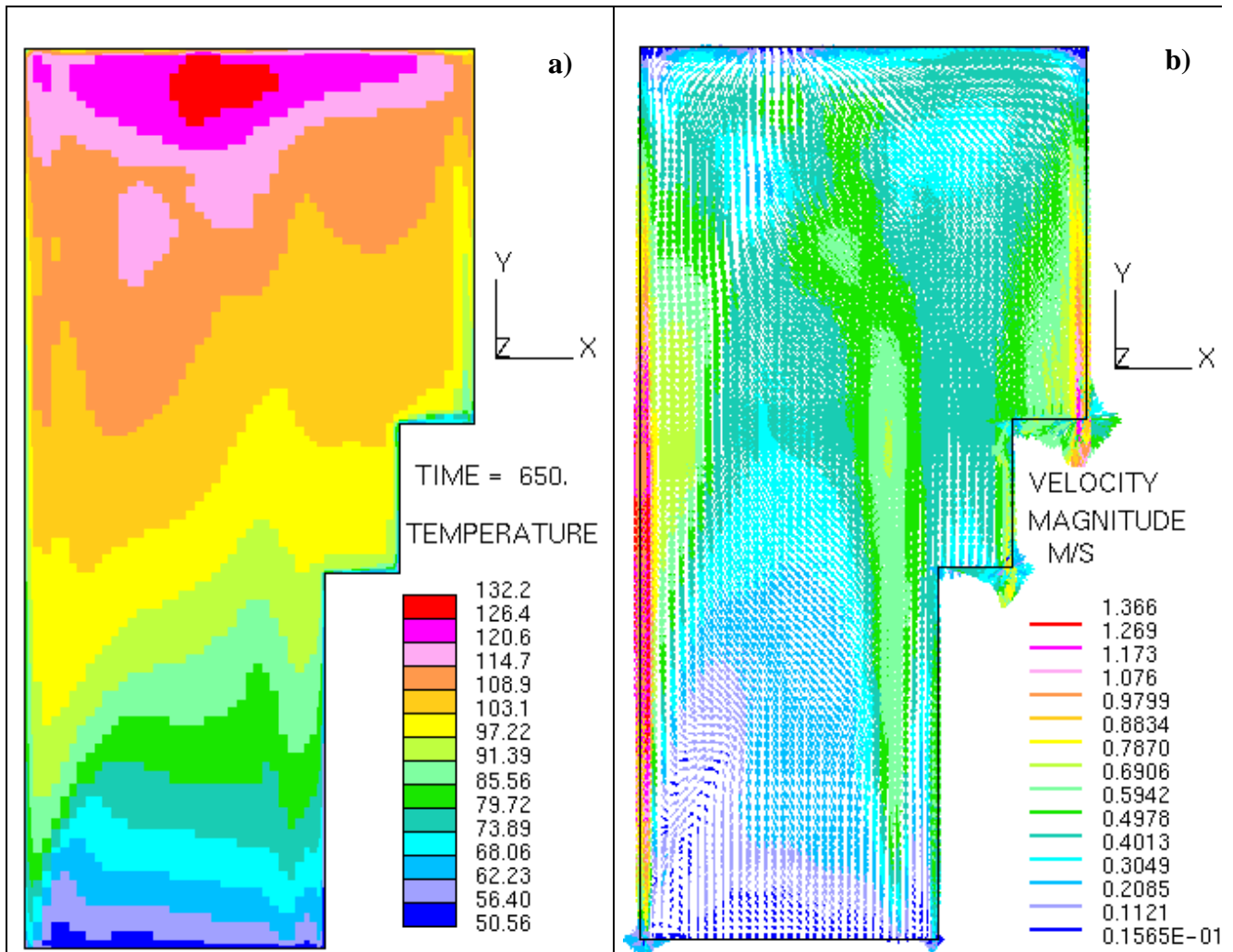
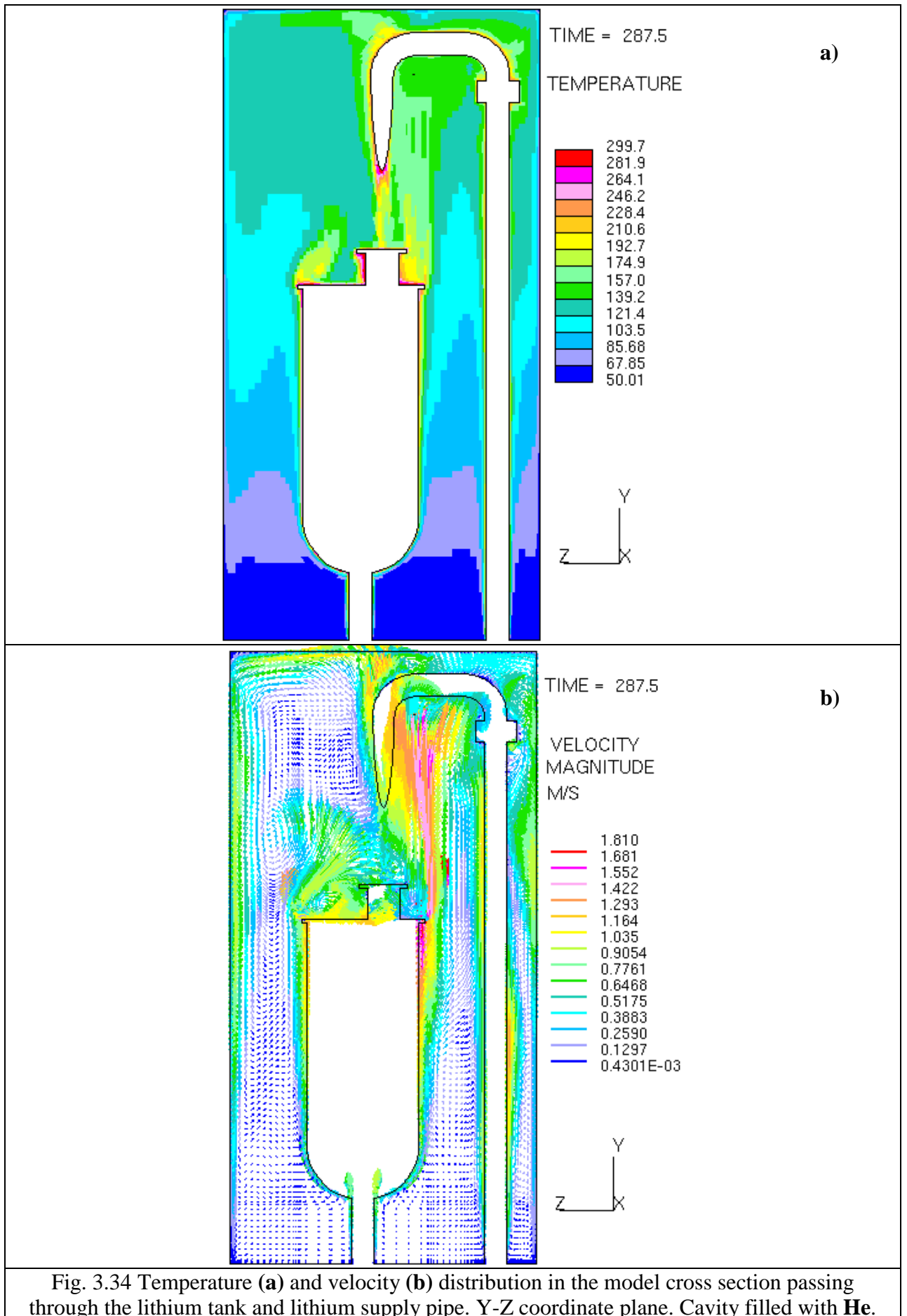
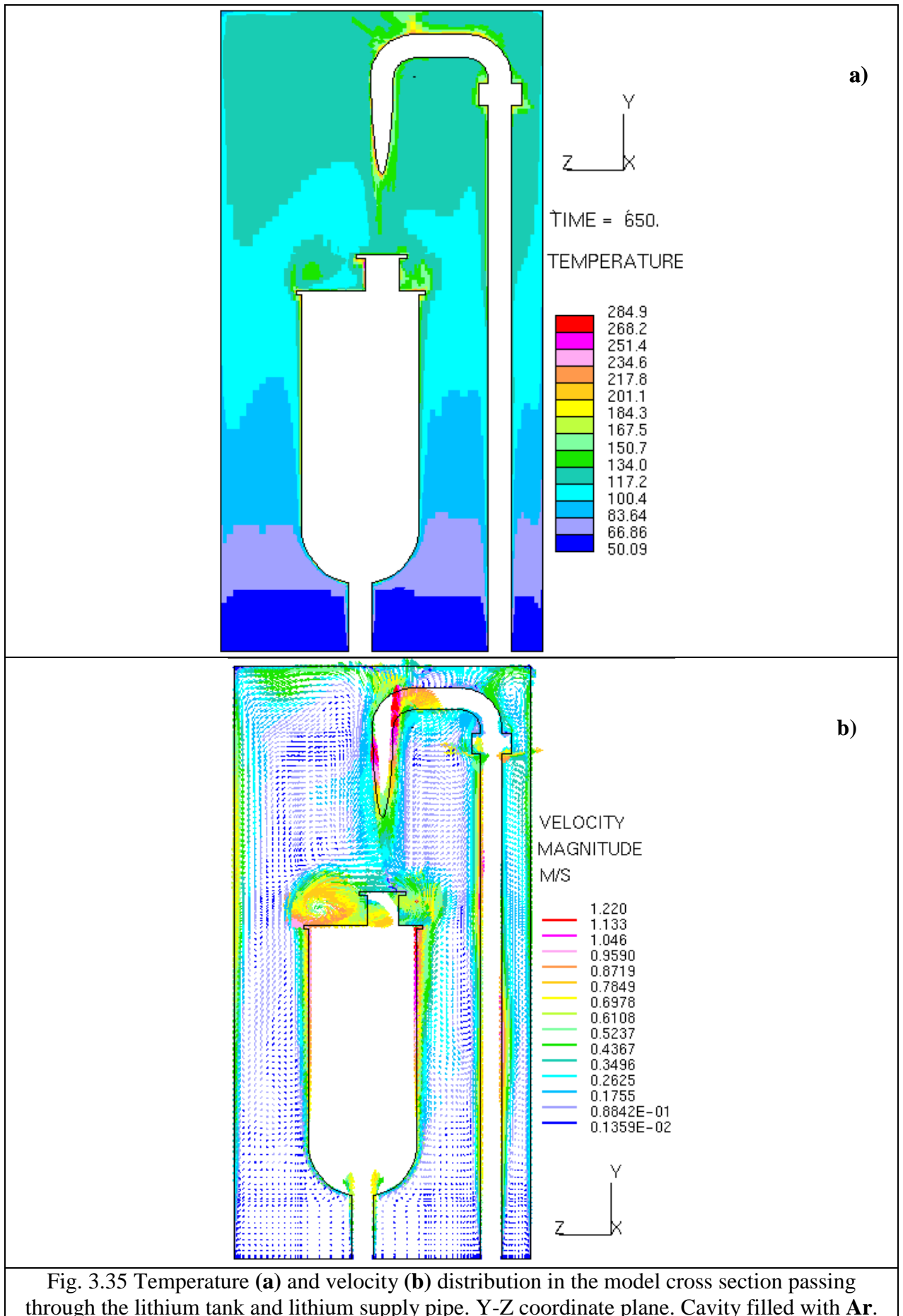


Fig. 3.33 Temperature **(a)** and velocity **(b)** distribution in the model cross section located at 20 mm from the back wall of the model. X-Y coordinate plane. Cavity filled with Ar





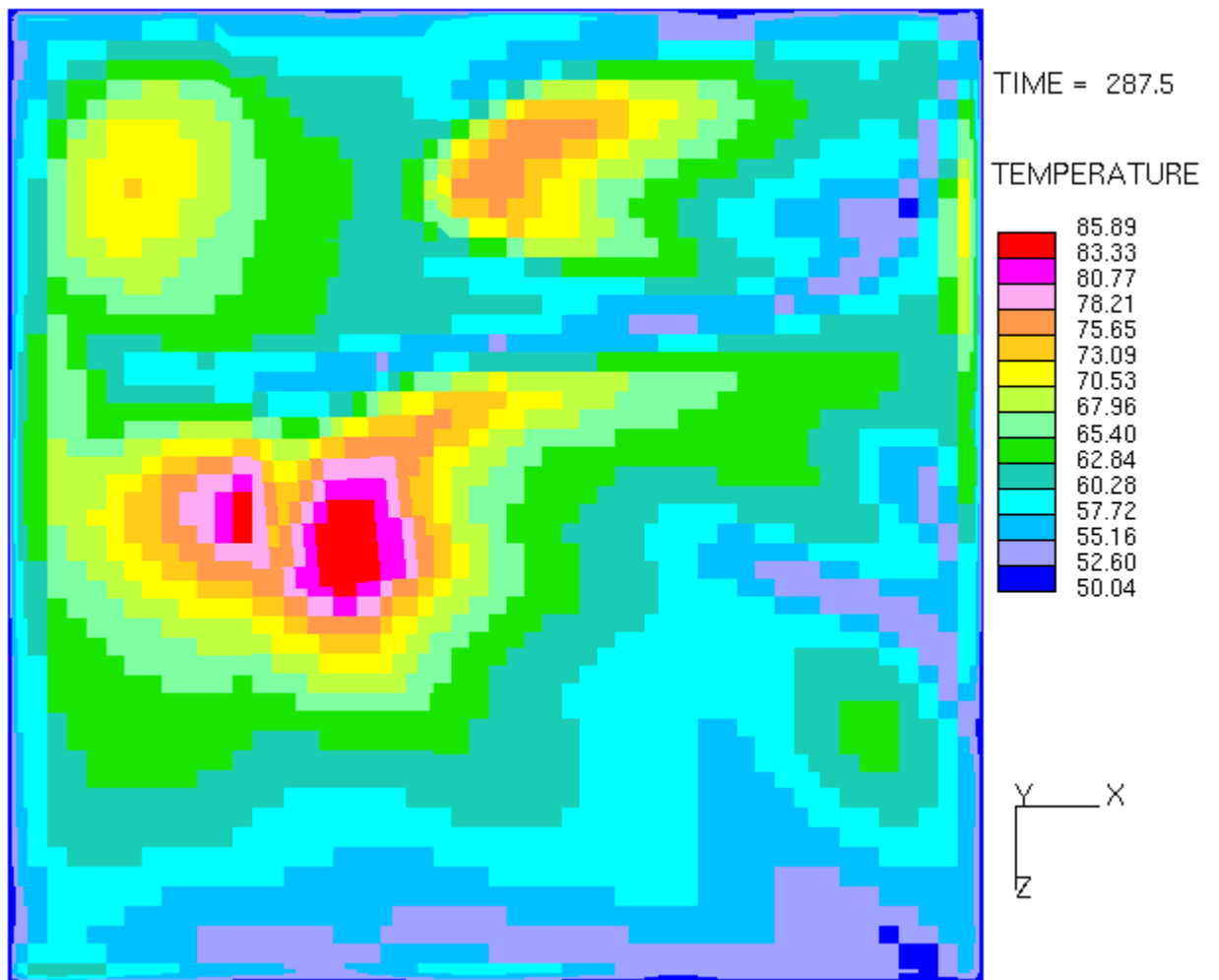


Fig. 3.36 Temperature distribution in the model cross section located at 2 mm from the top wall of the model. X-Z coordinate plane. Cavity filled with **He**.

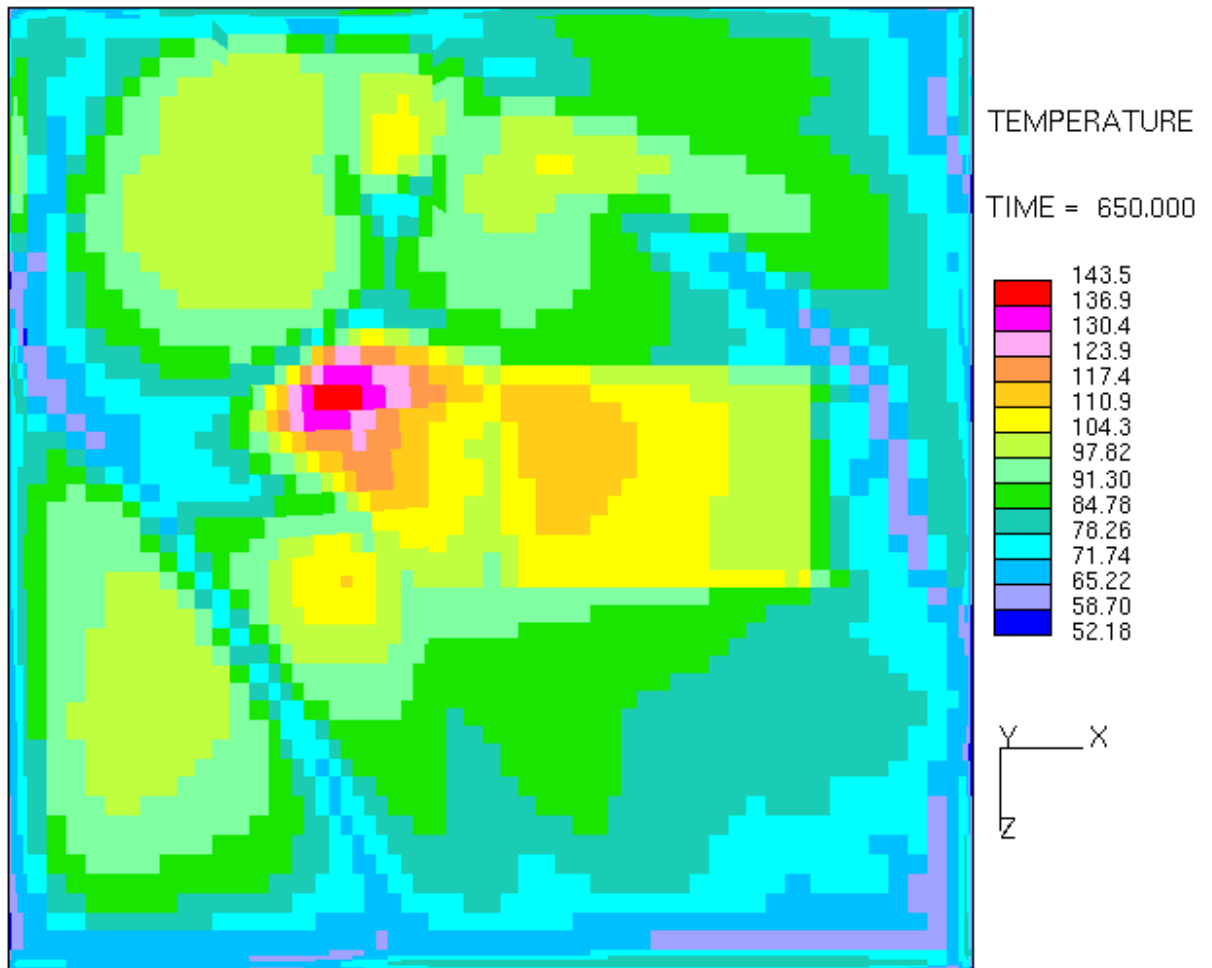


Fig. 3.37 Temperature distribution in the model cross section located at 2 mm from the top wall of the model. X-Z coordinate plane. Cavity filled with Ar.

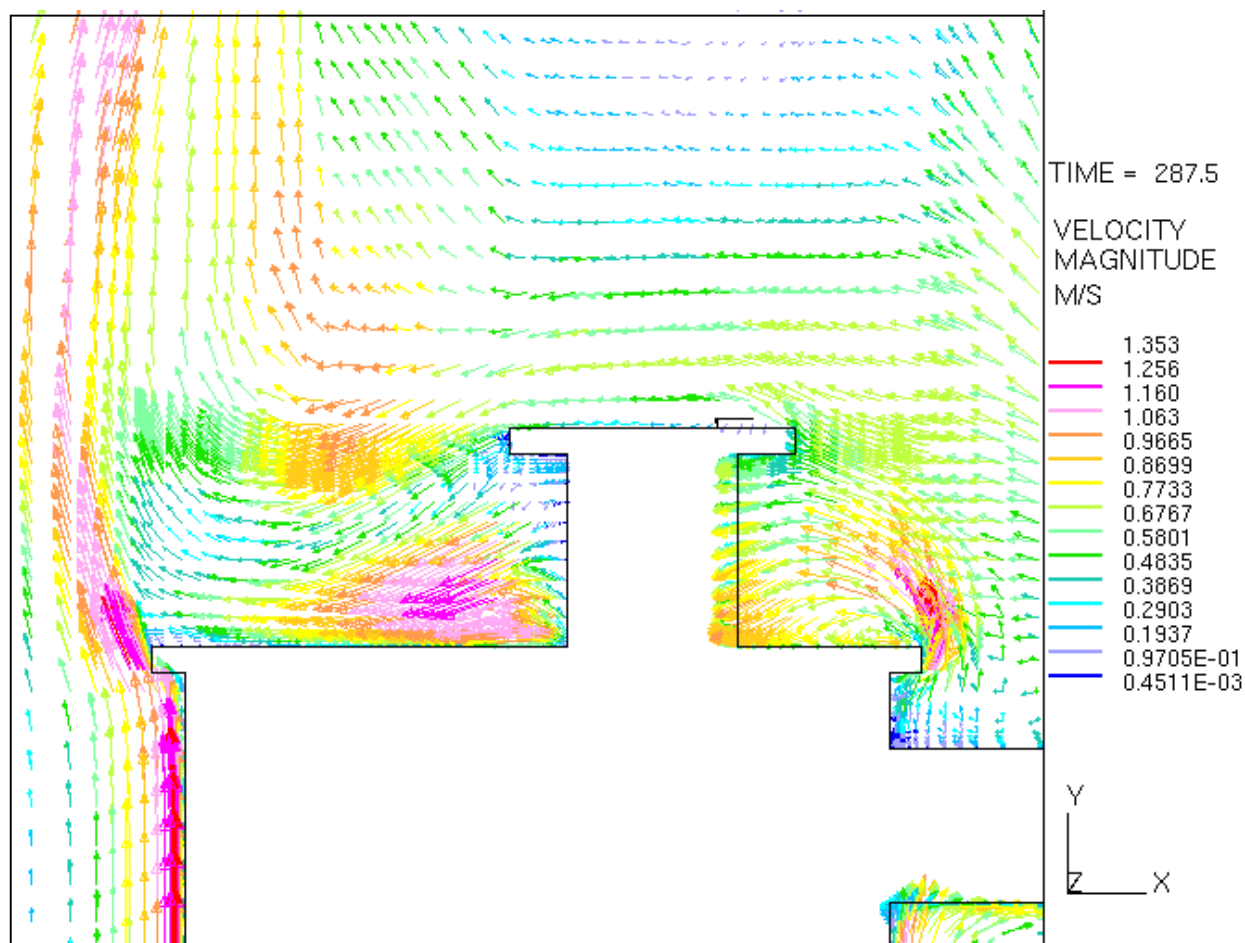


Fig. 3.38 Detailed view of the velocity field near the nozzle of the lithium tank. Plane passes through the lithium tank mid cross section (see Fig. 3.26). Cavity with  $\text{He}$ .